

# **Multi-Physics Stochastic Modeling of a High Speed Composite Flywheel Energy Storage System**

A Thesis

Presented in Partial Fulfillment of the Requirements for the

Degree of Master of Science

with a

Major in Mechanical Engineering

in the

College of Graduate Studies

University of Idaho

by

Justin D. Pettingill

Major Professor: Matthew Riley, Ph.D.

Committee Members: Michael Santora, Ph.D. and Gabriel P. Potirniche, Ph.D.

Department Administrator: Steven Beyerlein, Ph.D.

May 2017

## Authorization to Submit

This thesis of Justin D. Pettingill, submitted for the degree of Master of Science with a Major in Mechanical Engineering and titled “Multi-Physic Stochastic Modeling of a High Speed Composite Flywheel Energy Storage System,” has been reviewed in final form. Permission, as indicated by the signatures and dates given below, is now granted to submit final copies to the College of Graduate Studies for Approval.

Major Professor: \_\_\_\_\_ Date: \_\_\_\_\_

Matthew Riley, Ph.D.

Committee Members: \_\_\_\_\_ Date: \_\_\_\_\_

Michael Santora, Ph.D.

\_\_\_\_\_ Date: \_\_\_\_\_

Gabriel P. Potirniche, Ph.D.

Department

Administrator: \_\_\_\_\_ Date: \_\_\_\_\_

Steven Beyerlein, Ph.D.

## Abstract

High speed flywheel energy storage systems (FESS) are predicted to outperform other energy storage systems in energy density, environmental impact, and lifetime. Proper development can transcend FESS into the new standard of energy storage for space and terrestrial applications. Maintaining structural integrity of a high speed FESS requires the use of high strength, light weight composites. A hubless field regulated reluctance machine (FRRM) FESS requires a magnetically permeable material and irregular geometry to electromagnetically spin the flywheel. This thesis describes modeling of mechanical and electromagnetic changes created by geometry and material necessary to produce rotation. Incorporating permeable composite materials is examined to categorize characteristics favoring design constraints. The design space is explored and mapped with the use of an interpolation process known as Kriging. After future constraints are determined, the Kriging blueprint will be helpful in determining optimal material and geometry to efficiently maximize energy stored by the flywheel.

## Acknowledgements

I would like to thank my professors, colleagues, family, and friends. The support they have given is much appreciated. I am especially thankful to Mercedes Cane. She has been my rock through my education. I would like to extend a special thank you to Dr. Matthew Riley. I am grateful for his collaboration and guidance through the completion of my graduate degree. I would also like to thank Dr. Michael Santora and Dr. Gabriel P. Potirniche for taking the time to read this thesis and listen to my defense.

This is a team project, and I could never image doing this work alone. I would like to extend my gratitude to the other members of this project for their assistance and direction:

Dr. Christine Berven

Dr. Herbert Hess

Dr. Joe Law

David Arnett

Nicholas Bachus

Cade Smith

Matt Philips

Shea Morrison

## Table of Contents

Authorization to Submit.....	ii
Abstract .....	iii
Acknowledgements .....	iv
Table of Contents .....	v
List of Figures .....	viii
List of Tables.....	xi
Definition of Terms.....	xii
1      Introduction .....	1
1.1     Flywheel Energy Storage Systems .....	2
1.2     University of Idaho FESS.....	3
1.3     University of Idaho High-Speed FESS .....	8
1.4     Thesis Objectives .....	9
1.5     Scope .....	10
2      Composites.....	12
2.1     Composites Categories .....	13
2.2     Discontinuous-Randomly Oriented Composite Mechanics .....	15
2.2.1     Discontinuous-Randomly Oriented Composite Moduli .....	16
2.2.2     Composite Strength.....	20
3      Uniaxial Tension Testing of Composites.....	27
3.1     Composite Specimen Design.....	27
3.2     Composite Mold Design.....	31
3.3     Composite Molding Methodology .....	34
3.4     Strain Gage Measurements.....	39
3.4.1     Poisson's Ratio.....	40

3.4.2	Young's Modulus.....	43
3.5	Data Collection.....	44
3.6	Composite Testing Results .....	47
3.7	Composite Mechanics Discussion and Conclusion.....	53
4	Mechanical Rotor Model.....	55
4.1	HSFESS Mechanical Composition .....	56
4.2	Axisymmetric Rotor Model.....	57
4.3	Localized Stress Model Approach.....	59
4.3.1	Simple FEA Model .....	61
4.3.2	Model Adjustments: Kaschmitter's Simulation.....	65
4.4	Localized Stress Model .....	67
4.4.1	Kriging/Gaussian Process .....	68
4.4.2	Localized Stress Model Creation .....	73
4.4.3	Empty Chevron Model.....	77
4.4.4	Filled Chevrons, No Separation Model.....	79
4.4.5	Filled Chevrons, Bonded Model .....	82
4.5	Localized Stress Model Conclusion .....	85
5	Electromagnetic Rotor Model .....	89
5.1	FRRM Composition .....	89
5.2	LSFESS Electromagnetic Model.....	90
5.3	Magnetic Permeability Experiment.....	91
5.4	FEA Model Creation .....	94
5.5	Electromagnetic Stochastic Model.....	96
5.6	Electromagnetic Rotor Model Conclusion .....	101
6	Summary and Future Work.....	103

6.1	Summary .....	103
6.2	Future Work .....	105
Appendix A: Mechanical Testing Information .....		112
Appendix B: Specimen Data Collection Procedure .....		116
Appendix C: Toroid Permeability Test .....		124

## List of Figures

Figure 1: Energy density comparison for energy storage systems [3] [4] [5].....	2
Figure 2: Low speed flywheel energy storage system diagram [7] .....	4
Figure 3: Energy loss mechanisms.....	5
Figure 4: High temperature superconductor plate.....	6
Figure 5: 1mm rotor/stator airgap .....	7
Figure 6: The University of Idaho's assembled low speed flywheel energy storage system ....	8
Figure 7: Types of fiber reinforced composites [14] .....	14
Figure 8: Randomly oriented fibers [14].....	16
Figure 9: Convention for fiber orientation [14] .....	17
Figure 10: Dependence of modulus ratio ( $E/E_I$ ) on volume fraction [14].....	18
Figure 11: Young's modulus comparison predictions [14] .....	19
Figure 12: Voronoi cell approximation [14] .....	22
Figure 13: Representative volume element [14] .....	24
Figure 14: Tsia-Hill, maximum stress, and maximum strain criterions [14] .....	24
Figure 15: Dogbone style specimen .....	28
Figure 16: Gripping systems for tensile specimens .....	28
Figure 17: Machine attachment for composite specimen .....	29
Figure 18: Final specimen geometry and SolidWorks static simulation .....	30
Figure 19: Machine attachments, 3D printed specimen, and hardware .....	31
Figure 20: Mold diagram .....	33
Figure 21: Inside machined molds .....	34
Figure 22: Completed molds .....	34
Figure 23: Latin hypercube sampling example, 2D .....	36
Figure 24: Chen, equation 2.29, effect chopped fiber volume fraction on normalized strength .....	36
Figure 25: Chen, equation 2.29, effect iron particle volume fraction on normalized strength	37
Figure 26: Specimens after curing .....	38
Figure 27: Strain gage resistance .....	39
Figure 28: Rectangular rosette and delta rosette .....	40
Figure 29: Installed stacked rosette strain gage .....	40

Figure 30: Stacked rosettes [31].....	42
Figure 31: Stress-strain curves for brittle (a) and ductile (b) materials .....	44
Figure 32: Data acquisition circuit.....	45
Figure 33: Fractured composite specimen .....	46
Figure 34: Control Specimen stress vs strain .....	46
Figure 35: Elastic modulus vs iron particle and chopped fiber reinforcement .....	48
Figure 36: Lees' Strength vs iron particle and chopped fiber reinforcement .....	49
Figure 37: Chen's Strength vs iron particle and chopped fiber reinforcement.....	49
Figure 38: Poisson's ratio vs iron particle and chopped fiber reinforcement.....	50
Figure 39: Composite flywheel diagram with multiple rings [38].....	57
Figure 40: Tapered composite flywheel [12] .....	59
Figure 41: Salient poles and chevron inductance.....	60
Figure 42: Rotor stress concentrations .....	61
Figure 43: Analytical and numerical comparison of circumferential stress vs radial distance	62
Figure 44: Analytical and numerical comparison of radial stress vs radial distance .....	63
Figure 45: Analytical and numerical comparison of radial displacement vs radial distance...	64
Figure 46: FEA and Kaschmitter's model comparison of stress vs radial distance.....	66
Figure 47: FEA and Kaschmitter's model comparison of radial displacement vs radial distance.....	66
Figure 48: Diagram of semivariogram.....	70
Figure 49: Semivariance of empirical relationship fitted to observed bins .....	71
Figure 50: Rotor design variables .....	74
Figure 51: Semivariogram of stress fits: empty chevrons.....	78
Figure 52: Semivariogram of displacement fits: empty chevrons .....	79
Figure 53: Semivariogram of stress fits: filled chevrons no separation model.....	81
Figure 54: Semivariogram of displacement fits: filled chevrons no separation model.....	82
Figure 55: Semivariogram of stress fits: filled chevrons bonded model .....	84
Figure 56: Semivariogram of displacement fits: filled chevrons bonded model .....	85
Figure 57: FRRM topology [5] .....	90
Figure 58: Toroid specimen [31].....	92
Figure 59: Toroid test setup .....	93

Figure 60: Linear extrapolation of permeability data .....	94
Figure 61: Stator winding topology [7].....	96
Figure 62: Semivariogram of chevron $B$ field .....	97
Figure 63: Semivariogram of rotor/stator airgap $B$ field.....	98
Figure 64: Semivariogram of rotor midpoint $B$ field .....	99
Figure 65: Semivariogram of stator maximum $B$ field .....	100

## List of Tables

Table 1: Specimen volume fractions and mixture ratios.....	38
Table 2: Mass results of specimens.....	39
Table 3: Control specimen results.....	47
Table 4: Elastic modulus and tensile strength results .....	47
Table 5: Elastic modulus error values .....	51
Table 6: Strength error values .....	52
Table 7: Poisson's ratio error values .....	53
Table 8: Simple FEA model inputs.....	62
Table 9: Geometric constraints and design variable bounds.....	75
Table 10: Tested Materials.....	76
Table 11: Semivariogram of stress characteristics: empty chevrons .....	78
Table 12: Semivariogram of displacement characteristics: empty chevrons .....	79
Table 13: Filled chevron material iterations .....	80
Table 14: Semivariogram of stress characteristics: filled chevrons no separation model .....	81
Table 15: Semivariogram of displacement characteristics: filled chevrons no separation model .....	82
Table 16: Filled chevron (bonded) material iterations .....	83
Table 17: Semivariogram of stress characteristics: filled chevrons bonded model .....	84
Table 18: Semivariogram of displacement characteristics: filled chevrons bonded model....	85
Table 19: Permeability experimental results.....	93
Table 20: FEMM constrains and input variable ranges .....	95
Table 21: FEMM materials list .....	96
Table 22: Semivariogram characteristics of chevron <i>B</i> field .....	97
Table 23: Semivariogram characteristics of rotor/stator airgap <i>B</i> field .....	98
Table 24: Semivariogram characteristics of rotor midpoint <i>B</i> field.....	99
Table 25: Semivariogram characteristics of stator maximum <i>B</i> field.....	100

## Definition of Terms

FESS	Flywheel energy storage system
LSFESS	Low speed flywheel energy storage system
HSFESS	High speed flywheel energy storage system
HTSC	High temperature superconductor
FRRM	Field regulated reluctance machine

## 1 Introduction

Energy is used in nearly every aspect of modern civilization, from exploring new concepts to staying warm at night. Storing that energy has always been a part of human activities.

Energy storage is the capture of generated energy for a later use. Several sources of energy storage exist, ranging from dried wood to a fuel cell. When exploring new worlds, like the lunar surface, energy becomes even more valuable. Energy production and storage becomes exponential expensive when transporting these systems off planet. To support the exploration of space, the National Aeronautics and Space Administration (NASA) has been working to develop a reliable, efficient, energy dense storage system. The energy storage device enables explorers to capture excess energy created during peak generation hours and use it when needed through energy inert periods. An energy storage system used in space needs to be low-maintenance, effective and safe because of the risks associated with space exploration.

Space has extreme conditions. The lack of an atmosphere on the moon results in temperatures on the lunar surface ranging from 400K in the daylight and 100K in the darkness [1]. The moon cycles through 14 earth days of sunlight and 14 earth days of darkness which makes the extreme conditions difficult for some energy storage devices to transcend. Sustainable sources of power production on the lunar surface include solar and nuclear. The long periods of darkness eliminates solar generation as a sole power provider. Nuclear power plants cannot operate during the high daylight temperatures to prevent overheating of the nuclear core. The intermittent energy power sources expose the need to store energy for a later use.

Energy storage system types have tradeoffs of power density, energy density, life, charge/discharge cycles, and cost [2]. There are many viable storage systems including batteries, compressed air, pumped hydroelectricity, and supercapacitors. The energy density of some energy systems are illustrated in Figure 1. A flywheel energy storage system (FESS) requires a lighter payload for installation than NASA's current storage system, batteries [3]. A FESS is a potentially energy dense and efficient storage system that can be used on earth and for space exploration.

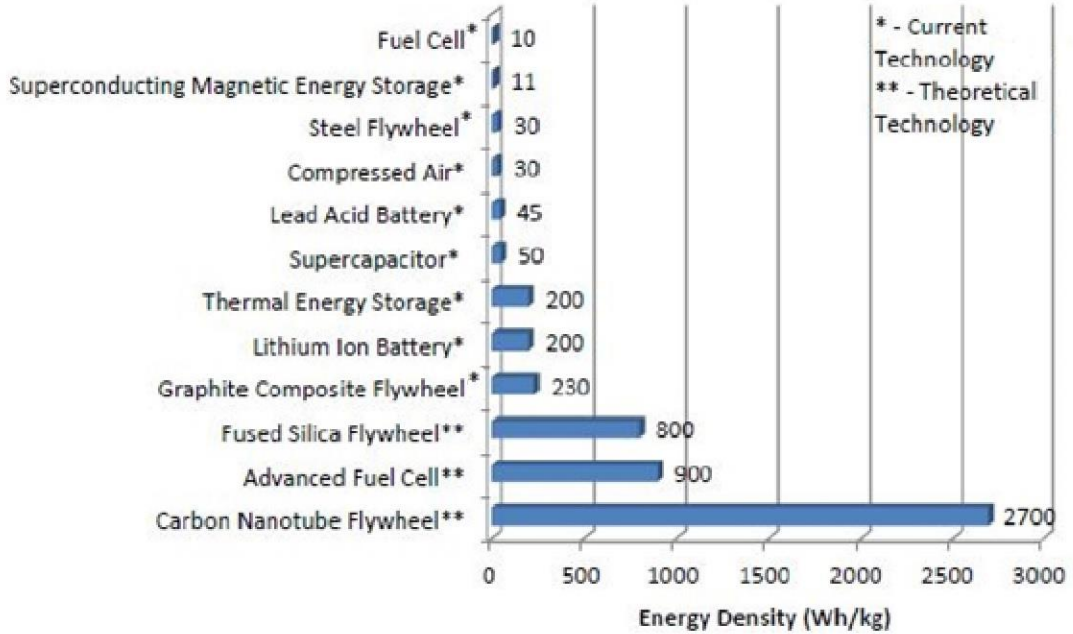


Figure 1: Energy density comparison for energy storage systems [3] [4] [5]

## 1.1 Flywheel Energy Storage Systems

A flywheel is a rotating device that is used to mechanically store rotational energy. Flywheel technology dates back to the Industrial Revolution [6]. Since then, flywheels have been used from automobiles, to potter's wheels, to toys. These systems all use a flywheel to transfer mechanical energy. Current applications include electric vehicles and stationary backup power applications to improve electric grid power quality issues [3].

FESS's store mechanical energy in the form of a cylindrical rotating mass. The kinetic energy,  $KE$ , is related to the inertia,  $I$ , and rotational speed,  $\omega$ , of the flywheel:

$$KE = \frac{1}{2}I\omega^2 \quad 1.1$$

The equation reveals it is more energy profitable to increase the speed of the flywheel than it is to increase the moment of inertia. A flywheel with a high strength to weight ratio is now becoming possible with the progression of material science.

The mechanical energy stored by the flywheel is extracted into electrical energy by use of an electric machine. The electric machine is used as either a motor or generator. If the machine is being operated as a motor, electrical energy is being transferred into the flywheel by rotating it faster. If the machine is operating as a generator, the energy in the rotating object is converted to electrical energy [3].

A FESS has many advantages when comparing the energy storage systems in Figure 1 [4]:

- No periodic maintenance is required
- Long life expectancy of 20+ years
- High energy and power density
- Low environmental impact by excluding the use of hazardous materials
- Wide operating temperature range
- Rapid discharge rates without degradation

With all of the advantages, NASA has deemed the University of Idaho with investigating and creating a FESS as a viable storage system

## **1.2 University of Idaho FESS**

NASA has provided funding to the University of Idaho under the Steckler Space Grant to research and develop a FESS. The grant is currently under phase III which is an extension of research for the use of a hubless low-speed FESS. Other goals of the project are to advance education for both undergraduate and graduate students in a STEM environment, promote interdisciplinary work, and to develop, test, and optimize a high speed FESS. The research team is currently formed of Electrical and Computer Engineering, Mechanical Engineering, and Physics professors and students. In phase II of the Steckler Space Grant, The University of Idaho has proven the design of a hubless low-speed FESS (LSFESS) and is currently testing this device.

The University of Idaho's LSFESS is intended to rotate at 1800rpm, but has been designed to operate at speeds of up to 5000rpm [7]. In a hubless flywheel design, a shaft is absent. A hubless flywheel design designates the topology of the machine as an inside-out design. In an inside-out design, the rotor, or flywheel, spins about the stationary stator. This topology has the electromagnetic force originating in the stator by the use of electrical windings. The stator

turns the electrical energy into mechanical energy by rotating the flywheel, and also turns the mechanical energy back into electrical energy. A diagram of the University of Idaho's LSFESS is shown in Figure 2.

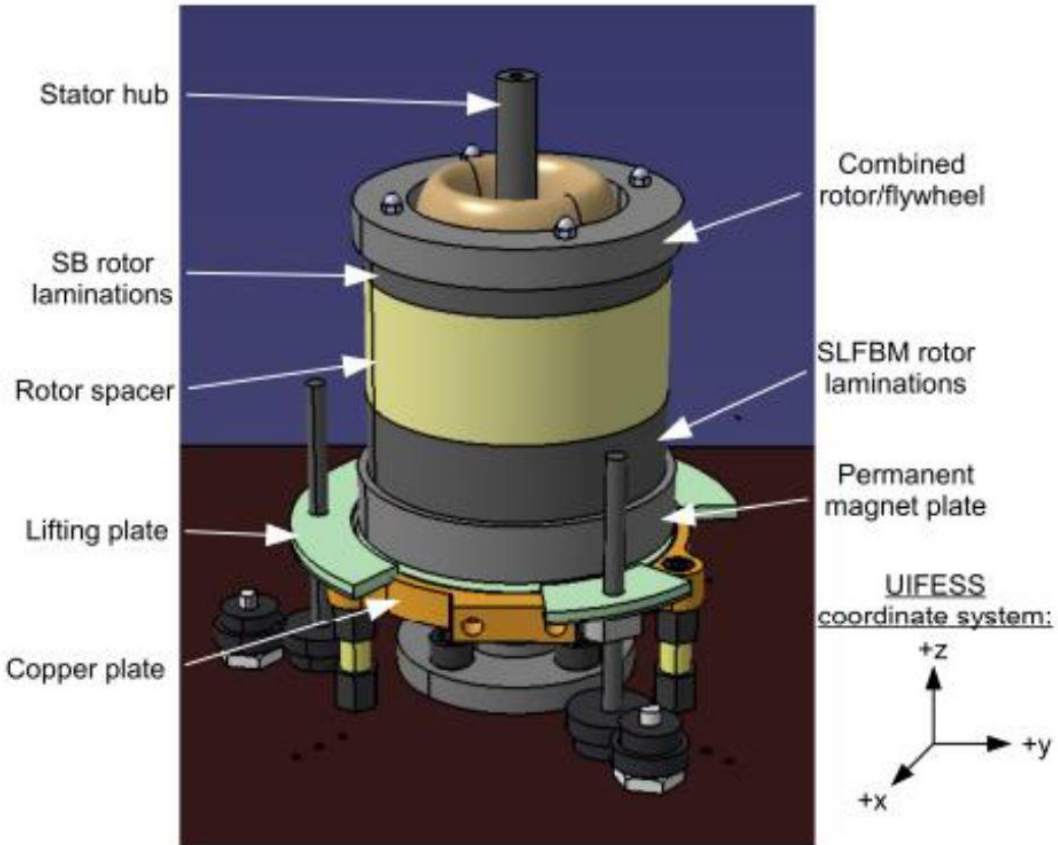


**Figure 2: Low speed flywheel energy storage system diagram [7]**

FESS possess energy conversion and storage challenges that diminish efficiency of the device. The energy loss mechanisms include electrical, magnetic, bearing and wind drag as shown in Figure 3. The LSFESS uses various subsystems designed to reduce any inherent losses to improve overall efficiency. The LSFESS uses a magnetically and electrically efficient field regulated reluctance machine (FRRM) FESS topology [8], a passive magnetic bearing levitation system and an active magnetic bearing system to reduce bearing loss, and a vacuum containment system to reduce wind drag. When the FRRM is operating, a significant amount of heat is produced by the stator windings. The higher temperature also leads to a lower efficiency. Cold water is pumped through the stator hub to remove heat away from the windings and increase the machine's efficiency.

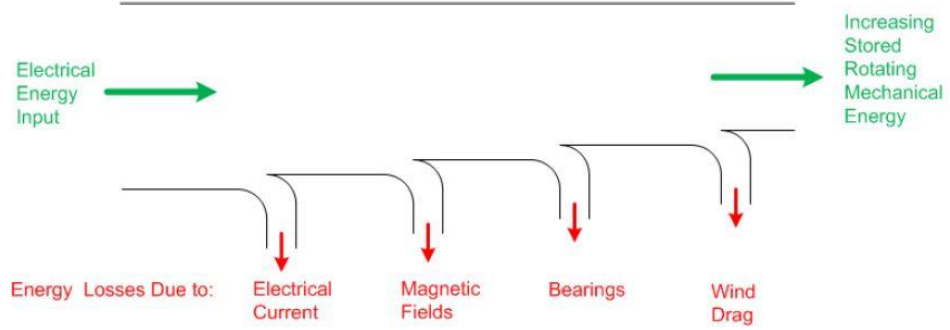


**Figure 3: Energy loss mechanisms**

The FRRM's purpose is to efficiently convert the electrical signal applied to the stator windings into kinetic energy stored in the spinning rotor. In phase I of the project, multiple machines were considered for the electromagnetic component of the FESS system. The top machines were elected based on the expected machine force density. After comparing the force densities, the FRRM was selected as the machine for the University of Idaho's FESS [8].

The passive magnetic bearing (PMB) and active magnetic bearing (AMB) systems are used to decrease friction that is produced under the use of mechanical bearings. A permanent magnetic plate and high temperature superconductors (HTSC) operate the PMB system. This frictionless bearing controls the z- direction of the rotor while allowing rotation about the z-axis. The PMB operates using HTSC and permanent magnets oriented in a Halbach array. A Halbach array orients permanent magnets in specified directions which ultimately increases the gradient and intensity of the magnetic field [9]. The interaction of the magnets and HTSC creates a force that pins the HTSC and magnet together. If either of the components are fixed, then the other is levitated with the force. The PMB force requires that the HTSC be cooled below a critical temperature to provide the pinning effect. The HTSC's critical temperature is 91K [10]. A copper plate and liquid nitrogen are used to achieve the critical temperature of the HTSC. A schematic of the HTSC copper plate is shown in Figure 4



**Figure 4: High temperature superconductor plate**

The inside-out, hubless design allows for movement in the x-y plane. The PMB provides some restoring forces in the x-y plane, but the AMB provides most of the restoring and rotating forces. The stabilizing bearing (SB) and self-bearing machine (SLFBM) make up the AMB of the University of Idaho's LSFESS. The SB and SLFBM are not one chunk of material, but thin layers of m-36 electrical silica steel known as laminations. The laminations decrease eddy currents in the FRRM. The eddy currents are magnetic fields that loop back into the parent magnetic source [11]. The AMB is a frictionless bearing that provides support by means of magnetic forces. The absence of physical contact eliminates mechanical wear, reducing the need for maintenance. The AMB relies on feedback to control the forces provided to the flywheel. The feedback comes from position sensors that tell the electronics where the rotor is at. The sensors inform the power electronics how the gap between the rotor and stator is changing. To operate the LSFESS efficiently, the gap must be maintained at 1 mm, illustrated in Figure 5. The dynamics of the flywheel are built into the system to tell the AMB how to respond to realign the flywheel according to different positions of the rotor [7].

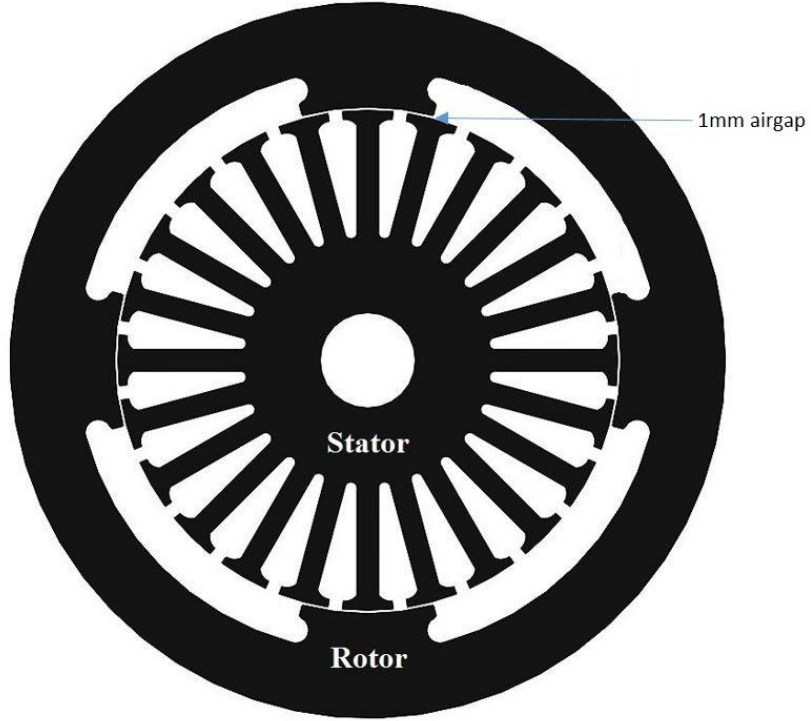


**Figure 5: 1mm rotor/stator airgap**

A vacuum containment system minimizes the windage losses by achieving vacuum conditions of  $10^{-4}$  Torr [5]. The torque created by the FRRM is more efficient in a vacuum environment and the chamber semi-mimics the lunar surface. The chamber also serves as a containment system to protect against failure at low rotational speeds. The vacuum chamber and overall topology of the University of Idaho's LSFESS is shown in Figure 6.

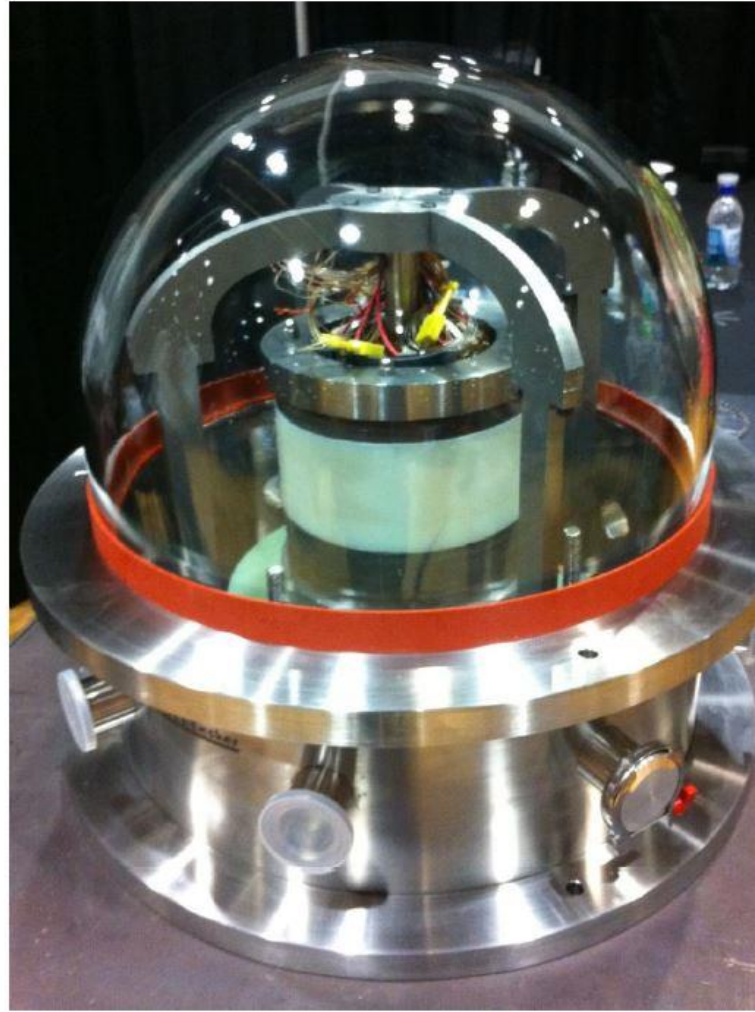


**Figure 6: The University of Idaho's assembled low speed flywheel energy storage system**

### **1.3 University of Idaho High-Speed FESS**

Phase III of the Steckler project is to evaluate the performance of the LSFESS and then design, build, and test a high-speed flywheel energy storage system (HSFESS). The LSFESS is a proof of concept design to progress work into a more energy dense HSFESS. The HSFESS will be designed to spin at high rotational speeds (<10,000rpm) to increase energy storage. The geometry of the rotating assembly will be designed to withstand the large centrifugal forces with minimal deflection, so the use of high strength materials is expected.

Brenden F. Kaschmitter [12] has completed initial modeling work at the University of Idaho to investigate a HSFESS. The model includes the use of wrapped fiber composites to explore

carbon fiber for the high strength application while simultaneously reducing weight. High strength materials are needed to withstand the stresses induced by high rotational speeds. The model incorporates multiple physical rings of different materials to optimize the geometry of the flywheel. Two optimizations are created to meet specific requirements. One is to maximize the kinetic energy storage of the system given operating constraints, the other is to minimize the displacement at the inner surface of the rotor. Kaschmitter's model provides an overall geometry of the rotor that will meet the specified requirements such that material failure does not occur. The geometry provides cylindrical dimensions of the optimized rotor, but does not take into account the needed jagged geometry of the rotor shown in Figure 5.

## **1.4 Thesis Objectives**

Overall dimensions of the HSFESS have been determined to maximize kinetic energy storage by modeling the rotor as a perfect cylinder. The work submitted by Kaschmitter is an excellent starting place to refine design of the HSFESS. The LSFESS is a proof of concept design that does not have the mechanical obstacles the HSFESS imposes. The forces induced on the rotor during high speed operation are a significant limiting factor of the HSFESS design.

The primary objective of the work presented in this thesis is to explore and develop models based on electromagnetic topology of the HSFESS. The models will incorporate the needed geometry of the rotor for interaction with the FRRM. The increased stress concentrations created around sharp corners in the rotor will be quantified and mapped. The map will integrate material properties and rotor geometry to explore more desirable designs. The investigation will include displacement, stress, and magnetic field density maps that correlate geometry, material characteristics and operating conditions of the HSFESS. Different models will be created to explore the possibility of using iron impregnated composite materials. Composite materials can reduce weight, making the characteristics mechanically desirable for rotating components. The added iron has the ability to enhance electromagnetic characteristics compared to carbon fiber composites. The work presented will require a mechanical and electromagnetic model of the rotor. Three numerical mechanical models will be presented to observe and classify the distinguishing characteristics of an iron impregnated composite material being used as the electromagnetic operating component of the rotor.

The models will incorporate different materials and geometry to explore the effects of each. A numerical electromagnetic model is also developed to explore the effects of geometry, material characteristics and operating parameters. The electromagnetic model presented is used to explore the effects of magnetic field density of an iron impregnated composite material. The models will use simulated data to create a regression model governed by prior covariances known as a Kriging/Gaussian process. The models will estimate stochastic predictions based on provided inputs to explore untested operating conditions. The maps will be a guide to resolve the incorporation of an iron impregnated composite material into the HSFESS.

The second objective is to provide experimental procedures to test unknown material characteristics required as model inputs. The inputs are elastic modulus, Poisson's ratio, tensile strength, and magnetic permeability. The approach will exercise outlined procedures and compare testing results to formulated theory.

## **1.5 Scope**

The work of this thesis is implemented under phase III of the Steckler Space Grant provided by NASA. Phase I provided analytical and experimental proof that iron energy losses could be reduced during idling periods. Various machine topologies were also explored during phase I, and the FRRM was selected for the FESS. Phase II is included as part of the work presented by Bridget Wimer [5], Brent Kisling [7], and Kevin Rammus [13]. Phase II had the goal of designing, and building a proof of concept low speed, integrated, hubless flywheel and machine. The proof of concept FESS is used for future teams to explore control algorithms and test degaussing routines. Phase III is to evaluate the performance of the LSFESS and then design, build and test a HSFESS. The results of phase II are the building blocks of phase III. A list is included that supplies main results of theses from Kaschmitter [12], Wimer [5], Kisling [7], and Rammus [13].

This thesis:

- Composite material behavior
- Uniaxial tension testing composites
- Mechanical rotor model

- Electrical rotor model

Kaschmitter [12]:

- Numerical model to define stress state of cylindrical flywheel
- Multiple physical ring modeling to incorporate high strength composites
- Optimizations to maximize energy storage and minimize radial deflection

Wimer [5]:

- FRRM theory and design
- SLFBM and SB force derivations
- Dynamic model of FESS

Kisling [7]:

- SLFBM machine axial control
- SLFBM machine rotation control
- SB machine control

Rammus [13]:

- Power electronics
- Sensor component selection
- Vacuum chamber implementation

Chapter 2 of this thesis contains an overview of composite mechanics favoring short fiber and particulate composites. A uniaxial testing procedure to collect needed material characteristics based on a molded composite material is located in chapter 3. An overview of the work previously performed on the University of Idaho's HSFESS, a modified model to incorporate precise flywheel geometry, and an overview of the 3 stochastic maps to explore untested design space are all discussed in chapter 4. Chapter 5 expands the rotor model to investigate electromagnetic effects of geometry and material properties. Chapter 6 presents a summary and conclusions reached from the models along with recommendations for future work.

## 2 Composites

The four main categories of structural materials are metals, ceramics, polymers and composites. Composites consist of two or more materials combined together to generate a new compound. Composites are typically made from various combinations of the other structural materials [14]. People have been making composites for many thousands of years. An early example is a mixture of mud and straw called adobe [15]. This composite was used to build homes in Egypt as early as 3800 B.C.; some of those structures are still standing today [16]. Over the past 50 years composites have been steadily increasing in importance over metals because of their characteristics. Composite materials often have higher strength to weight ratios increasing the specific strength of the material. Many composites can also be manufactured with less cost than other materials. Because composites are composed of 2 or more materials, they can be formulated to meet the needs of a specific application.

The purpose of this chapter is to introduce different classes of composites with a brief overview of their characteristics. Mechanics for discontinuous randomly oriented composites is discussed and an outline of moduli and strength terms are presented. Equations predicting composite characteristics will also be delivered. The reason for this mechanics discussion is to provide a path to use these mechanisms for the high speed flywheel energy storage system (HSFESS). Mechanics approximations for strength and moduli are compared with uniaxial test specimens for accuracy. Strength and moduli expressions are necessary for rotor design. In the chapter 4, FEA simulations are used to determine rotor strength and mechanics characteristics needed for the simulations.

Composites are very effective because many materials are stronger and stiffer in small fiber form rather than in bulk form. The small scale increases relative strength by decreasing relative flaw population. This in turn increases fracture toughness [17]. Using small reinforcements increases the strength of the material, but a binding agent is needed to hold them together.

## 2.1 Composites Categories

The two main categories of composites are fibrous reinforced and particulate reinforced. These composites both exist in a binder that suspends the reinforcement material. This glue-like substance is called matrix material. The matrix material also acts as a barrier for the reinforcement, protecting it from the external damage and environmental attack. The designer is allowed to choose from a variety of matrix and strengthening materials to achieve a combination material with desired properties. Composites can have high strength to weight ratios while being able to be customized for density, stiffness, toughness, and stability.

Fiber reinforced composites have the ability to be very strong, but light. This can be obtained by using a small, but strong, carbon fiber embedded into a less dense matrix. Normally, the matrix has a much lower elastic modulus than the fiber. This allows the fiber to carry most of the force. Aligning all of the fibers in the same direction allows this type of composite to be strongest in tension along the length of the fiber, but much weaker in the other directions due to the anisotropic nature of the composite. Anisotropy is the property of being directionally dependent. Metals and glasses are typically considered isotropic materials. This means their properties are uniform in all directions. The behavior of isotropic materials is easier to predict, but anisotropic materials can be tailored to the forces an object is experiencing.

The need for customizing mechanical properties has introduced various types of fiber composites: continuous, woven, chopped and hybrid as shown in Figure 7 [14].

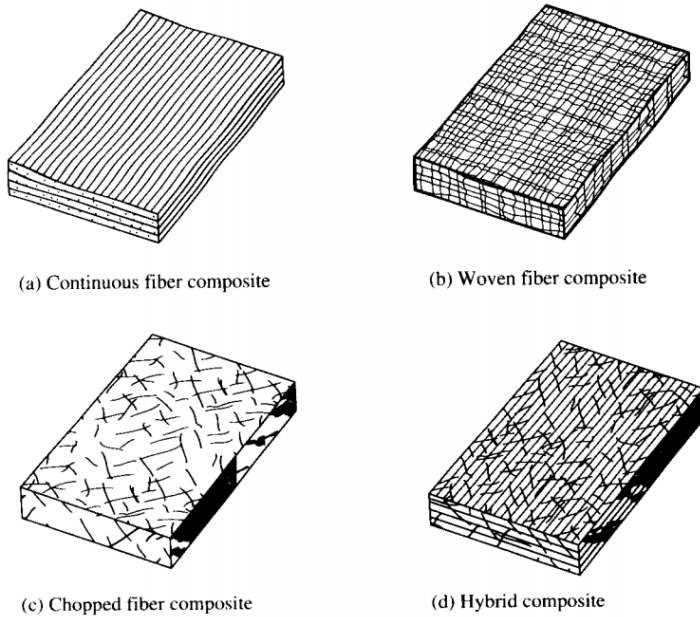


**Figure 7: Types of fiber reinforced composites [14]**

Continuous fiber composite are constructed by orienting fibers along a cardinal direction. Single fiber/matrix sequences, laminae, are assembled to build a laminate. While this composite type has high strength along the fiber direction, the other directions are much weaker. The laminate has the potential to separate, called delamination, due to unwanted matrix loading [14]. Woven fiber composites have fibers oriented in multiple directions, but still run the continuous length of the composite. Woven composites are less likely to delaminate, but the strength and stiffness are sacrificed because of the fiber orientation [14]. Chopped fiber composites have short fibers randomly oriented in the matrix material. In a sample large enough to the fiber size, the fiber randomness exhibits a 3D isotropy [18]. Hybrid Composites contain more than one type of fiber in a single matrix material.

Particle composites consist of one particle material dispersed in a matrix material. Particles can have any shape or size, but are generally spherical. Particle composites do not have the high strength mechanical properties like lamination stacks, but industrial interests for using these composite materials are growing. Particle composites have economic advantages and design flexibility over fibrous composites. Easier manufacturability enables the production of complex parts which cannot be made with traditional stack laminations [19]. The particulates

are small relative to the size of the structure and are assumed to be evenly distributed throughout. This randomness allows this type of composite to be considered isotropic.

Further discussion on composites is weighted toward chopped fiber composites and particle composites because of the properties that can be achieved. Their strength properties are less desirable than continuous fiber composites, but other properties are desirable for this application. The particulate reinforcements are capable of characteristics that favor electromagnetic permeability, while the fiber reinforcements increase strength. The HSFESS uses the stator and rotor combination to apply an electromagnetic flux field that spins the flywheel. A lower magnetic permeable material in the rotor, increases the power to apply a torque to rotor. A main goal of the overall project is to store and draw energy from the flywheel efficiently, making permeability a desirable composite characteristic.

## **2.2 Discontinuous-Randomly Oriented Composite Mechanics**

Short fiber reinforced or particulate reinforced composites are classified as discontinuous, randomly oriented, reinforced composites. These composites are not likely to be used in structural applications, but they have many characteristics that make them useful for other applications. The randomly oriented composites still exhibit a high strength to weight ratio and are much easier and cheaper to manufacture than continuous fiber composites. Discontinuous composites are able to be mixed with liquid matrix and be molded into complex geometric contours. Continuous fiber lamina are unable to conform to complex shapes without being damaged or distorted [14]. Discontinuous composites are easily mixed with liquid matrix resin and the mixture is injected or compressed into molds to produce parts with complex shapes.

Material choices and volume fractions give the designer flexibility when using composite materials. A large range of flexibility requires approaches that characterize the macroscopic properties of a composite material without the need to test individual properties. The following analysis assumes the following characteristics for fibrous and particulate reinforcements [14]:

- The matrix material is isotropic
- Reinforcement and matrix materials are linear elastic

- Perfect bonding between reinforcement and matrix
- Reinforcement and matrix are homogeneous
- Reinforcement volume fraction is constant throughout composite
- The macroscopic characteristics of the composite are homogeneous, and linear elastic

Since the packing arrangement of randomly oriented reinforcements is statistically random, the properties are the same in any direction for the material. Because of their isotropic nature, analyzing discontinuous reinforced composites requires geometrically averaged relationships. For the orientation of the fibers to be random in a 3D sense, the fiber length,  $L$ , must be much less than the thickness of the part,  $t$ , as illustrated in Figure 8(a). If the thickness is much smaller than the length of the fiber, fibers are only randomly oriented in two directions as shown in Figure 8(b).

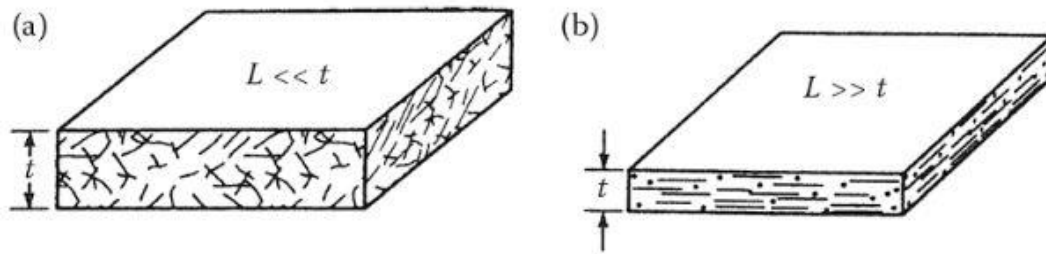


Figure 8: Randomly oriented fibers [14]

### 2.2.1 Discontinuous-Randomly Oriented Composite Moduli

Nielsen and Chen used the averaging concept to develop a relationship for a geometrically averaged Young's modulus,  $\tilde{E}$ . This planar modulus is the same as the in plane Young's modulus of the isotropic composite. The relationship is given by

$$\tilde{E} = \frac{\int_0^\pi E_x d\theta}{\int_0^\pi d\theta} \quad 2.1$$

where  $E_x$  is the off-axis Young's modulus and  $\theta$  is the angle of the oriented fiber from a referenced axis [20]. Orientation sign convention for  $\theta$  follows the general engineering representation of the right hand rule as shown in Figure 9. The axes 1 and 2 represent the longitudinal and transverse directions of the fiber, respectively. The individual fibers are an

elastic orthotropic material. Orthotropic materials possess three orthogonal planes of material symmetry. An elastic orthotropic material's constants do not change at a point under a rotation of  $180^\circ$  [14]. The notation  $\phi_{ij}$  states the property of the material with  $i$  indicating reinforcement and  $j$ , being 1 or 2, to indicate the longitudinal or transverse directions. If  $j$  is not present, the material is assumed isotropic.

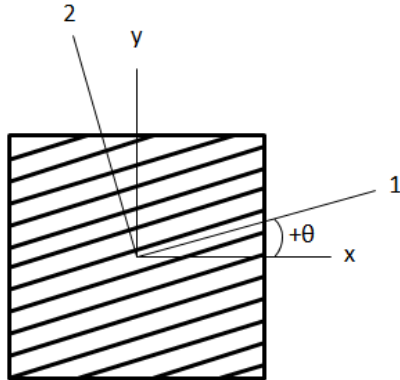


**Figure 9: Convention for fiber orientation [14]**

Nielsen and Chen reported that the averaged modulus,  $\tilde{E}$ , for a randomly oriented composite was much lower than the longitudinal modulus  $E_1$  and transverse modulus  $E_2$  [14]. The relationship between fiber volume fraction,  $\tilde{E}/E_1$  and  $E_f/E_m$  is shown in Figure 10.  $E_f$  represents the fiber modulus and  $E_m$  represents the matrix modulus. Because Nielsen and Chen's analysis is based on a continuous fiber model, the predicted modulus,  $\tilde{E}$ , is only dependent on fiber orientation and not fiber length [14]. Nielsen and Chen reported that Equation 2.1 predicted values lower then experimental values.

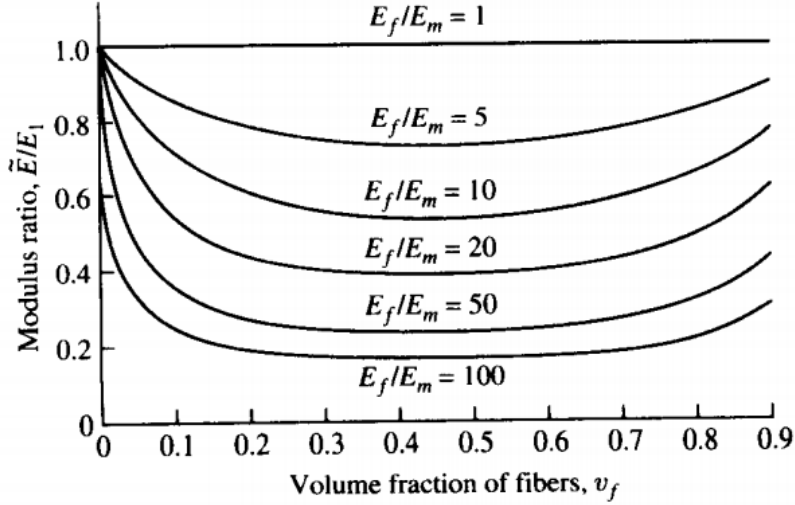


Figure 10: Dependence of modulus ratio ( $\tilde{E}/E_1$ ) on volume fraction [14]

To predict the stiffness of the linear variation for the longitudinal and transvers modulus,  $E_1$  and  $E_2$  respectively, and expanding to two reinforcements, the following rule of mixtures is used [21] [22]:

$$E_1 = E_{f1}v_f + E_{g1}v_g + E_m v_m \quad 2.2$$

$$\frac{E_2}{E_m} = \frac{1 + \xi(\eta_c v_f + \eta_g v_g)}{1 - (\eta_c v_f + \eta_g v_g)} \quad 2.3$$

where,

$$\eta_c = \frac{\frac{E_{f2}}{E_m} - 1}{\frac{E_{f2}}{E_m} + \xi} \quad 2.4$$

$$\eta_g = \frac{\frac{E_{g2}}{E_m} - 1}{\frac{E_{g2}}{E_m} + \xi} \quad 2.5$$

The equations are under the assumption that the matrix modulus,  $E_m$ , is isotropic and the fiber moduli are orthotropic. That is that the longitudinal fiber moduli,  $E_{f1}$  and  $E_{g1}$ , do not necessarily equal the transverse fiber modulus,  $E_{f2}$  and  $E_{g2}$  [14]. Variables  $v_f$ ,  $v_g$ , and  $v_m$  are the volume fractions of the reinforcements and matrix. A curve fitting parameter,  $\xi$ , is

dependent on fiber packing arrangement. Halpin and Tsai found that the value  $\xi = 2$  gave an excellent fit to the transverse modulus of a square array of circular fibers [23].

Evaluating equation 2.1 was performed by Tsai and Pagano by using invariant forms along with quasi-isotropic lamina theory [24]. The approximate expressions are shown to be [14]:

$$\tilde{E} = \frac{3}{8}E_1 + \frac{5}{8}E_2, \quad \tilde{G} = \frac{1}{8}E_1 \frac{1}{4}E_2 \quad 2.6$$

where  $\tilde{G}$  is the geometrically averaged shear modulus of the composite. The lateral strain and axial strain are still proportional through Hooke's law. Poisson's ratio for the composite,  $\tilde{\nu}_c$ , is found by using the following isotropic equation:

$$\tilde{\nu}_c = \frac{\tilde{E}}{2\tilde{G}} - 1 \quad 2.7$$

Equations 2.6 and 2.7 were used to estimate the elastic modulus of randomly oriented boron fiber-enforced epoxy. These results compared favorably with experimental results as shown in Figure 11. Manera also reported good agreement with a different set of micromechanics equations for  $E_1$ ,  $E_2$ ,  $G_{12}$ , and  $\nu_{12}$  [25].

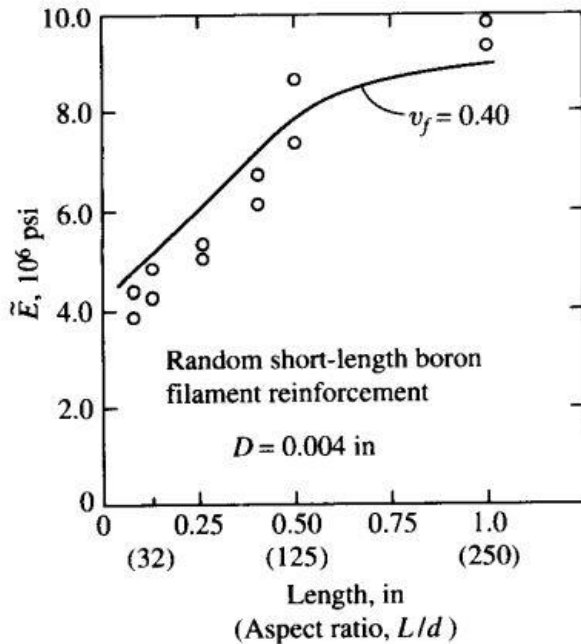


Figure 11: Young's modulus comparison predictions [14]

### 2.2.2 Composite Strength

Approximating strength of a composite is a much more difficult process than moduli. The methods depend on whether the reinforcement or the matrix has a lower maximum strain. Composite failure is defined by either fiber failure or matrix failure. This is under the assumption that the interface has infinite strength and does not slip. Due to the perfect bonding of the matrix and reinforcement, the average displacements and strains in the reinforcement, matrix, and composite along the longitudinal direction are the same,  $\bar{\varepsilon}_{c1} = \bar{\varepsilon}_{f1} = \bar{\varepsilon}_{m1}$ . The fiber failure strain,  $e_{f1}^{(+)}$ , and matrix failure strain,  $e_m^{(+)}$ , can be defined by:

$$e_{f1}^{(+)} = \frac{s_{f1}^{(+)}}{E_{f1}} \quad 2.8$$

$$e_m^{(+)} = \frac{s_m^{(+)}}{E_m} \quad 2.9$$

where  $s_{f1}^{(+)}$  is the longitudinal strength of the fiber in tension and  $s_m^{(+)}$  is the strength of the matrix in tension. There are two cases of longitudinal failure:

Case 1:

- $e_m^{(+)}$  is larger than  $e_{f1}^{(+)}$  and it can be concluded that the fiber will govern failure

Case 2:

- $e_{f1}^{(+)}$  is larger than  $e_m^{(+)}$  and it can be concluded that the matrix will govern failure.

Most fibers used in engineering have a longitudinal failure strain that is less than that of the matrix [14]. When the fiber governs failure, case 1, the stress in the fiber reaches the fiber tensile strength and the matrix stress is defined by:

$$s_{mf1}^{(+)} = E_m e_{f1}^{(+)} \quad 2.10$$

When the stress in the matrix reaches the matrix tensile strength,  $s_{mf1}^{(+)}$ , the composite stress reaches the composite strength,  $s_L^{(+)}$ :

$$s_L^{(+)} = s_{f1}^{(+)}v_f + s_{mf1}^{(+)}(1 - v_f) \quad 2.11$$

The empirical relation for the composite longitudinal tensile strength is extrapolated to multiple reinforcements and is given as:

$$s_L^{(+)} = s_{f1}^{(+)}v_f + s_{g1}^{(+)}v_g + \frac{1}{2}(s_{mf1}^{(+)}v_m + s_{mg1}^{(+)}v_m) \quad 2.12$$

where

$$s_{g1}^{(+)} = E_{g1}e_{g1}^{(+)} \quad 2.13$$

$$s_{mg1}^{(+)} = E_m e_{g1}^{(+)} \quad 2.14$$

When the matrix governs failure, case 2, the stress in the matrix reaches the matrix tensile strength and the fiber stress is defined by:

$$s_{fm1}^{(+)} = E_{f1}e_m^{(+)} \quad 2.15$$

When the stress in the fiber reaches the fiber tensile strength,  $s_{fm1}^{(+)}$ , the composite stress reaches the composite strength,  $s_L^{(+)}$ :

$$s_L^{(+)} = s_{fm1}^{(+)}v_f + s_m^{(+)}(1 - v_f) \quad 2.16$$

The empirical relation for the composite longitudinal tensile strength is extrapolated to multiple reinforcements and is given as:

$$s_L^{(+)} = s_{fm1}^{(+)}v_f + s_{gm1}^{(+)}v_g + s_m^{(+)}(1 - v_t) \quad 2.17$$

where

$$s_{gm1}^{(+)} = E_{g1}e_m^{(+)} \quad 2.18$$

$$v_t = v_f + v_g \quad 2.19$$

Transverse failure strain is due to the strain concentration around the matrix. A strain concentration factor,  $F$ , is used because of the non-linearity of stress-strain relationships in transverse loading [14]. The transverse strength is given as:

$$s_T^{(+)} = \frac{E_2 s_m^{(+)}}{E_m F} \quad 2.20$$

where

$$F = \sum_{i=1}^n F_i v_i$$

$$F_i = \frac{1}{\frac{d_i}{s_i} \left[ \frac{E_m}{E_{i2}} - 1 \right] + 1} \quad 2.21$$

The random packing of the fibers can be quantified by the Voronoi cell shown in Figure 12. Stresses, strains, displacements and dimensions are assumed constant inside the Voronoi cell. The cell size and fiber diameter are denoted by  $s$  and  $d$ , respectively. The subscript  $i$  shows

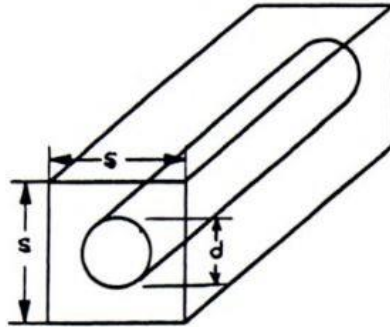


Figure 12: Voronoi cell approximation [14]

that the stress concentration factor can be extrapolated to multiple reinforcements. Since the fiber-packing geometry is never 100% reproducible, the micromechanics predictions will never be exact [14]. The fiber diameter,  $d$ , does not need to be approximated by a circle, but for this paper only circle approximations are discussed. The cell size,  $s$ , is given as:

$$s_i = d_i \sqrt{\frac{\pi}{4v_i}} \quad 2.22$$

The cell size equation is under the assumption that the fiber volume fraction is approximated as a square array as shown in Figure 12.

An in-plane shear strength,  $s_{LT}$ , must be defined in order to continue analysis on the discontinuous fiber composite. This expression follows the same form as 2.20 and is given as:

$$s_{LT} = \frac{G_{12}s_m^{(+)}}{G_m F_s} \quad 2.23$$

where

$$F_s = \sum_{i=1}^n F_{si} v_i \quad 2.24$$

$$F_{si} = \frac{1}{\frac{d_i}{s_i} \left[ \frac{G_{m12}}{G_{i12}} - 1 \right] + 1} \quad 2.25$$

The in-plane shear concentration factor,  $F_s$ , is again due to the non-linearity between the stress-strain relationships in the transverse loading. The concentration factors  $F$  and  $F_s$  both assume that stresses in the matrix and fibers are equal and that each material satisfies Hooke's law [14].

The behavior of the generally orthotropic aligned discontinuous reinforced composite can be analyzed using a representative volume element as shown below in Figure 13, where the reinforcement is oriented at an angle with the loading axis. Calculation of the off axis strength of a randomly oriented composite is accomplished with the Tsia-Hill Criterion.

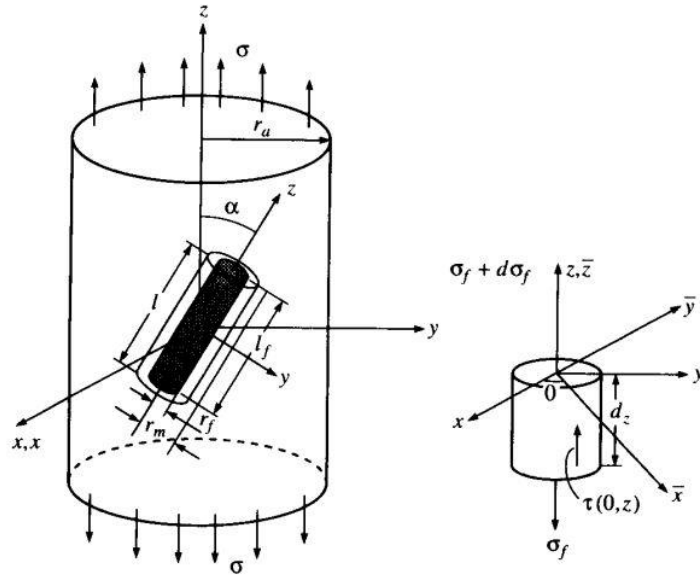


**Figure 13: Representative volume element [14]**

The Tsia-Hill Criterion is a surface for plane stress and is a function of the biaxial stresses and shear stresses. The Tsia-Hill Criterion was developed as a modification to the maximum distortional energy criteria known as the von Mises Criterion. The Tsia-Hill Criterion is compared to the Maximum Stress and Maximum Strain Criterion in Figure 14.

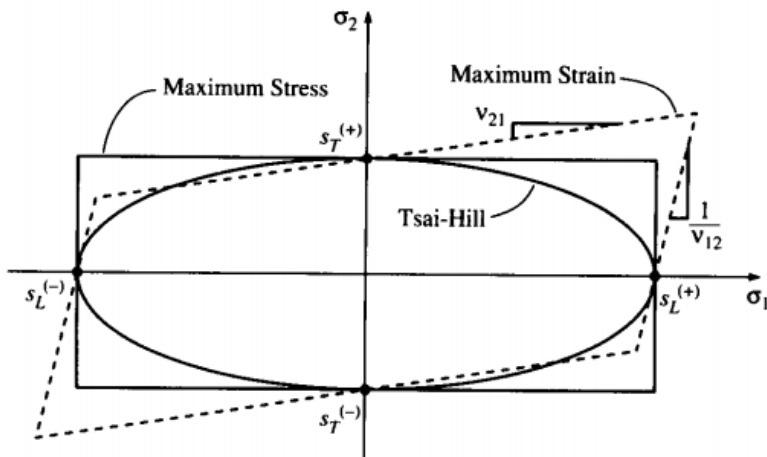


**Figure 14: Tsia-Hill, maximum stress, and maximum strain criterions [14]**

The Maximum Stress Criterion does not incorporate the interaction between stress components and creates a rectangular shape. This criterion predicts failure when any principal material axis stress exceeds the corresponding strength. The Maximum Strain Criterion

incorporates added strain in biaxial loading creating a parallelogram. This criterion predicts failure when any principal material axis strain exceeds the corresponding ultimate strain. The Tsia-Hill Criterion is a continuous failure surface and takes the shape of ellipse. Experimental data tends to follow the Tsia-Hill Criterion more than the Maximum Stress or Maximum Strain Criterion [14]. With the Tsai-Hill Criterion, loading can be either positive or negative because the criterion is not direction specific.

Using the definitions of the composites longitudinal strength,  $s_L^{(+)}$ , transverse strength,  $s_T^{(+)}$ , and in plane shear strength,  $s_{LT}$ , then substituting the corresponding off axis stress state into the Tsia-Hill Criterion, the off axis stress becomes [14]:

$$\sigma_x = \left[ \frac{\cos^4 \theta}{s_L^2} + \left( \frac{1}{s_{LT}^2} - \frac{1}{s_L^2} \right) \sin^2 \theta \cos^2 \theta + \frac{\sin^4 \theta}{s_T^2} \right] \quad 2.26$$

Baxter developed a model for predicting the geometrically averaged strength,  $\tilde{\sigma}_x$ , for randomly oriented composites by averaging the Tsai-Hill equation for off-axis strength [14] as

$$\tilde{\sigma}_x = \frac{\pi \int_0^{\pi/2} \sigma_x d\theta}{\frac{\pi}{2}} \quad 2.27$$

Using equation 2.27, Lees and broke the failure criterion into three mechanisms. Each operate over a range of angles:

- for  $0 \leq \theta \leq \theta_1$   $\sigma_x = \frac{s_L^{(+)}}{\cos^2 \theta}$  Longitudinal tensile failure
  - for  $\theta_1 \leq \theta \leq \theta_2$   $\sigma_x = \frac{s_{LT}}{\sin \theta \cos \theta}$  Interfacial shear failure
  - for  $\theta_2 \leq \theta \leq \frac{\pi}{2}$   $\sigma_x = \frac{s_T^{(+)}}{\sin^2 \theta}$  Transverse tensile failure
- $$\cot \theta_1 = \frac{s_T^{(+)}}{s_{LT}}$$
- $$\tan \theta_2 = \frac{s_T^{(+)}}{s_{LT}}$$

Using the representative volume element, Figure 13, Lees integrated equation 2.27 over all possible orientations using the angle bounds. Lees established a geometrically averaged

strength,  $\tilde{\sigma}_x$ , for randomly oriented discontinuous reinforcements excluding fiber orientation,  $\theta$  [26]:

$$\tilde{\sigma}_x \simeq \frac{2s_{LT}}{\pi} \left[ 1 + \frac{s_T^{(+)}}{s_{mf1}} + \ln \frac{s_T^{(+)} s_{mf1}}{s_{LT}^2} \right] \quad 2.28$$

Chen also took the same approach as Lees, but accounted for a strength efficiency factor  $\Psi$  and obtained the equation [27]:

$$\tilde{\sigma}_x = \frac{2s_{LT}}{\pi} \left[ 2 + \ln \frac{\Psi s_L^{(+)} s_T^{(+)}}{s_{LT}^2} \right] \quad 2.29$$

Lees and Chen both reported good agreements of their predictions from and to experimental data [14]. Neither Lees nor Chen incorporated the use of equations involving effects of fiber length on composite longitudinal tensile strength,  $s_L^{(+)}$  [14] [22]. This is considerable when expanding these equations to multiple reinforcements with different geometry. Equations 2.28 and 2.29 were developed using only fiber orientation and not fiber length. The equations developed by Lees and Chen are independent of reinforcement span [26] [27]. However, equations 2.28 and 2.29 are significantly influenced by the shear strength,  $s_{LT}$ , because the matrix supports much of the load [14].

The randomly oriented composite mechanics discussed in this chapter are used to predict material characteristics of an unknown mixture. The mixture will consist of chopped fibers, iron particles, and matrix material. The analytical composite results are compared with uniaxial test specimen experimental results in the next chapter.

### 3 Uniaxial Tension Testing of Composites

Tensile tests are performed to measure properties of materials. These properties are then used to predict the behavior of a material under different loading other than uniaxial tension. Uniaxial tension testing is an experiment where a specimen is subjected to a controlled load. The load is applied by a test machine, resulting in a gradual elongation and eventual fracture of the specimen.

This chapter discusses tensile testing techniques to verify discontinuous-randomly oriented isotropic mechanical properties. Specimen design, mold design, molding process, measurements and testing are discussed. Poisson's ratio, elastic modulus, and tensile strength are determined from uniaxial tension tests. Different fiber, iron and matrix volume fractions are tested to collect various trial points. Test results are compared to the equations discussed in chapter 2 for accuracy.

#### 3.1 Composite Specimen Design

Tensile test specimens come in many different shapes and sizes. The typical tensile specimen has a shape referred to as a 'dogbone' and is illustrated in Figure 15. The typical tensile specimen has enlarged ends or shoulders for the machine to grip onto. Shoulders can be manufactured in various ways to mate the specimen to the tensile testing machine. An important part of the specimen is called the reduced section. The cross sectional area of the reduced section is much smaller than that of the shoulders as shown in Figure 15. A smaller reduced section ensures that deformation and failure is localized in this region. The distance between the ends of the reduced section must be long enough that the larger ends do not constrain deformation. The reduction from the grip section to the reduced section should be smooth. A larger radius shields the specimen from unwanted stress concentrations that could skew results. FEA aids in designing the tensile specimen so the radius does not interfere with the gage length stress. The gage length is prismatic and undamaged. Measurements are made over the gage length section, ergo instruments such as strain gages or extensometers are placed here. The gage length section should be great, relative to the diameter or thickness of the specimen. Otherwise, the stress state will be more complex than simple tension [28].

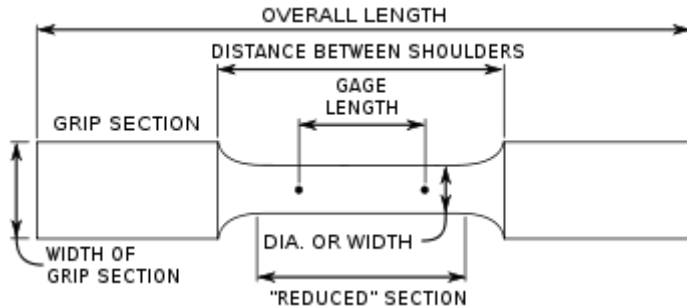


**Figure 15: Dogbone style specimen**

There are many different ways to secure the specimen in the testing machine. A few are shown below in Figure 16. The specimen that is being constructed and the testing machine being used must be taken into account when selecting a gripping mechanism. The most important thing is to ensure that the grip section can be held at the maximum load.

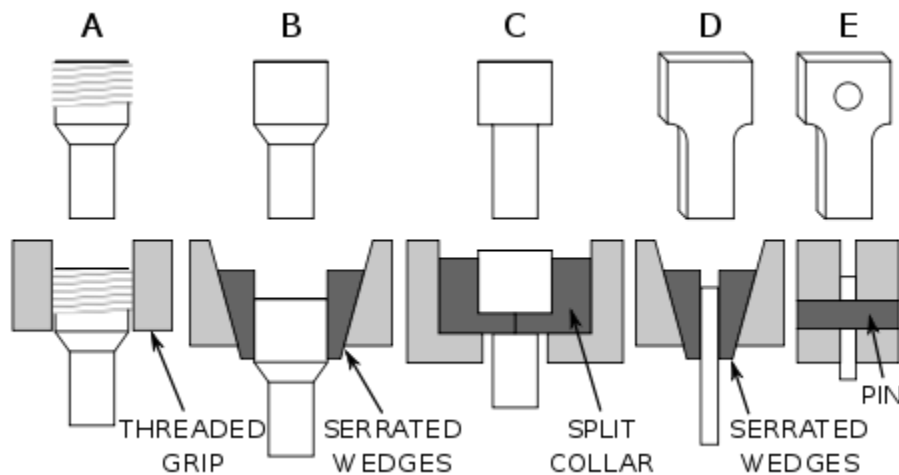


**Figure 16: Gripping systems for tensile specimens**

For the composite tensile test, a specimen with a pin design is chosen replicating Figure 16-E. To complete the test, the specimen must be able to interact with the pull testing machine. The machine being used requires threaded grips, but the composite being tested does not have the ability to possess threads. Having threads on the composite neglects the assumption that the fiber length must be shorter than the thickness or pitch of the threads. The strength in the threads would not be the same strength as the rest of the composite [14]. The threads would possess too high of a stress concentration and unwantedly break at the threads during the test.

An attachment is made to connect the threaded grips to the pin connection of the composite. A drafted SolidWorks component and completely machined attachment is shown in Figure 17.

Two attachments are made because the machine requires one attachment for the stationary arm and one for the moving arm.

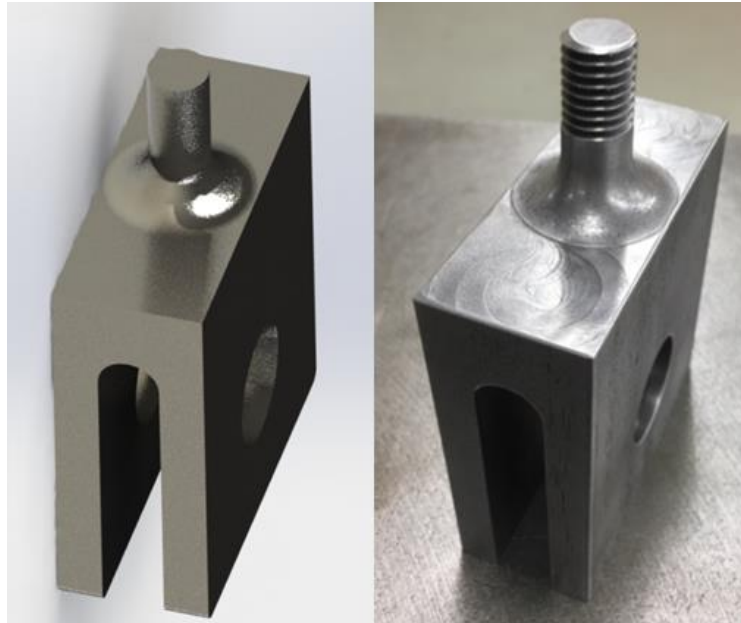


**Figure 17: Machine attachment for composite specimen**

The composite specimen needs to be thick enough to assume that the reinforcements are randomly distributed in all three directions,  $x$ ,  $y$ , and  $z$ . Geometric averaging techniques can be used when the reinforcement length is much less than the thickness of the part [14]. The fiber length chosen for this experiment are  $\frac{1}{4}$  inch fibers and the iron particle size chosen is 325 mesh or 44 microns. To ensure that the fibers are randomly oriented, a thickness of  $\frac{1}{2}$  inch has been chosen for the square ‘dogbone’ shape. The edges are also filleted to minimize the absence of reinforcements in the small corners.

It is essential that the composite specimens elongate and fracture across the gage length. Simulations are used to provide knowledge of where the specimen begins to yield by quantifying stress concentrations. The contour from the shoulder to the reduced section can be adjusted in the simulation to confirm the gage length’s fracture. The final specimen design is shown in Figure 18 along with a SolidWorks static strength simulation. The simulation also

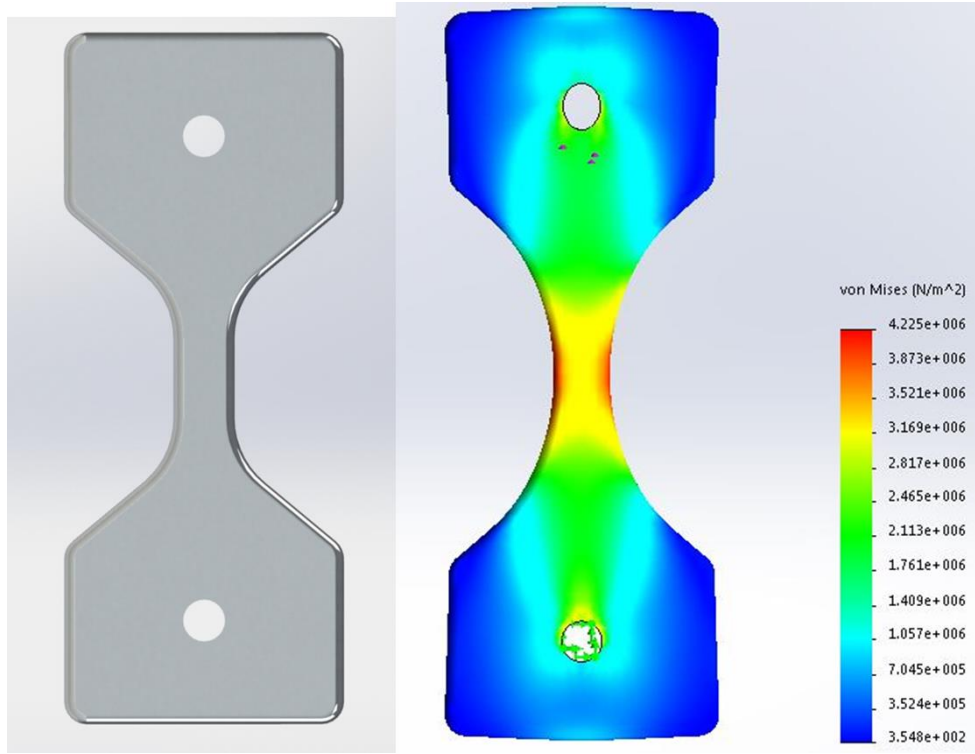


**Figure 18: Final specimen geometry and SolidWorks static simulation**

provides knowledge on how large of a pin to use for the specimen. The composite relies on the hole to be small because of the lower bearing strength of the material. The machine wants the pin to be large so it can focus the force on the gage length and not the pin. The pin size can be calculated at first, but then confirmed with the static stress simulation. After reviewing simulations, a pin size of  $\frac{1}{2}$  inch is chosen for the final specimen.

Because of the extensive molding process, fit of the specimen and attachments into the tension test machine is necessary to check before all of specimens are completed. A prototype is 3D printed of the specimen to ensure the fit of the components. The combined attachments, hardware, and 3D printed prototype are shown in Figure 19. The final dimensions of the uniaxial test specimen are shown in Appendix A: Mechanical Testing Information.

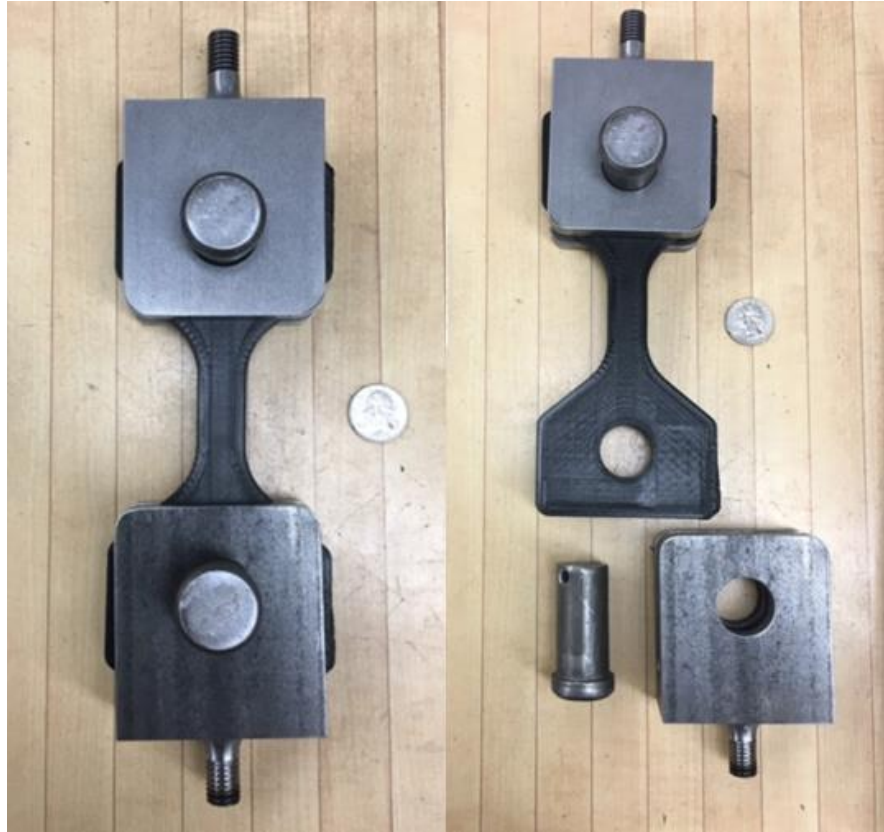


Figure 19: Machine attachments, 3D printed specimen, and hardware

### 3.2 Composite Mold Design

Molding is the process of manufacturing a certain shape with a pliable materiel using a ridged frame. A mold is a shaped block that mimics the structure and size of the desired component. When constructing a composite part, reinforcement and matrix materials are combined and cured around or inside a mold. After curing, the part shape is set.

Male and female molds are two fundamental types of forms. A male mold is a form that mimics the final shape of the part, but the part is fabricated over its outer surface. Male molds are not good for high tolerance parts because the part will be larger than the original frame. Female or cavity molds are generally more costly, but they offer more advantages. Female molds house the molding materials which enables high tolerance components. Female molds also offer smoother finishes than male molds. The need for high tolerances for this composite test will require the use of a female type mold.

Composite molding processes can be broken into two main types: thermoplastic and thermoset. Thermoplastics are melt process materials. When enough heat is added, the material liquefies and softens enough to be molded. When heat is removed, the material solidifies. Thermoset materials undergo a chemical reaction and transforms from a liquid to a solid. In its uncured form the material has unlinked molecules, but the addition of a second material, or catalyst, will initiate the chemical reaction. With the help of the catalyst the molecules link and form molecular chains causing the material to solidify. This change is permanent and irreversible. The total cure time of the thermoset can vary by type. The exposure to high heat will cause the material to degrade, not melt [29]. The matrix material used in this molding process is a thermoset that requires a two part epoxy to enable the chemical change.

After the matrix cures in the mold, manufacturer recommendations are to post-cure the part within the mold in an oven for 8 hours. This speeds up the total cure time of the thermoset from 3 weeks to 1 day. The oven curing limits the material that can be used to construct the mold. Machinability and cost are also taken into account for materials used for the mold. The finish on the mold should be smooth and free of blemishes because the specimen will reflect the mold. Blemishes, or voids, will skew collected results. The material that is able to withstand the heat, provide the best finish, and is most cost effective, is aluminum.

Multiple molds are constructed at different volume fractions of composite, iron and matrix material. The molding process itself takes 45 minutes, but the matrix material requires 1 day to fully cure. The part cannot be separated from the mold for the entire cure time. To fabricate more than one mold per day, 3 total molds are constructed to reduce total specimen manufacturing time.

The shape, mold material and mold type have been determined, but other features the mold requires are outlined in Figure 20.

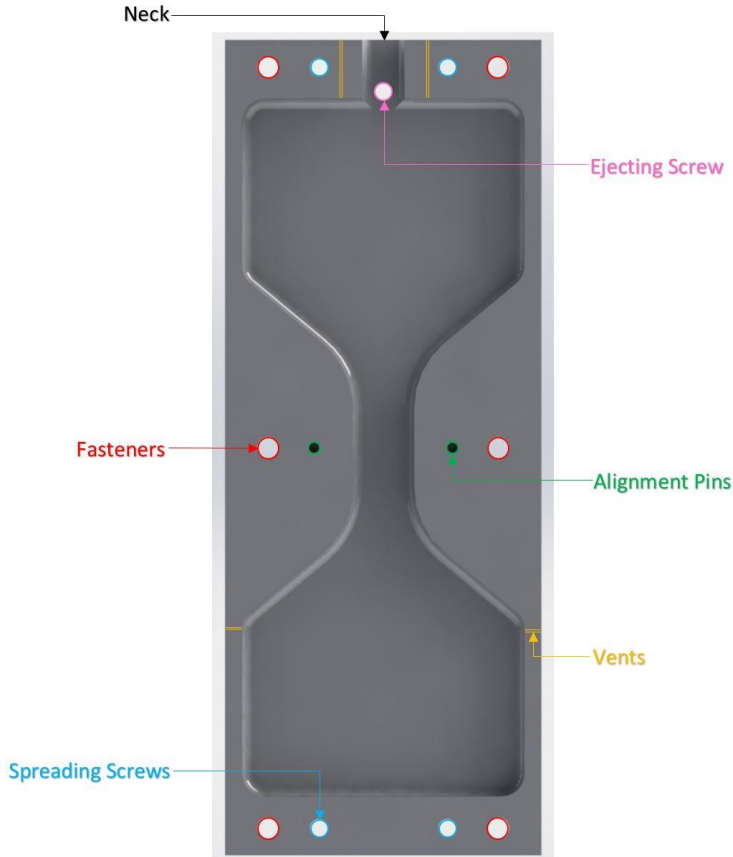


Figure 20: Mold diagram

- Fasteners – hold the mold halves together for the duration of construction
- Alignment pins – repeatedly align the two halves of the mold together for a visibly seamless interception
- Ejecting screw – push the part out of the mold upon cure completion
- Spreading screws – Spreads the two mold halves apart
- Neck – entrance for the composite and where pressure will be applied
- Vents – allow air voids to escape and composite mixture to completely fill the mold
- Number Stamp – identifies which mold to audit volume fraction iteration

The inside halves of the mold are shown below in Figure 21. The mold was machined as one piece to increase precision and then cut into six separate sections to produce the three separate molds shown in Figure 22.

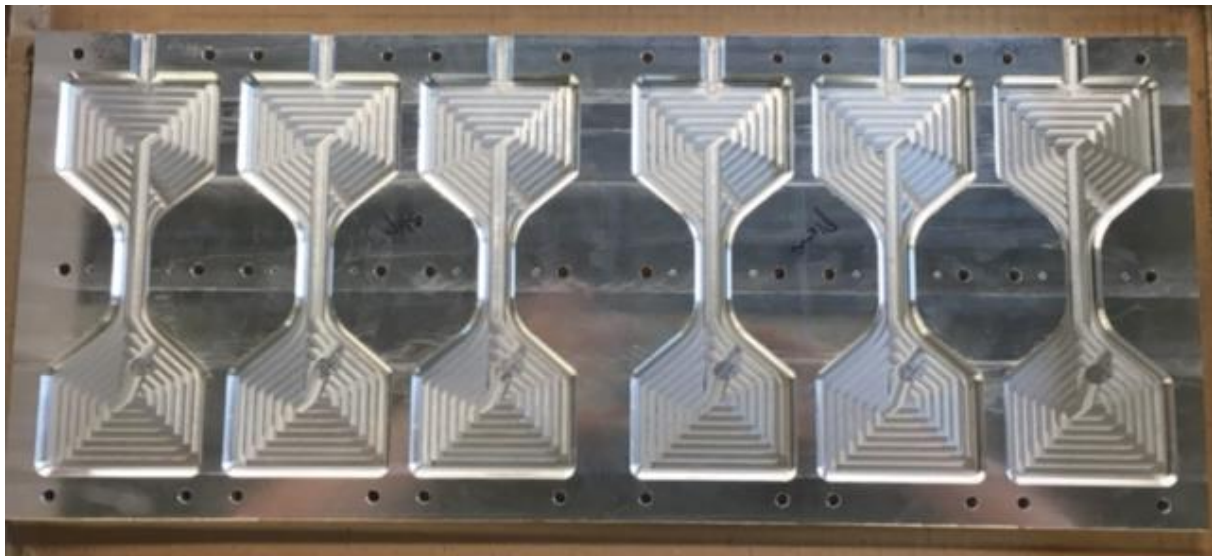


Figure 21: Inside machined molds



Figure 22: Completed molds

### 3.3 Composite Molding Methodology

Mechanical test specimens include combinations of chopped fiber reinforcements, iron particles, and matrix material. The hybrid composite mixture is uniformly mixed together, inserted into the mold, and then cured.

Before the mechanical composite specimens are manufactured, the volume fractions of each need to be determined. The volume fraction is defined as the volume of a material,  $V_i$ , divided by the volume of all of the materials summed together. The volume fraction for a single material is given as:

$$\phi_i = \frac{V_i}{\sum_{j=1}^n V_j} \quad 3.1$$

The sum of all of the volume fractions of a mixture is equal to one. A mass fraction can be calculated for each material as well, but the composite mechanics discussed in chapter 2 require volume fraction calculations.

To generate specimens, the percentages of volume fractions need to be chosen. One method of generating volume fractions is random sampling. Randomly sampling points does not take into account the point that was chosen on the previous iteration. Selecting points at random does run the risk of test points clustering in certain regions. Clustering is more likely when the design space is large compared to the number of test points desired. This results in poor distribution of the design space. For this experiment a low number of test points is desired because of the cost of producing specimens. The use of Latin hypercube sampling can amend the situation.

Latin Hypercube sampling is a method for generating random sample test points to explore the entire parameter space with a minimum number of test points. To select points, the parameter space is evenly gridded into bins. The number of bins matches the number of design points that the creator has control over. Then the gridded space can be filled by randomly selecting permutations of the variables which represent the grid locations. For a 2D design space, no other data points can be selected in the column or row occupied by that point. The configuration is similar to having a rook in every column and row on a chess board, but none are threatening each other [30]. An example of Latin hypercube sampling in a 2D design space is illustrated in Figure 23.

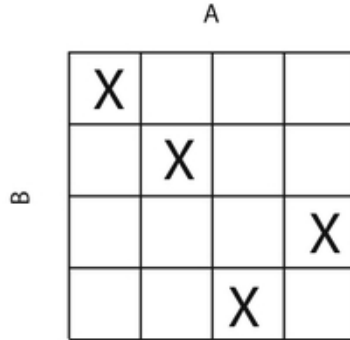


**Figure 23: Latin hypercube sampling example, 2D**

To select volume fractions for the test specimens, Latin hypercube sampling is used. To initiate sampling, volume fraction bounds must be determined for each material. The limits cannot be up to 100% of a single material because the substance is no longer a composite. The material must also possess enough matrix to fully bond the materials together. The point where the material starts to lose strength is the upper bound for the volume fraction. The fit presented by Chen, equation 2.29, is extrapolated out to show the effect of the strength of the material vs. volume fraction of the reinforcement. For this study only a single reinforcement material is used. The strength of the composite is compared against volume fraction for a chopped carbon fiber composite, Figure 24, and an iron particle composite, Figure 25.

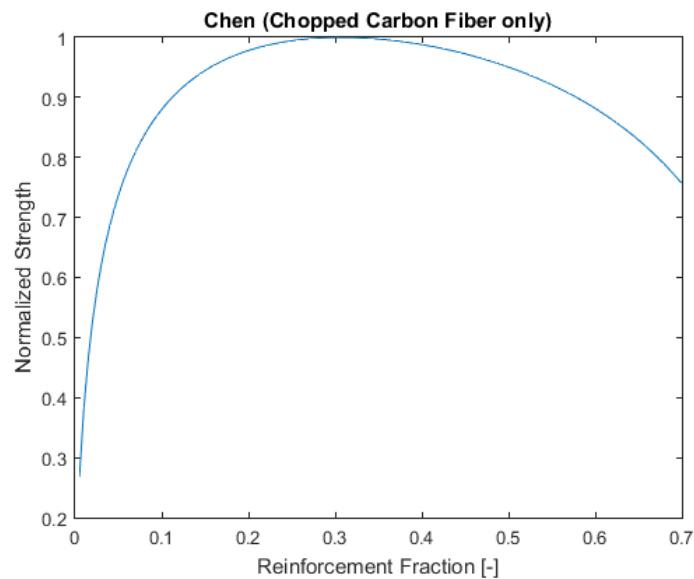


**Figure 24: Chen, equation 2.29, effect chopped fiber volume fraction on normalized strength**

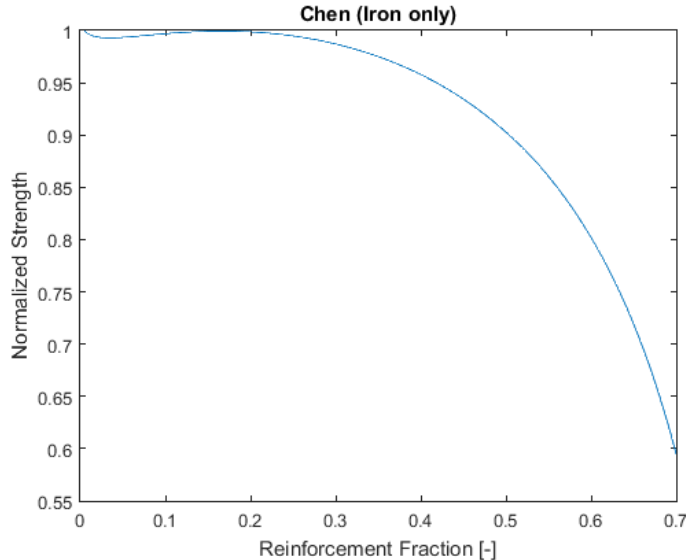


**Figure 25: Chen, equation 2.29, effect iron particle volume fraction on normalized strength**

Figure 24 shows that the strength of chopped fiber composites starts to drop off at a volume fraction of 0.3. The iron composite strength, Figure 25, starts to also decline at a volume fraction of around 0.3. The total volume fraction of the reinforcement in the composite will be the chopped fiber and iron particles combined. This experiment will set an upper limit for the combined reinforcement's volume fraction of 0.3.

Latin hypercube sampling points are shown below in Table 1. The volume fractions of each material are shown in percent along with the mixture ratios of mass or volume needed to create each specimen. The density of each material is taken into account to obtain the mass fraction for both the chopped fibers (CF) and iron particles. Because of their solid state, these two materials are only accurately measured on a mass fraction basis using a digital scale. The thermoset matrix comes in liquid form and has two parts: a hardener and a catalyst. The volumetric ratio of the hardener to the catalyst recommended by the manufacturer is 1:1. The matrix is easier to measure in a beaker as a volume fraction rather than a mass fraction because of its pre-cured liquid state. Data sheets for each material are presented in Appendix A: Mechanical Testing

**Table 1: Specimen volume fractions and mixture ratios**

#	CF (%)	Iron (%)	Matrix (%)	CF (g)	Iron (g)	Matrix (mL)
1	8.0	0.0	92.0	28.7	0.0	180.9
2	12.0	3.5	84.5	43.1	54.1	166.1
3	10.0	7.0	83.0	35.9	108.2	163.2
4	20.0	5.0	75.0	71.8	77.2	147.5
5	15.0	11.0	74.0	53.8	170.0	145.5
6	5.0	17.0	78.0	17.9	262.8	153.4
7	20.0	10.0	70.0	71.8	154.5	137.6
8	30.0	0.0	70.0	107.7	0.0	137.6
9	0.0	0.0	100.0	0.0	0.0	196.6

Once a specimen has been post-cured and removed from the mold, the specimen is marked with the number it has been assigned to from Table 1. Various specimens after post-curing are shown in Figure 26.

**Figure 26: Specimens after curing**

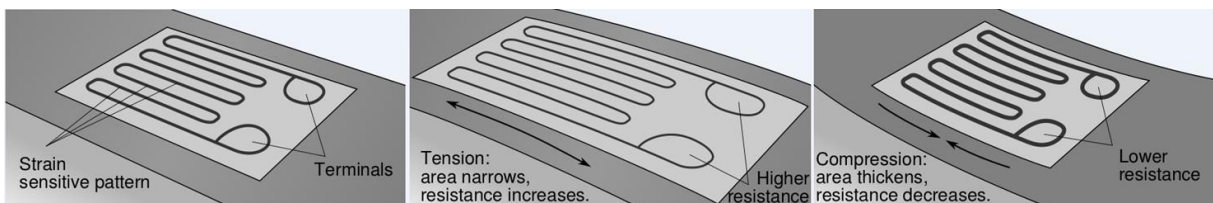
Each specimen is weighed as soon it has exited the mold. The mass is recorded with a digital scale and is compared to the theoretical mass to find the air percentage in the specimen. The percentage of air will be used as a parameter in the composite mechanics discussed in chapter 2. Each volume fraction from Table 1 is manufactured twice for consistency. The mass results are compiled in ascending order below in Table 2.

**Table 2: Mass results of specimens**

#	Theoretical mass (g)	Actual mass (g) of specimen 1	Actual mass (g) of specimen 2	Air (%) in specimen 1	Air (%) in specimen 2
1	196.9	192.6	187.3	2.23	4.92
2	241.8	239.9	237.6	0.80	1.75
3	279.3	270.8	273.6	3.07	2.07
4	268.7	267.5	264.1	0.45	1.71
5	331.1	316.6	327.1	4.39	1.22
6	387.5	371.2	380.3	4.21	1.86
7	325.8	311.9	314.6	4.27	3.44
8	223.7	221.1	217.4	1.19	2.84
9	187.2	184.1	186.3	1.68	0.51

### 3.4 Strain Gage Measurements

Strain gages are devices used to measure surface extension or contraction of a component. They cannot be used to measure the strain at an interior point of a member. Electric strain gages are used to obtain an average extension over a given gage length. The gages are made of fine wire and are glued to the surface of the component. When a force is applied to the member, the gage elongates or contracts. The change in voltage due to the change in resistance in the wire can be measured as illustrated in Figure 27.

**Figure 27: Strain gage resistance**

A wire strain gage can only effectively measure strain in one direction. Three strain measurements, in three linearly independent directions at a point on the surface of a specimen are required to determine the average state of stress at that point. The three strain gages are often clustered and referred to as a strain rosette. Two common forms of strain rosettes are the rectangular rosette and delta rosette. The rectangular rosette has angles between the three strain gages of  $45^\circ$  and the delta rosette has angles of  $60^\circ$ . The two types are respectively

shown below in Figure 28 [31]. Using a uniaxial tension test and stacked rosette data, the assumed isotropic composite is fully defined with the two linear elastic constants Poisson's ratio and Young's modulus.

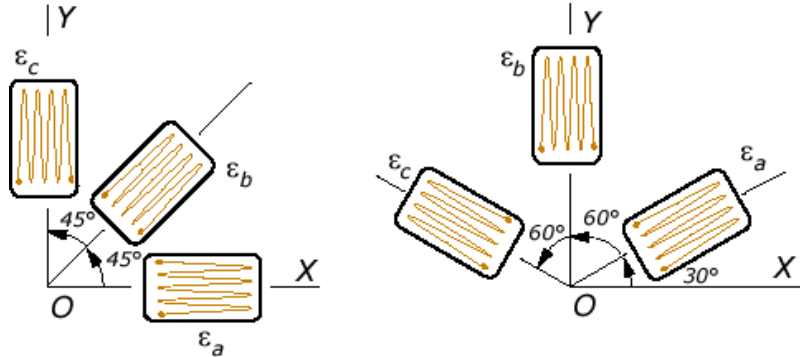


**Figure 28: Rectangular rosette and delta rosette**

The stacked rosette strain gages selected for this experiment have an angle,  $\theta$ , of  $45^\circ$ . Strain gages are mounted in the center of the gage section on each specimen as shown in Figure 29. The strain gage data sheet and a installation guide are presented in Appendix B: Specimen Data Collection Procedure



**Figure 29: Installed stacked rosette strain gage**

### 3.4.1 Poisson's Ratio

The strain gage rosette is used to approximate Poisson's ratio for the hybrid composite. The composite is assumed isotropic and when the material is placed under tension there exists a

longitudinal strain,  $\varepsilon_l$ , and a transverse strain,  $\varepsilon_t$ . Poisson demonstrated that these two strains were proportional to each other within the range of Hooke's law. Poisson's ratio is an elastic constant given as [32]:

$$\nu = -\frac{\varepsilon_t}{\varepsilon_l} = \frac{|\varepsilon_2|}{|\varepsilon_1|} \quad \varepsilon_2 < \varepsilon_1 \quad 3.2$$

The Poisson's ratio of a stable, isotropic, linear elastic material will be between -1 and 0.5. This is due to the requirement that the Young's modulus, shear modulus and bulk modulus must have positive values. Most materials have Poisson's ratios between 0 and 0.5 [32]. To determine principal strains  $\varepsilon_1$  and  $\varepsilon_2$ , the stacked rosette strain measurements will be used.

Through any point in an undeformed component, there exist three perpendicular lines that remain perpendicular under deformation. The strains of these three lines are called principal strains at the point. The theory is analogous with stress. To determine the principal strains in a three-dimensional case, the law of direction cosines is used in conjunction with the strain matrix,  $\tilde{\epsilon}$ , to obtain [31]:

$$\tilde{\epsilon} = \begin{bmatrix} \epsilon_{xx} & \epsilon_{xy} & \epsilon_{xz} \\ \epsilon_{xy} & \epsilon_{yy} & \epsilon_{yz} \\ \epsilon_{xz} & \epsilon_{yz} & \epsilon_{zz} \end{bmatrix}$$

$$\det(\tilde{\epsilon} - MI_n) = 0 \quad 3.3$$

or expanding the determinate yields

$$M^3 - \bar{I}_1 M^2 + \bar{I}_2 M + \bar{I}_3 = 0$$

where

$$\begin{aligned} \bar{I}_1 &= \text{tr}(\tilde{\epsilon}) \\ \bar{I}_2 &= \left| \begin{matrix} \epsilon_{xx} & \epsilon_{xy} \\ \epsilon_{xy} & \epsilon_{yy} \end{matrix} \right| + \left| \begin{matrix} \epsilon_{yy} & \epsilon_{yz} \\ \epsilon_{yz} & \epsilon_{zz} \end{matrix} \right| + \left| \begin{matrix} \epsilon_{xx} & \epsilon_{xz} \\ \epsilon_{xz} & \epsilon_{zz} \end{matrix} \right| \quad 3.4 \\ \bar{I}_3 &= \det(\tilde{\epsilon}) \end{aligned}$$

The roots of  $M$  are always real and positive because of the symmetry of the strain matrix,  $\tilde{\epsilon}$ . The identity matrix,  $I_n$ , is the same size as the strain matrix. The roots to the characteristic

equation are the principal strains,  $\epsilon_1$ ,  $\epsilon_2$ , and  $\epsilon_3$ . The strain invariants,  $\bar{I}_1$ ,  $\bar{I}_2$ , and  $\bar{I}_3$ , cannot be influenced by choice of coordinate axes [31].

The strain rosette is bonded to the free surface of the specimen so  $\epsilon_{zz} = \epsilon_{xz} = \epsilon_{yz} = 0$  [31]. The principal strains are [31]:

$$\epsilon_1, \epsilon_2 = \frac{\epsilon_{xx} + \epsilon_{yy}}{2} \pm \sqrt{\frac{1}{4}(\epsilon_{xx} - \epsilon_{yy})^2 + \epsilon_{xy}^2} \quad 3.5$$

To find  $\epsilon_{xx}$ ,  $\epsilon_{yy}$  and,  $\epsilon_{xy}$  the stacked rosette strain gage can be used. The strain rosette is mounted on the  $x$ -  $y$  plane as shown in Figure 30.

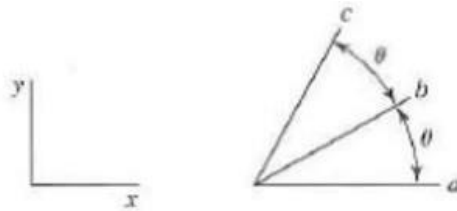


Figure 30: Stacked rosettes [31]

Deriving equations determining  $\epsilon_{xx}$ ,  $\epsilon_{yy}$  and,  $\epsilon_{xy}$  in terms of  $\epsilon_a$ ,  $\epsilon_b$ ,  $\epsilon_c$ , and  $\theta$  requires the use of direction cosines. The extensional strains in the directions of  $a$ ,  $b$  and  $c$  are [31]:

$$\begin{aligned} \epsilon_a &= \epsilon_{xx} \\ \epsilon_b &= \epsilon_{xx} (\cos^2 \theta) + \epsilon_{yy} (\sin^2 \theta) + 2\epsilon_{xy} (\cos \theta) (\sin \theta) \end{aligned} \quad 3.6$$

and

$$\epsilon_c = \epsilon_{xx} (\cos^2 2\theta) + \epsilon_{yy} (\sin^2 2\theta) + 2\epsilon_{xy} (\cos 2\theta) (\sin 2\theta)$$

The stacked rosette strain gages being used in this experiment have an angle,  $\theta$ , of  $45^\circ$ .

Solving the above equations for  $\epsilon_{xx}$ ,  $\epsilon_{yy}$  and,  $\epsilon_{xy}$ , and then using  $\theta=45^\circ$  yields:

$$\begin{aligned} \epsilon_{xx} &= \epsilon_a \\ \epsilon_{yy} &= \epsilon_c \\ \epsilon_{xy} &= \epsilon_b - \frac{1}{2}(\epsilon_a - \epsilon_c) \end{aligned} \quad 3.7$$

Using the results from equation 3.7 and 3.5 solves for the principal stresses,  $\varepsilon_1$  and  $\varepsilon_2$ , directly from the stacked rosette gage measurements  $\varepsilon_a$ ,  $\varepsilon_b$ , and  $\varepsilon_c$ :

$$\varepsilon_1, \varepsilon_2 = \frac{\varepsilon_a + \varepsilon_c}{2} \pm \sqrt{\frac{(\varepsilon_a - \varepsilon_b)^2 + (\varepsilon_b - \varepsilon_c)^2}{2}} \quad 3.8$$

Using equation 3.8 and 3.2 Poisson's ratio can be determined for the composite material. This method is independent of Young's modulus which is unknown for the composite before testing.

### 3.4.2 Young's Modulus

Young's modulus, or the elastic modulus, is the measure of stiffness of a solid material. Approximating Young's modulus is more straightforward than Poisson's ratio. With a surface mounted strain gage, the uniaxial tension test gives strain data as a change in electrical resistance. One of the axis of the strain gage is aligned with the direction that the machine applies force. The uniaxial tension test machine outputs the force that it is being applied to the material. Stress can be calculated across the gage length with the known cross sectional area of the specimen. Plotting the stress vs strain, Figure 31, will give an approximation of the elastic modulus,  $E$ , in the linear elastic region. The principal stress-strain relationship in this region is given by Hooke's law in a uniaxial state of stress [32]:

$$\begin{aligned} \sigma_1 &= E\varepsilon_1 \\ \sigma_2 &= 0 \\ \sigma_3 &= 0 \end{aligned} \quad 3.9$$

The ultimate tensile strength is also recorded during the uniaxial tension test. The ultimate tensile strength is defined as the maximum stress attained in the engineering stress-strain diagram. The tensile test machine applies an increasing force to the material at a constant strain rate until stress failure,  $\sigma_f$ . The strain rate is slow enough that dynamic effects are neglected. The strain rate for this tensile tests is  $0.001\frac{1}{s}$ . For a ductile material the engineering failure stress is lower than the ultimate tensile strength because of the definition of engineering stress. For a brittle material the ultimate tensile strength and failure strength are identical as illustrated in Figure 31. The hybrid composite being tested will act as a brittle material. This is due to the chopped carbon fiber having a small elongation at fracture

of 0.0198. The elongation at fracture is how much the material can strain in tension until fracture.

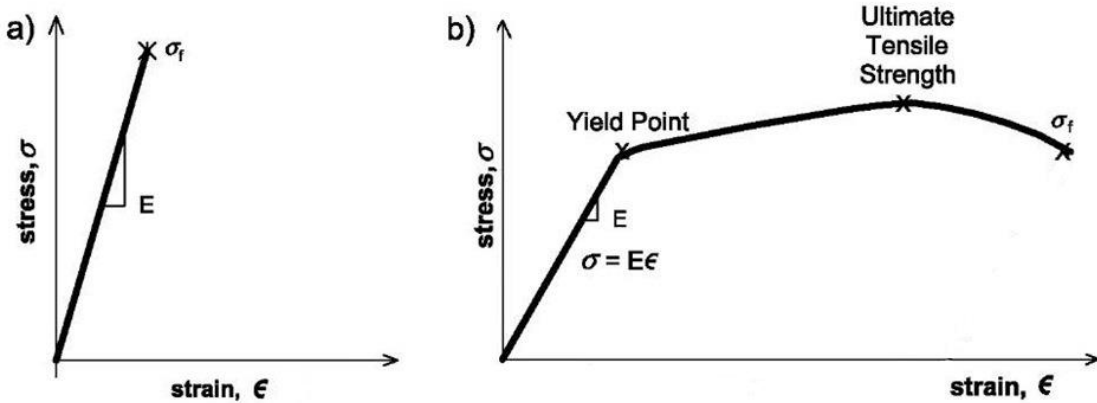
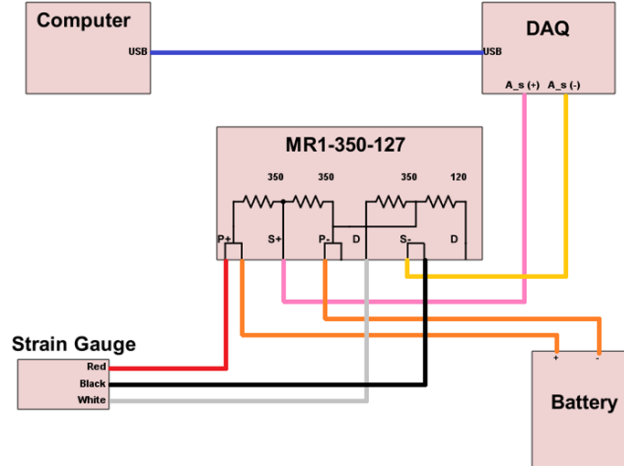


Figure 31: Stress-strain curves for brittle (a) and ductile (b) materials

### 3.5 Data Collection

Data collection is performed with data acquisition. Data acquisition is the process of sampling signals that measure real world physical conditions and converting the results into digital numeric values. A computer is used for processing and storing measurement data. This experiment uses a data acquisition device that converts the strain gage's physical change into an electrical signal and records the point through special software. The software being used for the strain in this experiment is the National Instrument Signals Express package. The software will be recording change in strain vs time. A tutorial of the National Instrument Signals Express software is provided in Appendix B: Specimen Data Collection Procedure.

The strain gage elongations are very small, so the signal is small. In order to boost these small changes in resistance, a bridge completion module is used. A bridge completion module is a more robust version of a Wheatstone bridge [33]. A Wheatstone bridge is an electrical circuit used to accurately measure resistance changes [34]. The bridge completion module is more convenient than a Wheatstone bridge and is used with different types of strain gages. Each of the three strain gages in the stacked rosette geometry requires its own bridge completion module. The data acquisition circuit for a single strain gage is shown in Figure 32. The data acquisition unit used for this experiment is a National Instruments 6009.



**Figure 32: Data acquisition circuit**

The pull test machine also has its own special data acquisition software. This software is Bluehill® . This software controls the rate at which the machine changes force, called the strain rate. The strain rate for this experiment is set at  $0.001\frac{1}{s}$ . The software records tensile stress in MPa, load in N, and extension of the machine in mm. All of these values are recorded against time.

After the data acquisition software is ready, the specimen is placed in the machine. Data acquisition starts and records data until the specimen is fractured across the gage section. The tensile test machine stops automatically when it senses fracture of the specimen. A machine mounted, fractured composite specimen is shown in Figure 33.

The collected strain and stress data is used to approximate the elastic modulus. To do this the strain data must be filtered because of the high sensitivity of the strain gages. Matlab is used to filter the noisy strain gage data. A control specimen of only matrix is tested first to validate the testing procedure. The matrix comes with a data sheet that has a given elastic modulus and tensile strength. The control specimen results are shown in Figure 34.

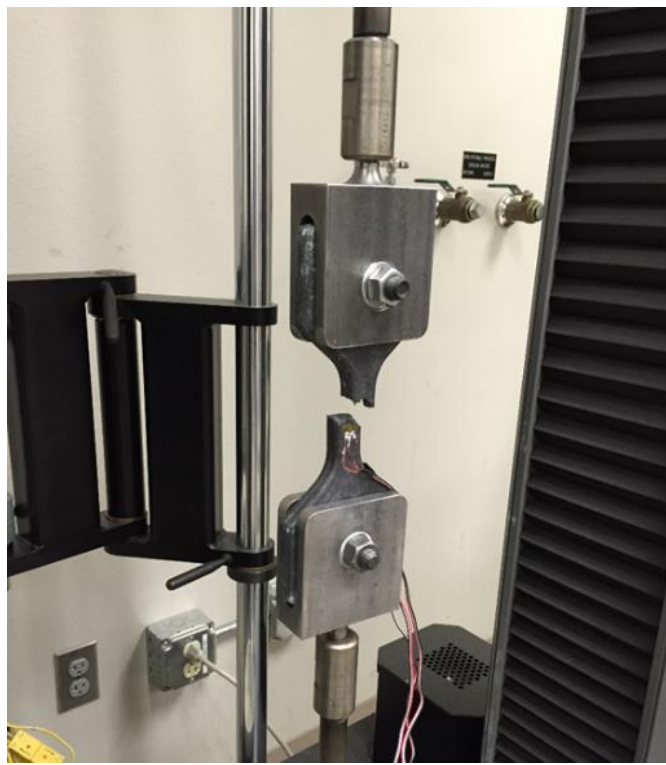


Figure 33: Fractured composite specimen

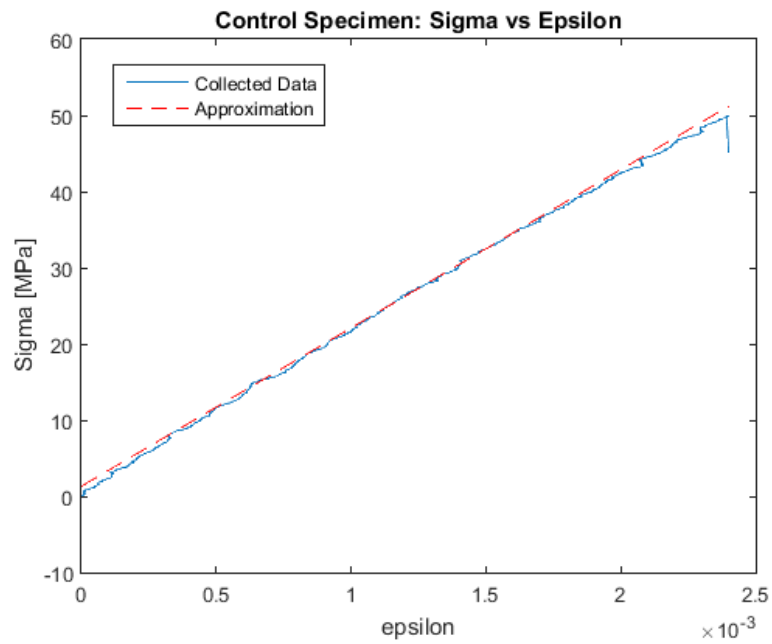


Figure 34: Control Specimen stress vs strain

The results of the control test are shown in Table 3. The region of linear elastic behavior is approximated with a straight line.

**Table 3: Control specimen results**

	<b>Data Sheet Specs</b>	<b>Collected Results</b>	<b>Difference (%)</b>
<b>Elastic Modulus (GPa)</b>	1.98	2.2	11.1%
<b>Tensile Strength (MPa)</b>	46.0	45.9	-2.2%

### 3.6 Composite Testing Results

The results for uniaxial tensile testing of the hybrid composite are shown in this section. The specimen number in the left column denotes sample then case. For example, 1\_2 indicates sample 1, case 2. Specimens 3\_2 and 7\_2 failed because of strain gage software malfunction. Once the tensile test machine starts, you cannot cancel it. The tensile testing machine independently collects stress data. Because of this, the maximum stress is shown for the two specimens, but not the elastic modulus data. The data will be plotted against composite mechanics equations presented in chapter 2.

**Table 4: Elastic modulus and tensile strength results**

<b>Specimen #</b>	<b>Elastic Modulus (GPa)</b>	<b>RMS of Linear Approximation vs Collected Data</b>	<b>Ultimate Tensile Strength (MPa)</b>
1_1	20.7	2.5	49.9
2_1	26.9	5.6	42.1
3_1	22.2	1.3	31.0
4_1	43.5	5.8	47.4
5_1	14.2	53.2	46.0
6_1	25.8	9.8	27.3
7_1	21.5	42.9	38.5
8_1	46.6	25.3	59.5
9_1	2.5	6.3	40.8
1_2	25.2	2.2	46.2
2_2	39.2	1.7	37.5
3_2	Fail	--	36.4
4_2	21.2	21.6	45.8
5_2	28.5	21.2	44.1
6_2	25.0	10.0	36.8
7_2	Fail	--	38.0
8_2	50.0	7.1	42.0
9_2	2.2	2.4	45.9

Using equation 2.6, a surface is created to map the elastic modulus vs iron particle and chopped fiber reinforcement shown in Figure 35. Lee's composite strength model, equation 2.28, is used to create a surface mapping the strength of the composite vs iron particle and chopped fiber reinforcement shown in Figure 36. Chen's composite strength model, equation 2.29, is used to create a surface mapping the strength of the composite vs iron particle and chopped fiber reinforcement shown in Figure 37. A surface is created to map Poisson's ratio, equation 2.7, vs. iron particle and chopped fiber reinforcement shown in Figure 38.

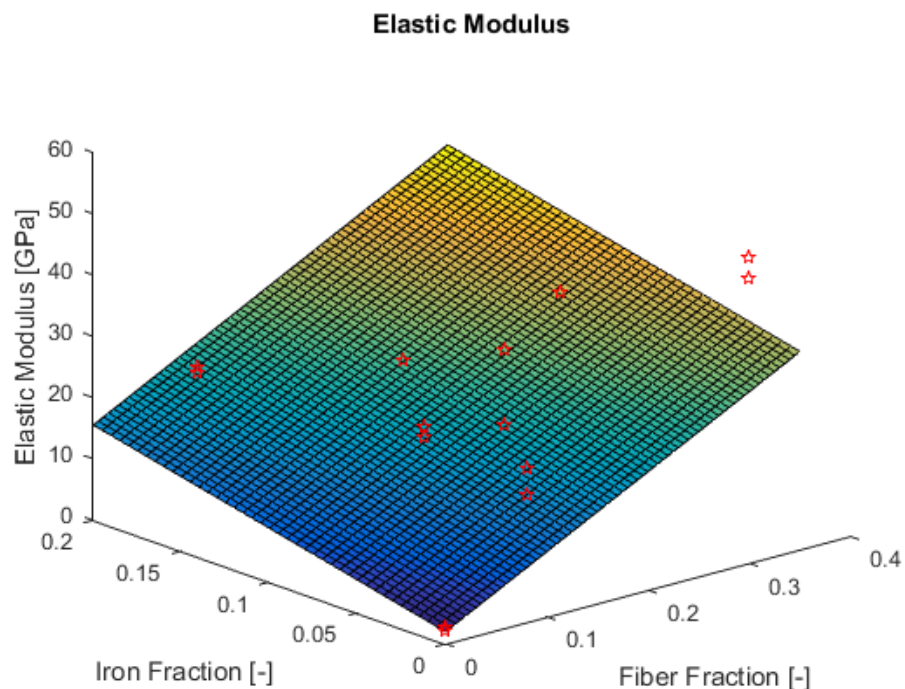


**Figure 35: Elastic modulus vs iron particle and chopped fiber reinforcement**

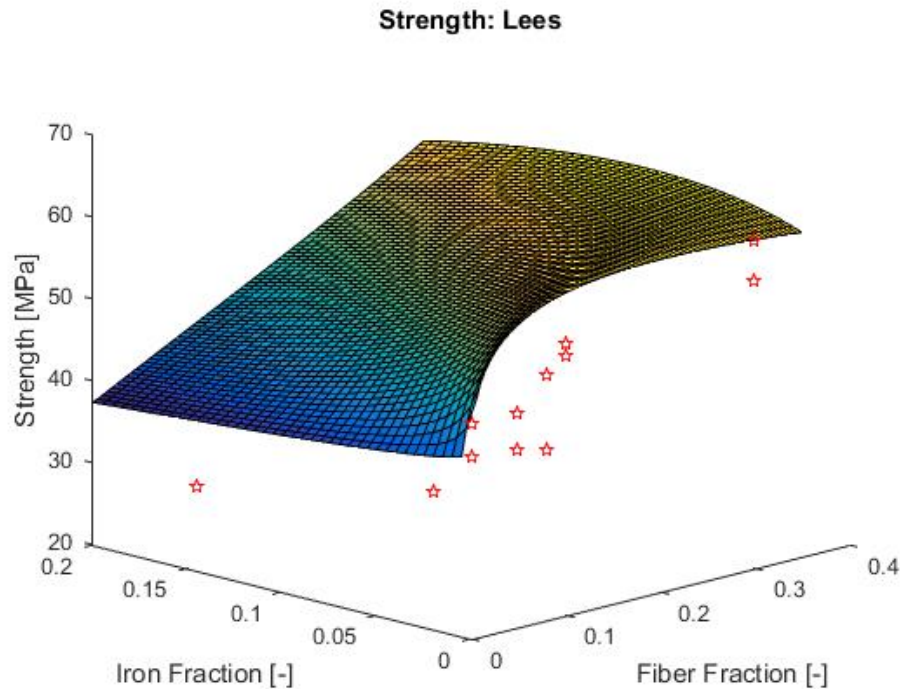


Figure 36: Lees' Strength vs iron particle and chopped fiber reinforcement

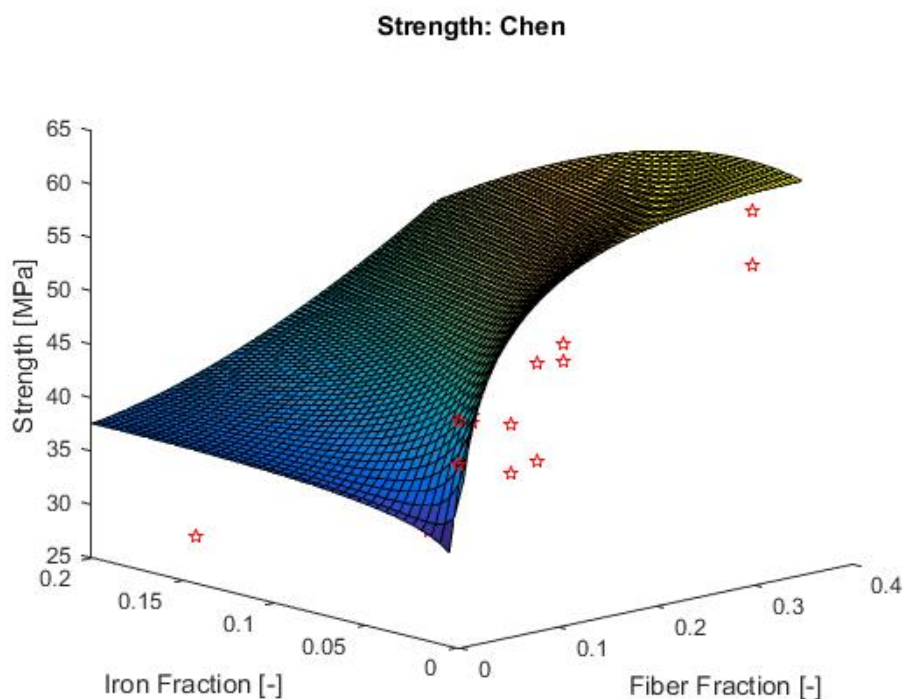
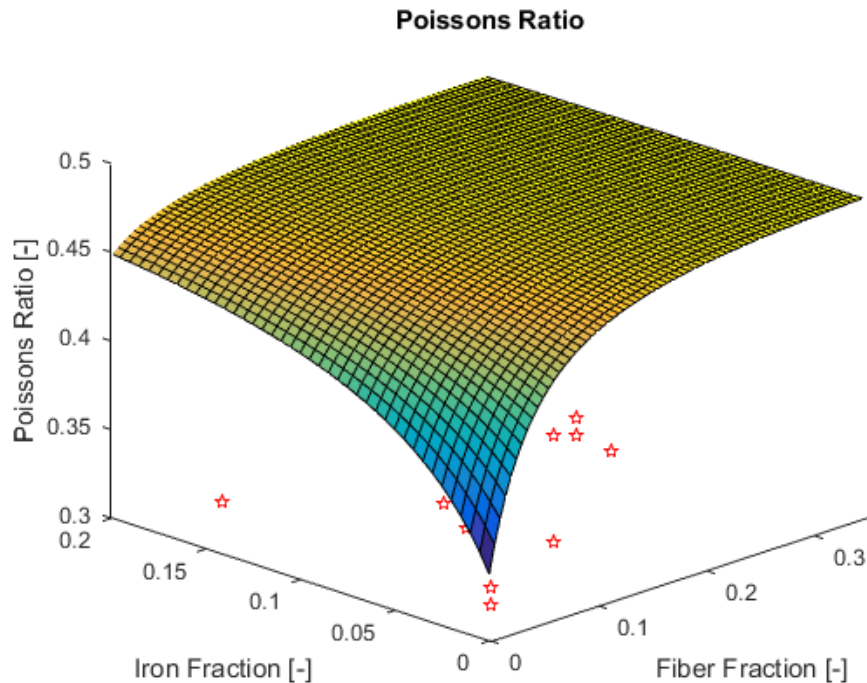


Figure 37: Chen's Strength vs iron particle and chopped fiber reinforcement



**Figure 38:** Poisson's ratio vs iron particle and chopped fiber reinforcement

The elastic modulus results from the experiment are compared with the surface in Figure 35 and presented in Table 5.

**Table 5: Elastic modulus error values**

<b>Specimen #</b>	<b>Elastic Modulus (GPa)</b>	<b>Elastic Modulus Approximation (GPa)</b>	<b>Error (%)</b>
1_1	20.79	8.92	57
2_1	26.97	14.78	45
3_1	22.26	15.42	31
4_1	43.55	22.74	48
5_1	14.2	22.47	58
6_1	25.89	17.85	31
7_1	21.51	26.14	22
8_1	46.64	28.02	40
9_1	2.58	1.985	23
1_2	25.2	8.92	65
2_2	39.21	14.78	62
3_2	0	0	00
4_2	21.2	22.74	07
5_2	28.56	22.47	21
6_2	25	17.85	29
7_2	0	0	0
8_2	50.05	28.02	44
9_2	2.2	1.985	10

**Avg. Error**      **37**

The strength results from the experiment are compared with the surfaces in Figure 36 and Figure 37. The data is presented in Table 6.

**Table 6: Strength error values**

<b>Specimen #</b>	<b>Ultimate Tensile Strength (MPa)</b>	<b>Lees (MPa)</b>	<b>Error (%)</b>	<b>Chen (MPa)</b>	<b>Error (%)</b>
1_1	49.95	58.66	17	55.68	11
2_1	42.1	57.01	35	53.4	27
3_1	31.05	51.71	67	47.05	52
4_1	47.48	59.45	25	57.04	20
5_1	46	52.19	13	47.6	03
6_1	27.38	41.26	51	38.77	42
7_1	38.55	60.76	58	52.12	35
8_1	59.53	60.1	01	61.7	4
9_1	40.86	45.36	11	34.22	16
1_2	46.2	58.66	27	55.68	21
2_2	37.52	57.01	52	53.4	42
3_2	36.43	51.71	42	47.05	29
4_2	45.86	59.45	30	57.04	24
5_2	44.15	52.19	18	47.6	08
6_2	36.87	41.26	12	38.77	05
7_2	38	60.76	60	52.12	37
8_2	42.03	60.1	43	61.7	47
9_2	45.9	45.36	01	34.22	25

**Avg. Error****31****Avg. Error****25**

**Table 7: Poisson's ratio error values**

<b>Specimen #</b>	<b>Experimental</b>	<b>Analytical</b>	<b>Error (%)</b>
1_1	0.4	0.45	11
2_1	0.38	0.47	19
3_1	0.32	0.46	30
4_1	0.46	0.47	2
5_1	0.31	0.47	34
6_1	0.29	0.46	37
7_1	0.29	0.48	40
8_1	0.19	0.48	60
9_1	0.32	0.34	6
1_2	0.41	0.45	9
2_2	0.32	0.47	32
3_2	0	0.46	0
4_2	0.35	0.47	26
5_2	0.37	0.47	21
6_2	0.31	0.46	33
7_2	0	0.48	0
8_2	0.29	0.48	40
9_2	0.33	0.34	3

**Avg. Error**      **25**

### **3.7 Composite Mechanics Discussion and Conclusion**

In this chapter, tensile testing techniques were discussed to compare discontinuous-randomly oriented isotropic mechanical properties developed in chapter 2. How to design a specimen, mold design, molding process, and measurements were discussed. Specimens consisting of chopped carbon fiber, iron particles, and a thermoset matrix material were constructed. Latin hypercube sampling was used to spread the design space of the specimens. A uniaxial pull test was used to determine the maximum tensile strength of each composite material. A stacked rosette strain gage configuration was used to find the Young's modulus and Poisson's ratio of each composite mixture. The results from the experiments were compared to the composite mechanics discussed in chapter 2.

The overall error of the uniaxial testing data was mostly due to the manufacturing process. The manufacturing process could be improved, but at high expenses. Construction of test

specimens could be advance with the use of vacuum bagging. Vacuum bagging is a technique employed to create mechanical pressure on a composite during its cure cycle. The technique removes all of the air trapped within the composite. The molds were originally set up to use vacuum bagging, but limited resources did not allow the technique to be used. There are other advanced methods of composite creation [35]. The specimens could also be 3D printed with expensive equipment [36]. The process can be used to eliminate most of the unwanted air. One of the most expense processes is a pressure molding process. With these types of components, extreme pressure and temperature are applied with a dry matrix to create the composite [37] [19]. The pressure applied is on the order of 500MPa and the temperature is around 100°C. The pressure and temperature ensure air removal and a higher bonding strength of the two materials. The pressure bonding technique can be used to tailor specific needs the component, but comes at a high cost.

Although the air percentage in each specimen can be quantified, there is not a way of telling where the air pockets are located without expensive equipment. The impact of air pockets creates stress concentrations in the material, therefore, lowering the maximum tensile strength. The equations discussed in chapter 2 are under the assumption that the material is uniformly distributed within the component. Without costly equipment, such as an x-ray diffraction device, there is no way to ensure that the material is perfectly distributed through the gage length.

With knowledge of improving the manufacturing process, with more expensive equipment, the data presented in Table 5, Table 6, and Table 7 has a low enough error to proceed to the modeling process, incorporating the discontinuous randomly oriented reinforced composite results.

## 4 Mechanical Rotor Model

The high speed flywheel energy storage system (HSFESS) has been pre-determined to be an “inside-out” design [5]. This means that the rotor spins about the stationary stator. High temperature superconductors are used to levitate the rotor to control its vertical degree of freedom. The use of passive levitation removes the need for a shaft as the high temperature superconductors keep the rotor locked vertically in place, while allowing the rotor to rotate freely about the circular axis. The rotation about this axis allows the rotor to be modeled as a rotating hollow cylinder. When a hollow cylinder is rotating with a constant angular velocity, material particles are subjected to a centripetal acceleration. The acceleration leads to an inertial force which in turn leads to stresses in the cylinder. As the angular velocity of the rotor increases, the stress also increases. By use of Hooke’s law, the stresses lead to strains and ultimately displacements. The rotor stress must be lower than the failure strength of the material so rotor does not fracture. A model to accurately predict stresses and displacements in the rotor based on geometry, material, and operating conditions is needed to design an energy dense flywheel in this configuration.

In this chapter, physical makeup of the HSFESS will be examined. This chapter outlines the original rotor model created at the University of Idaho by Brenden F. Kaschmitter [12]. Kaschmitter’s model is used to obtain cylindrical dimensions to optimize kinetic energy storage of the HSFESS given geometrical constraints and operating limits. A further extension to Kaschmitter’s model to map mechanical characteristics of the HSFESS rotor will be developed. The model will use finite element analysis (FEA) software to quantify localized stress in areas of interest, given geometry and material characteristics of the flywheel. The FEA data will be used to construct a semivariogram to process desired outputs of maximum stress and deformation in the rotor. The semivariogram will be used along with a Kriging/Gaussian process to predict stochastic outputs in the constrained design space. Three different rotor models will be discussed:

1. An empty chevron model that mimics the LSFESS.
2. A model that has material in the chevrons and includes sliding effects. This model is created to map stress and displacement at the inner edge of the rotor with two separate materials.

3. A model that has material in the chevrons that is bonded to the rotor material. This model is used to explore a carbon fiber composite as a more desirable material because of its high strength to weight ratio and ability to reduce sliding created along material boundaries by bonding the materials together.

## **4.1 HSFESS Mechanical Composition**

Work performed by the University of Idaho's low speed flywheel energy storage system (LSFESS) set the building blocks in place to design a more energy dense flywheel storage system. Building off of work done by the LSFESS is a key starting point of the HSFESS. The HSFESS will have the same general geometry of the LSFESS, but with a goal to maximize kinetic energy storage while still maintaining a high efficiency and material integrity. Other constraints are also present in the goal and will be discussed later in the chapter.

In order to maximize kinetic energy storage, equation 1.1, it is more advantageous to spin at high angular speeds than to increase the moment of inertia. In order to minimize the centrifugal force and radial displacement, a composite rotor with multiple physical rings has been chosen. Physical rings are defined as different materials as shown in Figure 39. The reason for multiple physical rings is to allow the flywheel to have a magnetically permeable material for the inside ring, so the stator is able to produce a torque on the rotor to spin the flywheel and store mechanical energy [8]. Another use of multiple physical rings is to reduce the stress in the permeable ring using a high strength, low density material around the outside of the rotor. The multiple physical rings can also be used to achieve a uniform deflection along the inside edge of the rotor [12]. One of the constraints of the rotor is minimizing the gap between the stator and the rotor as the angular velocity of the rotor increases. This gap must remain radially constant so the stator is able to provide a torque on the rotor more efficiently. Kaschmitter's implementation of a composite rotor with multiple physical rings will be discussed in the next section.

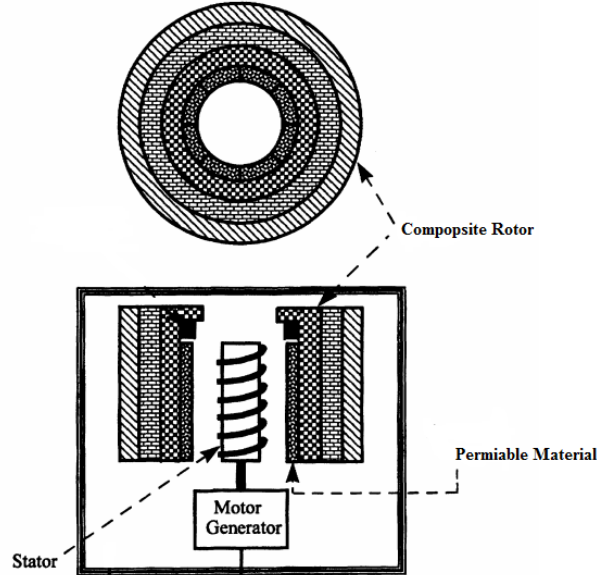


Figure 39: Composite flywheel diagram with multiple rings [38]

## 4.2 Axisymmetric Rotor Model

A University of Idaho M.S.M.E. student created a model to optimize geometry and angular velocity of the rotor to maximize the kinetic energy storage of the flywheel. A flywheel with multiple physical rings is chosen to control stress and deflection of the flywheel. The optimization limits the stress of the flywheel under material strengths so the rotor stays intact under the highest angular velocity.

Kaschmitter used an axisymmetric model developed by Sung K. Ha that uses a numerical solving method. The model is developed using a plain strain assumption for an axisymmetric flywheel [38]. The flywheel is assumed thick enough for this assumption to be valid. The model chosen is capable of having multiple physical rings. Kaschmitter first started with a model of an isotropic, homogenous rotor.

The model was compared to the analytical stress and displacement equations for an isotropic material with a constant thickness rotating at a specified angular velocity. The analytical equations are [39]:

$$\sigma_r = \frac{3 + \nu}{8} \rho \omega^2 \left[ a^2 + b^2 - r^2 - \frac{a^2 b^2}{r^2} \right] \quad 4.1$$

$$\sigma_\theta = \frac{3+\nu}{8} \rho \omega^2 \left[ a^2 + b^2 - \frac{1+3\nu}{3+\nu} r^2 + \frac{a^2 b^2}{r^2} \right] \quad 4.2$$

$$u_r = \frac{3+\nu}{8} \rho \omega^2 \frac{1-\nu}{E} r \left[ a^2 + b^2 - \frac{1+\nu}{3+\nu} r^2 + \frac{1+\nu}{1-\nu} \frac{a^2 b^2}{r^2} \right] \quad 4.3$$

where  $\sigma_r$ ,  $\sigma_\theta$ , and  $u_r$  are the radial stress, circumferential stress, and radial displacement, respectively. The variables  $a$  and  $b$  are the inner and outer radius and  $r$  is a continuous variable for the radial distance from  $a$  to  $b$ . The variables  $\rho$ ,  $\omega$ ,  $E$ , and  $\nu$  represent the density, rotational velocity, elastic modulus and Poisson's ratio, respectively.

The model did not match the isotropic equations exactly, however, the errors are relatively small. The hoop stress,  $\sigma_\theta$ , which is the highest stress, shows an error of approximately 5%. The radial stress,  $\sigma_r$ , shows a 5% error. The mechanics of materials approach results in approximate values. The Ha model [12] discretizes the flywheel into a number of finite numerical rings rather than a continuous object. The displacement shows a larger error of approximately 10%. The larger error is a result of the numerical model being derived from a plain strain assumption and equation 4.3 being derived in a plane stress assumption.

The results are acceptable, so the model was adjusted to incorporate the high strength carbon fiber composite as one of the physical rings. Using the same outside dimensions for the flywheel, the hoop stress and radial displacement were reduced by approximately 70% when the full iron flywheel was partially replaced by high strength composite. Lower stresses indicate that adjusting geometrical parameters and rotational velocity to reduce stress under yielding while still maintaining a high energy storage is feasible.

If the angular velocity of the rotor becomes great (>20,000rpm) [12], the gap between the stator and inner rotor surface increases well past the desired 1mm. Keeping the gap as close to 1mm as possible is needed to keep efficiency of the machine high. To achieve the desired gap, Kaschmitter proposed to taper the inside surface of the rotor and the stator as shown in Figure 40. The superconductors supporting levitation could then be actuated up and

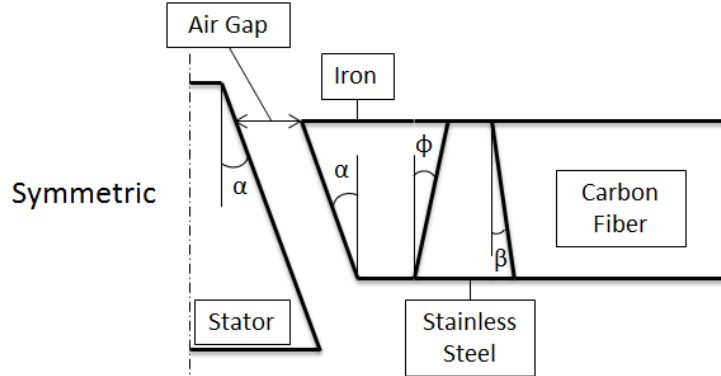


**Figure 40: Tapered composite flywheel [12]**

down as the speed decreases or increases. A material between the permeable material, iron, and high strength composite, carbon fiber, is also angled. The two angles,  $\phi$  and  $\beta$  are chosen such that the deflection across the inner edge is constant. These angles ensure the gap between the stator to the rotor is constant. A more complicated system is needed to increase the speed past 20,000rpm. The actuation of the superconductors and sensors provide difficult obstacles to overcome. The model is functional if needed, but other constraints have deemed a tapered stator model undesirable.

Kaschmitter's model is used to optimize geometry for kinetic energy storage. The optimization provides geometry of the flywheel while limiting stress under material strength. This model can be used with multiple physical rings, but the rings are seen as perfectly cylindrical. The model gives an accurate size of the flywheel to maximize kinetic energy storage, but it does not incorporate the localized stress concentrations created by the geometry of the permeable material in the rotor.

### 4.3 Localized Stress Model Approach

When a current is applied to the stator, a magnetic field is produced that causes the rotor to spin. The magnetic field can be represented as two magnetic poles: a north and south pole. The rotor is essentially a large electromagnet. For the HSFESS a field regulated reluctance machine (FRRM) has been chosen as the machine topology. A FRRM is a higher energy dense machine than an induction machine [40]. The FRRM has been proven by the University of Idaho's low speed flywheel energy storage system (LSFESS) team, and therefore, is chosen as the operating mechanism for the HSFESS.

For the FRRM, the rotor's poles are salient, meaning they protrude out from the cylindrical surface of the rotor [41]. The salient pole regions and interpole regions (also called chevrons) can be related to each other through the saliency ratio, which is a ratio of the inductance in the d-axis to the q-axis ( $L_d/L_q$ ) shown in Figure 41. Increasing the saliency ratio increases the torque produced by the stator on the rotor. The saliency ratio is dependent on the interpole region, and therefore the chevron design.

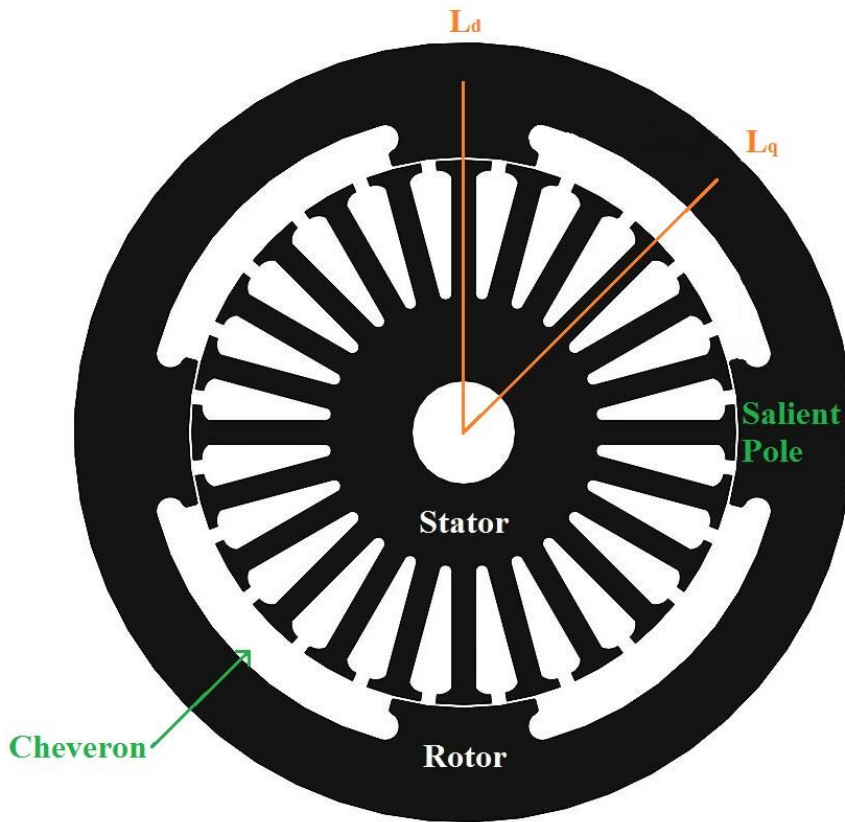


**Figure 41: Salient poles and chevron inductance**

The design of the salient poles proposes a mechanical problem. A localized increase in stress will form around the salient poles and chevron interface. A non-uniform stress will be present in these areas because of the geometric discontinuities. The non-uniformity in stress distribution results in a maximum stress at a section that is considerably larger than the average stress [31]. The analysis of geometric shapes to determine the stress concentration factor, which determines the localized maximum stress, is a difficult problem and not many analytical solutions exist [32]. To find the increased maximum stress around the salient poles

and chevron regions will require the use of finite element analysis (FEA). Using FEA does not guarantee finding the true maximum stress because the elements are finite [22].

Nonetheless, the approach is an improvement on the understanding of localized maximum stress in the spinning device displayed in Figure 42.

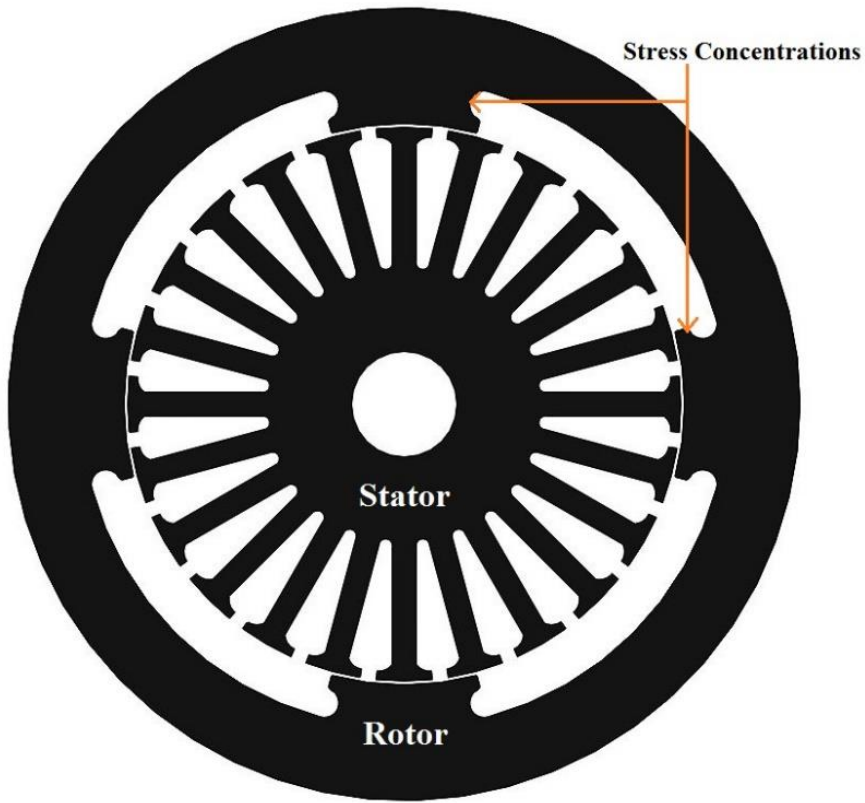


**Figure 42: Rotor stress concentrations**

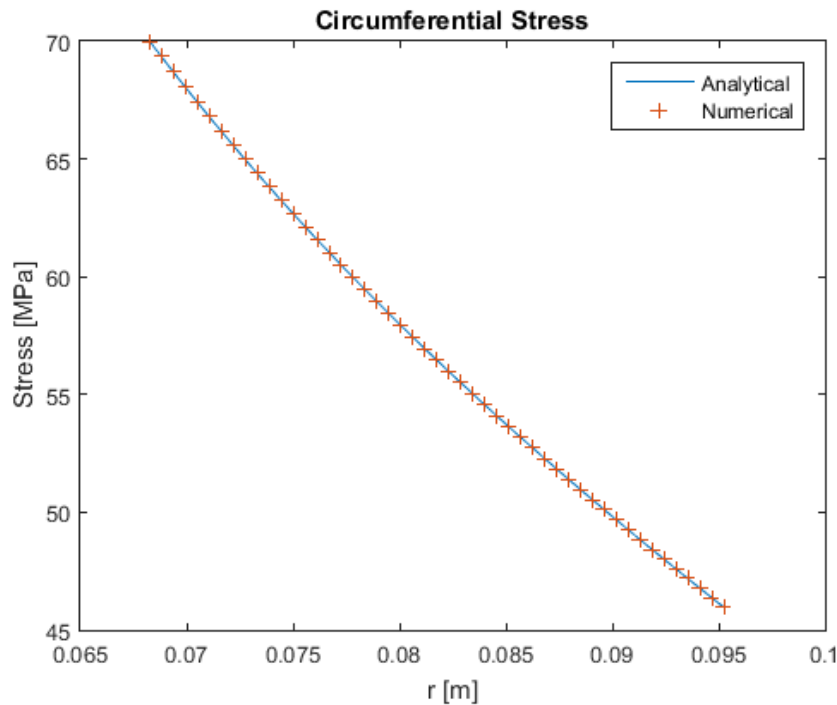
#### 4.3.1 Simple FEA Model

FEA methods are numerical methods for approximating the solutions to mathematical problems [22]. Representing the actual, physical domain with an approximation requires the identification of correct boundary conditions and understanding of problem formulation. To conclude that models have correct boundary conditions and are functioning properly, a simple analytical model is used to ensure accurate results. Using equations 4.1, and 4.2 for an isotropic material with a constant thickness rotating at a specified angular velocity, numerical FEA results are compared to the known analytical solution. The inputs for the two solutions are located in Table 8 and are analogous to the LSFESS.

**Table 8: Simple FEA model inputs**

Property	Value
Elastic Modulus ( $E$ )	200 GPa
Poisson's Ratio ( $\nu$ )	0.29
Density ( $\rho$ )	7700 $\frac{\text{kg}}{\text{m}^3}$

The numerical simulation is a very thin slice of material with boundary conditions that enforce the plane strain assumption. The plain strain assumption states that the component being analyzed is prismatic down its length and the stress at any cut section through the length will be duplicated. The HSFESS is assumed thick enough for this assumption to be valid. The results for the circumferential stress,  $\sigma_\theta$ , and radial stress,  $\sigma_r$ , are shown in Figure 43 and Figure 44, respectively.

**Figure 43: Analytical and numerical comparison of circumferential stress vs radial distance**

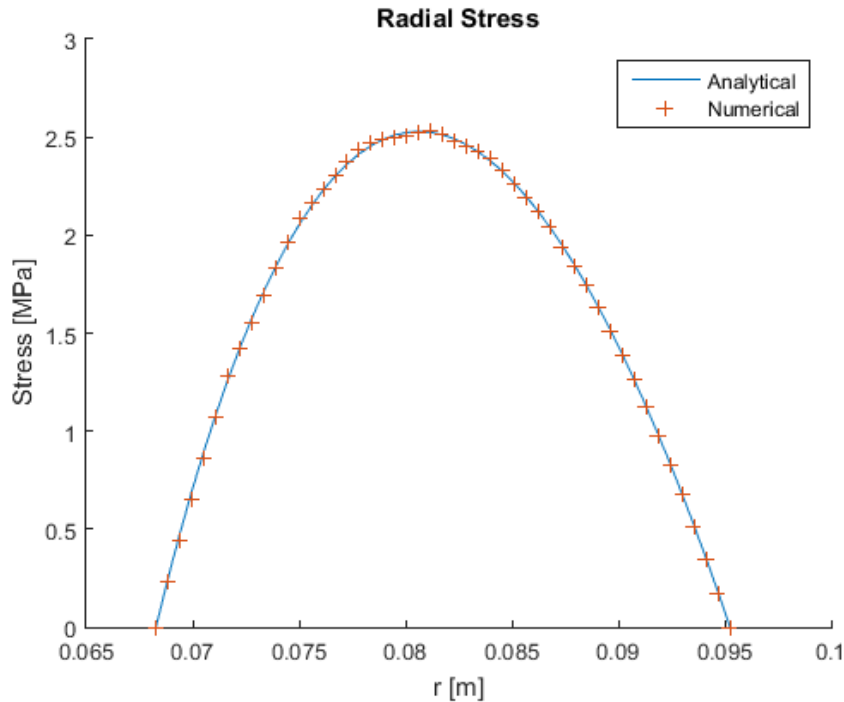


**Figure 44: Analytical and numerical comparison of radial stress vs radial distance**

The displacement of the inner surface of the rotor is also an import aspect of the FRRM. The airgap between the stator and the rotor has the highest reluctance. Reluctance is analogous to resistance in an electrical circuit. The higher the reluctance, the harder it is to move magnetic flux through a given path. The relationship of the reluctance to the airgap is an inverse relationship, and as the airgap increases the reluctance change is exponential [7]. To store more energy, increasing the flywheel's rotational speed is more advantageous than increasing the moment of inertia. At high speeds the material will deform radially increasing the airgap. Knowing how the airgap changes is important to be able to predict what the efficiency of the machine will be given the airgap. The same cylindrical FEA model is used to compare the numerical results to the analytical results from equation 4.3. The radial displacement results are show in Figure 45.

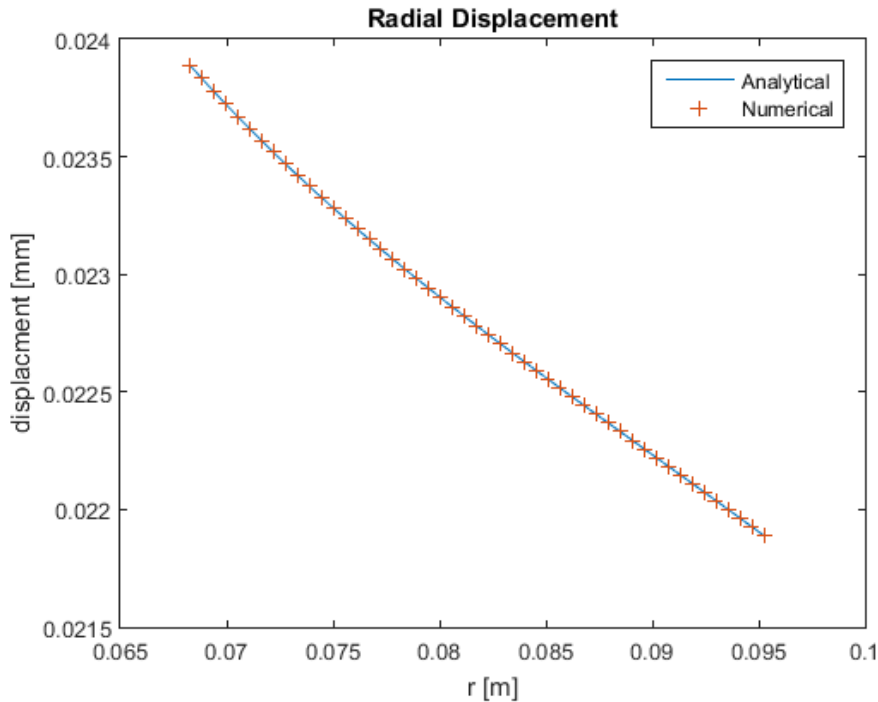


**Figure 45: Analytical and numerical comparison of radial displacement vs radial distance**

For the circumferential stress in Figure 43, which is the highest stress, the simulation predicts a stress of 0.0041% lower than the analytical equation from 4.2. The radial stress from Figure 44 displays a simulation error of 0.13% higher than the analytical results of equation 4.1. The radial displacement from Figure 45 displays a simulation error of 0.00011% higher than the analytical results from equation 4.3.

While the simulation does not match the analytical equations perfectly, the errors are very small. The isotropic equations were derived from a linear-elastic, mechanics of materials approach which results in approximate values. Some assumptions include linear-elastic behavior, homogeneous and uniform properties throughout [31]. The analytical and numerical solutions share the same domain, but the numerical solutions are represented by the finite linear combinations of analytical functions. The FEA solution is an approximation because it relies on calculations done at discrete points, rather than a continuum. The discrete points are appointed by a mesh size density set by the user. Where the mesh crosses is a node and in between nodes is the non-nodal area. As the mesh density becomes finer and finer, the solution will reach convergence. An assumption of the numerical solution includes a linear strain distribution from node to node based on a first order polynomial fit [42]. The values

computed at nodes are used to approximate values at non-nodal points by interpolation of nodal values. The stress in the rotor is an important output to depict mechanical failure, and the accuracy compared to the analytical solution deduces to further expand on the localized stress distribution.

#### **4.3.2 Model Adjustments: Kaschmitter's Simulation**

To produce accurate FEA simulations, using the same parameters as Kaschmitter's model, requires the connection of the two representations. The FEA simulation uses values computed at nodes to simulate the domain. Using more nodes increases needed computation power and time. To decrease the amount of nodes being used, a plane strain analysis is used. The HSFESS is assumed thick enough to validate this assumption. A very thin slice of the rotor is examined with boundary conditions that enforce the plain strain assumption. To further reduce the amount of nodes being used, the FEA model utilizes boundary conditions. The high strength carbon fiber composite can be removed from the analysis and replaced with a boundary condition that is equal to the orthotropic material's elastic moduli. To validate this approach, Kaschmitter's model was used as a comparison for the FEA simulation. The results of the stress comparison and displacement comparison are shown in Figure 46 and Figure 47, respectively. The lines on the graph represent Kaschmitter's numerical simulations, while the cross hatches are the FEA simulation. The FEA simulation is only performed on the inner magnetically permeable material because it is the weakest material in the flywheel. The carbon fiber is excluded from the FEA simulation, but is replaced by boundary conditions. The dotted lines on the plots represent material boundaries.

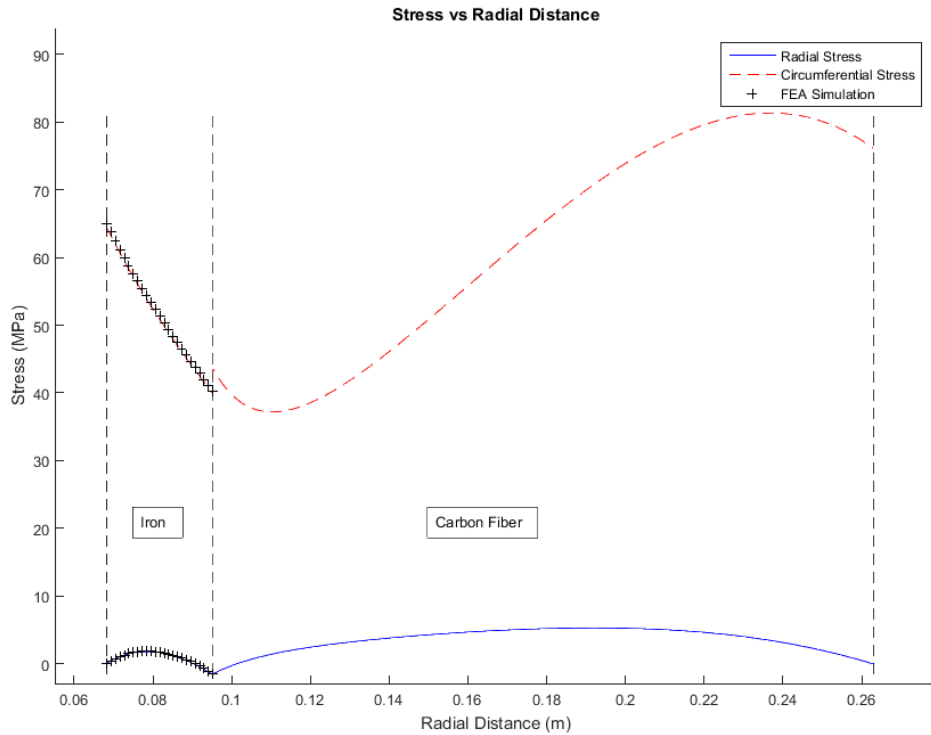


Figure 46: FEA and Kaschmitter's model comparison of stress vs radial distance

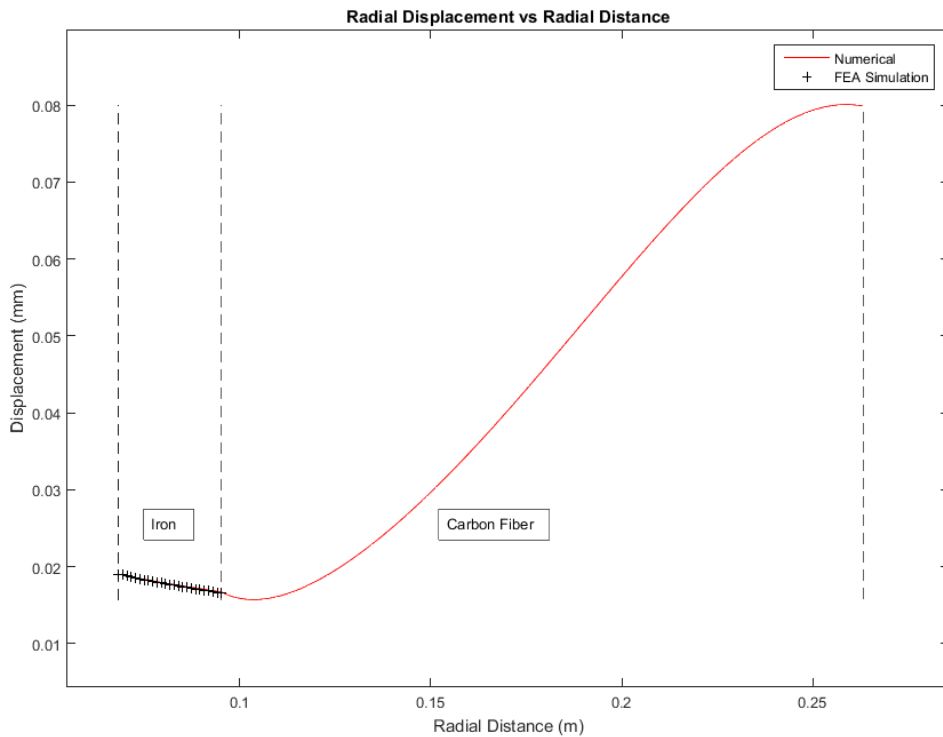


Figure 47: FEA and Kaschmitter's model comparison of radial displacement vs radial distance

For the circumferential stress in Figure 46, which is the highest stress, the FEA simulation predicts a stress of 2.04% lower than Kaschmitter's numerical model. The radial stress from Figure 46 displays an FEA simulation error of 2.04% lower than Kaschmitter's numerical model. The radial displacement from Figure 47 displays a FEA simulation error of 1.68% higher than the analytical results from equation 4.3.

Both of the simulations are approximations, but the errors between the two are small. Again, the models were developed from a linear-elastic, mechanics of materials approach rather than a continuum approach. This approach simplifies the models by omitting small details. Element order also contributes to the error between the two models. This means that the solving order of elements between boundary conditions for the two models is not the same. Because the errors are small, advancement to incorporate localized stress and displacement is synthesized.

#### **4.4 Localized Stress Model**

Changing the FEA simulation to incorporate the localized stress and displacement is straightforward, as the simple axisymmetric model has been verified. The chevrons introduce stress concentrations, Figure 42, but are a required element to more efficiently spin the rotor around the stator. Maintaining a high efficiency is a requirement of the HSFESS project. Another requirement of the project is to keep the flywheel from yielding in the localized stress areas. If the stress passes the yield stress, some of energy that is stored cannot be returned because that energy is used to plastically deform the material. Plastic deformation is also undesirable because the rotor will not return to its original dimensions. The unwanted plastic deformation would permanently change the stationary airgap. The stationary reluctance of the airgap would increase subsequently decreasing efficiency of the machine. Knowing the airgap at a given speed must also be incorporated into the model so the rotor can be successfully controlled by the moving magnetic field.

The localized stress and radial displacement do not have closed form equations. Building a flywheel and testing erroneous sets of geometry would not be effective experimental testing. This is why FEA is chosen to evaluate the rotor. Even with FEA, mapping the entire design space with every single possibility of rotor geometry/material characteristics given known bounds, requires too much time and resources. What if the material needs to change because

of an unknown constraint in the future? What if mass of the flywheel is limited because of superconductor/magnet physics? Because of the theory stage of the project, these type of questions cannot be ignored if limited resources are to be maximized.

The bounds of some parameters have been discovered by Kaschmitter's model, but other questions need to be answered. The approximate size of the rotor is known, but how does chevron geometry/material effect the stress? How does changing the geometry/material influence the localized stress? How much does airgap change given geometry/material characteristics? The complexity of the physics and design space infers the use of a surrogate model. A surrogate model is used to expedite simulations by reducing the time for computation at the cost of rigor and generality [43]. A surrogate model is a mathematical black box model that reproduces the output of a more complex phenomena.

#### 4.4.1 Kriging/Gaussian Process

One method of creating estimates with a surrogate model is a Kriging/Gaussian process. The Kriging process quantifies the uncertainty associated with predicted estimates. In the complex physical design space of the HSFESS, knowing prediction's uncertainty is beneficial. The Kriging method is an interpolation method. All interpolation algorithms estimate the value at a given location as a weighted sum of data values at surrounding locations [44]. The surrounding locations determine weights according to functions that give a decreasing weight with increasing distance between data value locations. Kriging assigns these weights according to data-driven functions, rather than an arbitrary function [44]. The goal is to determine the weights that minimizes the variance of the prediction. The basic form of the Kriging estimator,  $Y^*(\mathbf{u})$ , is [45]:

$$Y^*(\mathbf{u}) - m(\mathbf{u}) = \sum_{i=1}^{num(u)} \lambda_i [Y(\mathbf{u}_i) - m(\mathbf{u}_i)] \quad 4.4$$

where

- $\mathbf{u}$  and  $\mathbf{u}_i$  are location vectors for the point to be estimated and one of the neighboring points indexed by  $i$
- $num(u)$  is the number of data points in the local neighborhood used for the estimation of  $Y^*(\mathbf{u})$

- $m(\mathbf{u})$  and  $m(\mathbf{u}_i)$  are expected means of  $Y(\mathbf{u})$  and  $Y(\mathbf{u}_i)$
- $\lambda_i$  is the Kriging weight assigned to  $Y(\mathbf{u}_i)$  for estimating location  $\mathbf{u}$

The Kriging weights,  $\lambda_i$ , are derived from covariance functions that characterize the residual component,  $R(\mathbf{u})$  ( $R(\mathbf{u}) = Y(\mathbf{u}) - m(\mathbf{u})$ ). Covariance is defined as a measure of how much two random variables change together. To minimize the variance of the estimator an unbiased constraint is used with a mean of zero and covariance that is only a function of lag distance,  $\mathbf{h}$ , but not position,  $\mathbf{u}$  [45]:

$$E\{R(\mathbf{u})\} = 0 \quad 4.5$$

$$E\{R(\mathbf{u}) \cdot R(\mathbf{u} + \mathbf{h})\} = C_R(\mathbf{h}) \quad 4.6$$

The lag distance is the theoretical distance in the design space. The residual covariance,  $C_R(\mathbf{h})$ , is derived from a semivariogram model. The semivariance,  $\gamma$ , is the difference between the residual covariance at a lag distance of 0 and a lag distance of  $\mathbf{h}$  [45]:

$$\gamma(\mathbf{h}) = C_R(0) - C_R(\mathbf{h}) \quad 4.7$$

The semivariogram determines the difference in correlation, semivariance, as a function of lag distance [44]. A semivariance of 0 indicates that the two values are perfectly correlated and have a covariance of 0. A large semivariance is just the opposite, that is, the values are less correlated. The covariance of the residual at a lag distance of 0, is also referred to as the sill, c. The lag distance where the semivariogram reaches the sill is referred to as the range, a. Where the semivariogram intercepts the semivariance axis is called the nugget. A diagram of a semivariogram is shown in Figure 48.

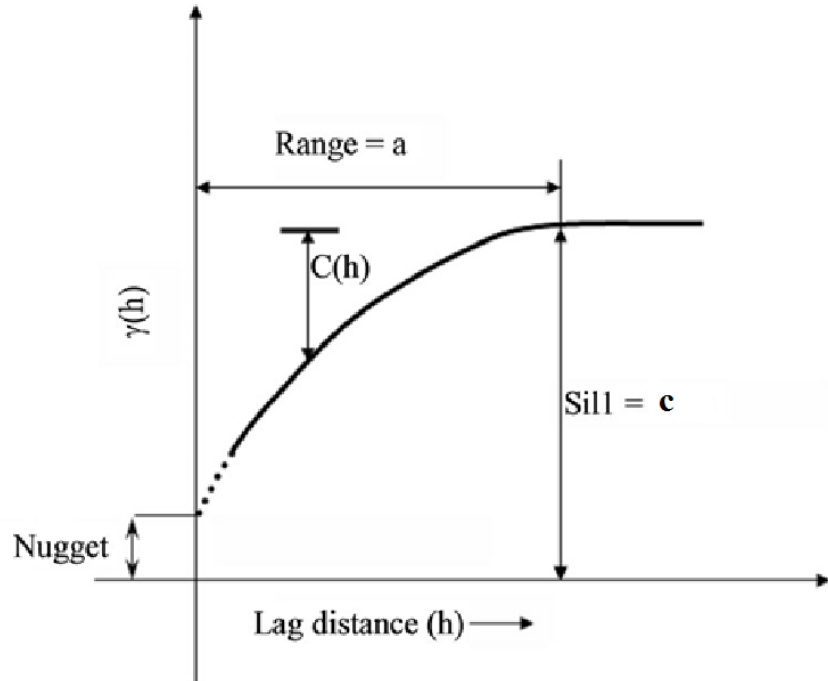


**Figure 48: Diagram of semivariogram**

In the case of a Kriging model, there is not an empirical representation of a semivariogram, only recorded data points. Evaluating semivariance as a function of lag requires a pair of points for any one semivariance. A semivariogram will need to be fit to the data points to approximate the semivariance. Considering each lag distance individually, can create a lot of noise, and the number of lag distances can become very high given a large data set. To eradicate this problem, lag distances are grouped together into bins depending on their design space distance from one another. The bins have a range of lag distances that each lag distance will be put into. The bins are each about the same size and contain about the same number of lag distances, forcing the data set to be unbiased. The semivariance is evaluated for each bin depending on the lag distance. With the semivariance of the bins plotted against the lag distance, a curve can be fit to obtain an empirical model for the semivariogram. An example of the observed bins and empirical relationship is shown in Figure 49.

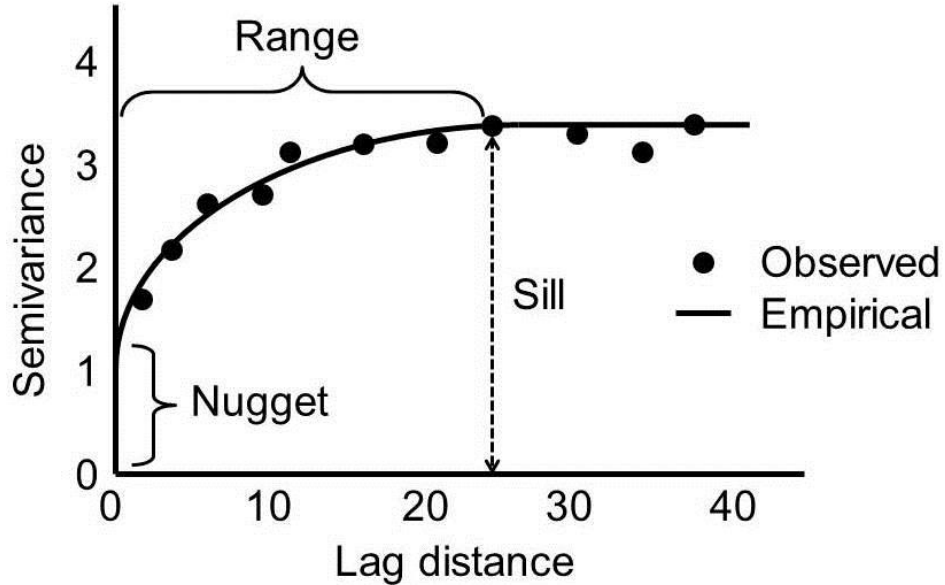


Figure 49: Semivariance of empirical relationship fitted to observed bins

There are a number of different forms of the semivariogram to fit observed data. The three discussed in this paper are spherical, exponential, and Gaussian. The forms of the semivariogram fits,  $g(\mathbf{h})$ , for each equation are [46]:

$$\text{Spherical} \quad g(\mathbf{h}) = \begin{cases} c \left[ 1.5 \left( \frac{h}{a} \right) - 0.5 \left( \frac{h}{a} \right)^3 \right] & \text{if } h \leq a \\ c & \text{if } h > a \end{cases} \quad 4.8$$

$$\text{Exponential} \quad g(\mathbf{h}) = c \left[ 1 - \exp \left( \frac{-3h}{a} \right) \right] \quad 4.9$$

$$\text{Gaussian} \quad g(\mathbf{h}) = c \left[ 1 - \exp \left( \frac{-3h}{a^2} \right) \right] \quad 4.10$$

The relationship between the semivariance depending on lag distance is found with one of the semivariogram fits, but in order to make a prediction based on a set of untested inputs, a Kriging variant is used. There are two forms of Kriging discussed here: simple and ordinary. With simple kriging the trend component,  $m(\mathbf{u})$ , is a constant. This means that every unknown point in the design space is initially assumed to have the same trend value. This approach has good accuracy for problems where the output does not change very much, but its validity decreases as the output has a wide range [44]. The localized stress concentrations will vary widely with changes of inputs. For this non-linear design space, simple Kriging is an

undesirable variant. Ordinary Kriging assumes that the mean is not global. The mean is only constant in a local neighborhood of the estimated point. The complexity of the design space dictates the use of an ordinary Kriging model. The form of the ordinary Kriging estimator is [45]:

$$Y^*(\mathbf{u}) - m(\mathbf{u}) = \sum_{i=1}^{num(u)} \lambda_i Y(\mathbf{u}_i) + \left[ 1 - \sum_{i=1}^{num(u)} \lambda_i(\mathbf{u}) \right] m(\mathbf{u}) \quad 4.11$$

The Kriging weights,  $\lambda_i$ , can be constrained to a local trend component by requiring that they sum to 1. A Lagrange parameter,  $\mu_o$ , is also introduced to force the system to minimize the variance error. The following system of equations are used to solve for the ordinary Kriging weights [45]:

$$\sum_{j=1}^{num(u)} \lambda_j(\mathbf{u}) C_R(\mathbf{u}_i - \mathbf{u}_j) + \mu_o(\mathbf{u}) = C_R(\mathbf{u}_i - \mathbf{u}) \quad i = 1, \dots, num(\mathbf{u}) \quad 4.12$$

$$\sum_{j=1}^{num(u)} \lambda_j(\mathbf{u}) = 1 \quad 4.13$$

This system of equations can also be written in matrix form as [45]:

$$\mathbf{K}\bar{\lambda} = \mathbf{k} \quad 4.14$$

where

- $\mathbf{K}$  is a matrix of covariances between data points
  - o  $K_{ij} = C_R(\mathbf{u}_i - \mathbf{u}_j)$
- $\mathbf{k}$  is a vector of covariances between the data points and the estimation point
  - o  $k_i = C_R(\mathbf{u}_i - \mathbf{u})$
- $\bar{\lambda}$  is the vector of the ordinary Kriging weights system of equations 4.12 and 4.13

After solving for the ordinary Kriging weights and Lagrange parameter using equation 4.14, an estimated trend value prediction,  $Y^*$ , and variance,  $\sigma^2$ , can be found using the following equations [45]:

$$Y^*(\mathbf{u}) = \sum_{i=1}^{num(u)} \lambda_i Y(\mathbf{u}_i) \quad 4.15$$

$$\sigma^2(\mathbf{u}) = C(0) - \lambda^T(\mathbf{u}) \mathbf{k} \quad 4.16$$

#### 4.4.2 Localized Stress Model Creation

Now that a surrogate model type, ordinary Kriging, has been chosen, data points need to be collected from the different configurations of chevron designs. The design variables that control the configurations must be quantifiable. This ensures that the semivariogram will be able to estimate a mean and standard deviation based on all input variables. For the type of model used in this analysis, the inputs are deterministic. A deterministic input is one that does not have any uncertainty associated with it. The values input into the model are absolutely correct. This is different than the output that is considered stochastic. Stochastic output is one where a design variable set produces a range of results for an output of interest; in this case a mean and standard deviation from the Kriging model.

The design variables chosen to incorporate into the model are illustrated in Figure 50

- $N_o$  is an outside notch radius. The notch radius is chosen as a variable because of the localized stress concentrations associated with notches.
- $N_i$  is an inside notch radius.  $N_i$  is chosen for the same reason as  $N_o$ .
- $C_w$  is the width of the salient pole. A wider salient pole increases the amount of material associated with the salient pole. The magnetic flux also has a larger area to move through. More material designates more rotational mass that increases the stress on the rotor.
- $R_i$  is the inside radius of the chevron. A larger inside radius increases the saliency ratio, which allows the stator to increase the torque on the rotor.
- $R_o$  is the outside radius of the permeable material. A larger outside radius increases rotor mass and radius to the center of the rotor. This increases the stress on the rotor.

Not pictured in Figure 50:

- $E$ , the elastic modulus is also chosen as a design variable because of Hooke's law.
- $\rho$ , the density of that material is chosen because the interaction it has in equations 4.1, 4.2, and 4.3.

- $\nu$ , Poisson's ratio is chosen because of Hooke's law.
- $\omega$ , the rotational speed of the rotor is chosen because of the effects it has in equations 4.1, 4.2, and 4.3.

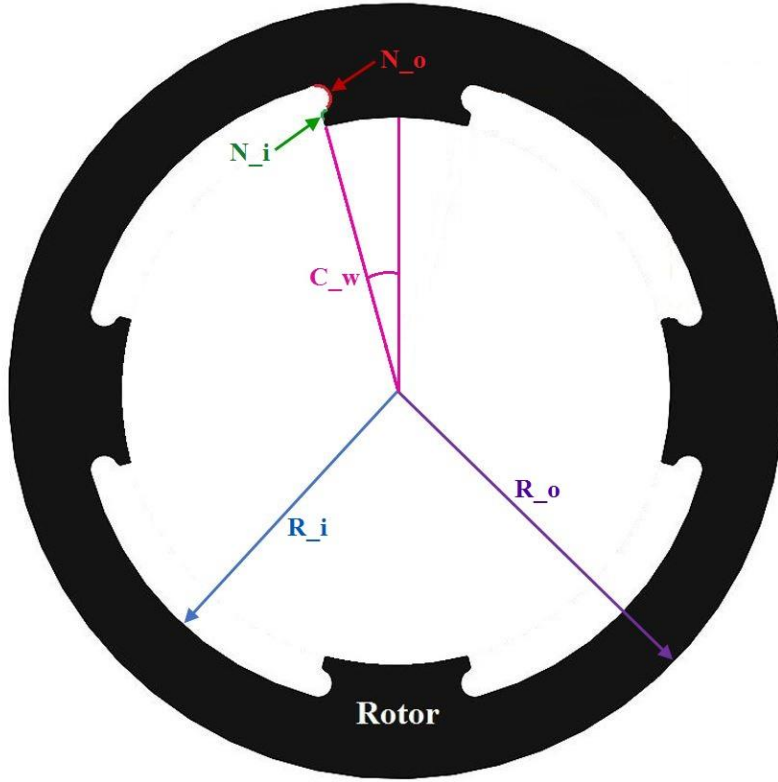


**Figure 50: Rotor design variables**

To create a semivariogram, a range of each design variable is needed. Other constant variables are also needed to create the geometry to input into the FEA model, such as the inside radius of the salient pole,  $R_s$ . Kaschmitter's model predicts the optimal flywheel configuration in cylindrical dimensions at a resolved rotational speed. Maintaining the thickness of the high strength carbon fiber on the outside of the rotor, allows  $R_s$  to be determined and  $R_o$  to be narrowed down to a range close to what Kaschmitter's model predicts. An upper bound of rotational speed is also dictated by Kaschmitter's model. Because the chevron gaps must all be constant to maintain control of the FRRM, the salient pole width,  $C_w$ , has a maximum of  $22.5^\circ$  before the salient pole regions are the same size as the chevron. To ensure this doesn't happen, an upper bound of  $C_w$  is set to  $20^\circ$ . A lower bound is dictated

by the geometry of the chevron:  $R_i$ ,  $N_o$  and  $N_i$ . The inner chevron radius,  $R_i$  can only be in between  $R_o$  and  $R_s$ . The notch radii,  $N_o$  and  $N_i$ , are also dictated by the geometry of the chevron. The elastic modulus and, density, and Poisson's ratio are all material specific. Many materials will be tested, and these inputs must be provided as a physical known material to the Kriging model. The model solves for many material inputs, but the material must be available. Several constraints must be evaluated before the design parameters enter the Kriging model. This ensures that a physical geometrically possible rotor design is being evaluated. Geometric constraints and design variable bounds are given in Table 9.

**Table 9: Geometric constraints and design variable bounds**

$0 < R_o - R_i - 2N_o - N_i$	in
$0 < R_s \tan(C_w) - N_o$	in
$0.125 < N_o < 0.425$	in
$0.0375 < N_i < 0.5$	in
$5 < C_w < 20$	deg
$3 < R_i < 4$	in
$3.6 < R_o < 4.6$	in
$10,000 < \omega < 25,000$	rpm
$R_s = 2.65$	in

From a mechanical standpoint the rotational stress needs to be lower than the materials strength. Reducing the density of the material reduces the stress imposed on the rotor. From an electrical standpoint the permeability of the material needs to be high and the deflection across the airgap from the stator to the rotor needs to be minimized. The two different needs of the mechanical and electrical divisions are against each other. Almost all high permeable materials have a high density. A high density creates more rotational stress and a larger airgap at a given elastic modulus and rotational speed. The composite mechanics discussed in chapter 2 are used to test a few different iron-particle-composite mixtures. The carbon-fiber-iron-particle-composite mixture will be used later in this chapter. The composite mixtures have a lower density than iron itself, but at a cost of lower permeability. A finite element method for magnetics using the same rotor design variables will be discussed in the next chapter. The elastic modulus, Poisson's ratio and yield strength of the iron-particle-composite mixture are found from equations 2.6, 2.7, and 2.29 respectively. Other materials are also

tested. Materials with different densities, moduli, and Poisson's ratios are tested to map the material design space. A list of materials used with corresponding characteristics are provided in Table 10.

**Table 10: Tested Materials**

Material	Yield Strength (MPa)	UTS (MPa)	Elastic Modulus (GPa)	Density (kg/m <sup>3</sup> )	Poisson's Ratio
Iron Composite 30%		42	22.5	3313	0.45
Iron Composite 50%		36	36.7	4484	0.46
Iron Composite 70%		23	51.8	5835	0.47
Aluminum Alloy	280	310	71	2770	0.33
Iron	130	240	110	7200	0.28
Steel	250	460	200	7850	0.3
Titanium Alloy	930	1070	96	4620	0.36
Silica Steel	290	434	151	7700	0.3
Magnesium Alloy	193	255	45	1800	0.35

Now that the design variable ranges have been decided, 45 different geometry configurations are created. The 45 different configurations are each tested at 4 different rotational velocities spread throughout the range of  $\omega$ . The FEA models also incorporate the 9 different materials. All of the geometric configurations are physical and adhere to the constraints in Table 9. A semivariogram that best fits the set of data can now be found for each of the three models.

Three separate models are created to map the wanted design spaces: an empty chevron model, a model that has material in the chevrons and includes slipping effects, and a model that has material in the chevrons but does not include any slipping. The model with no material in the chevron is used to replicate the LSFESS. The model with material in the

chevrons is created to try and reduce the displacement at the inside surface of the rotor. A stronger, lighter material can be used in the chevron gaps to try and achieve the smaller airgap. As the displacement increases, it is harder for the machine to push magnetic flux through the airgap. The idea is to be able to map the design space of the two-material model to see how the effects of adding more material, which leads to more stress, will impact the displacement of the inner rotor surface. The final model has material in the chevrons, but negates slipping effects. This configuration is possible because of advanced manufacturing processes. The process is only allowed with composite materials. Composite materials can be created by a 3D printing process [36]. This enables the composite rotor to be impregnated with iron, while limiting the chevrons to only contain a chopped carbon fiber composite. At the interface, the two materials would be bonded together in this manufacturing process. Because of the flexibility of the chopped carbon fiber composite material characteristics, Figure 35, Figure 36, Figure 37, and Figure 38, the two composite material mechanics can be matched. This means the two composite materials can have close to the same elastic moduli and Poisson's ratios.

#### **4.4.3 Empty Chevron Model**

An empty chevron model mimics the design of the LSFESS. This flywheel does not have any material in the chevrons. The empty chevron model uses 45 different geometries, 4 speeds and 9 materials. This makes 1620 total data points to create a semivariogram. The semivariance fit equations, 4.8, 4.9, and 4.10 are used to map the stress in the rotor.

Figure 51 shows the plot of each fit for the empty chevron stress model. Visually the plots are compared to the plotted bins, but the semivariogram characteristics are shown in Table 11.

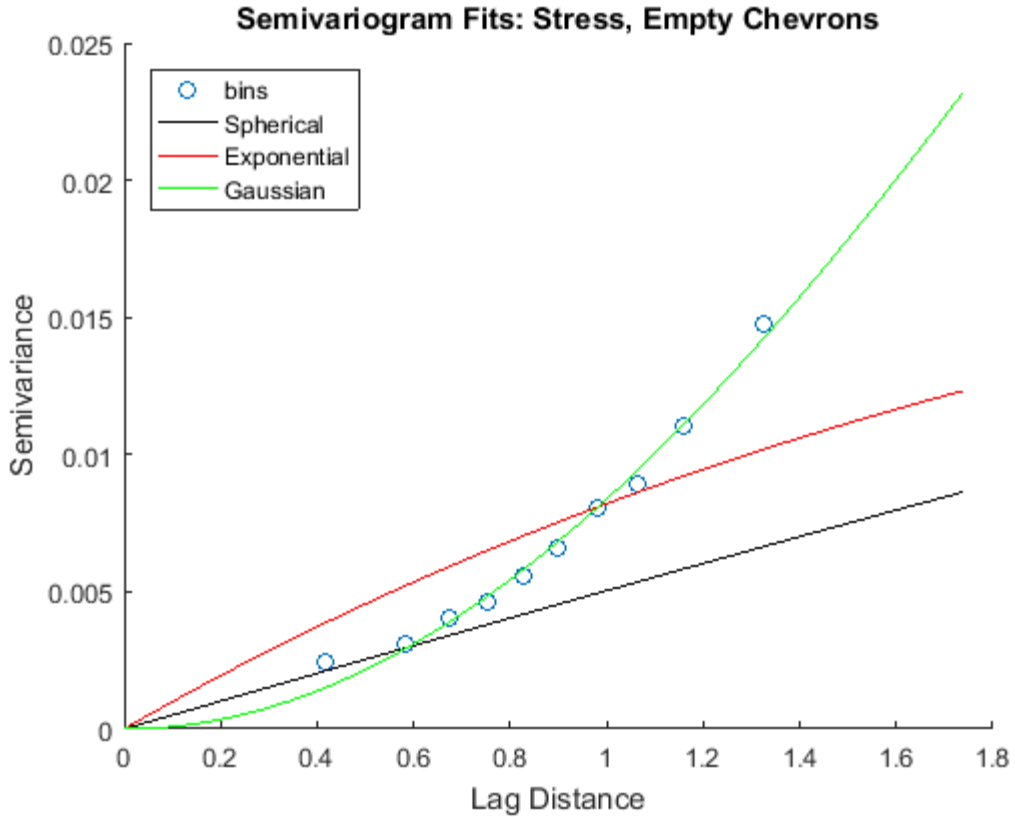


**Figure 51:** Semivariogram of stress fits: empty chevrons

**Table 11:** Semivariogram of stress characteristics: empty chevrons

Fit	Sill (c)	Range (a)	Residual Error
Spherical	0.038	6.72	2.81E-05
Exponential	0.023	6.79	4.07E-05
Gaussian	0.098	5.79	1.43E-06
<b>Number of Bins</b>		10	

From Table 11 and Figure 51 the Gaussian fit seems to fit the data the best. The residual error of the Gaussian fit is also the lowest. For these reasons, the semivariogram used for the empty chevron stress model is the Gaussian curve fit.

Figure 52 shows the plot of each fit for the empty chevron displacement model. Visually the plots are compared to the plotted bins, but the semivariogram characteristics are shown in Table 12.

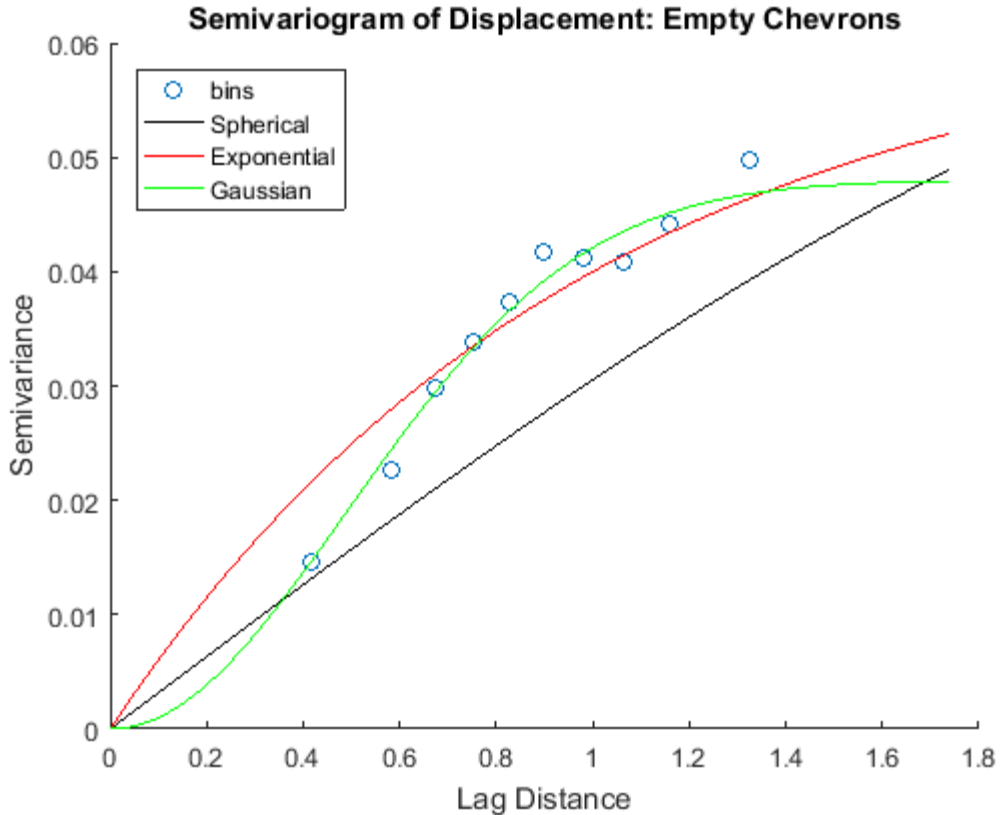


Figure 52: Semivariogram of displacement fits: empty chevrons

Table 12: Semivariogram of displacement characteristics: empty chevrons

Fit	Sill (c)	Range (a)	Residual Error
Spherical	0.054	1.76	5.79E-05
Exponential	0.063	2.98	1.16E-04
Gaussian	0.048	1.2	2.75E-05
<b>Number of Bins</b>		10	

The residual error of the Gaussian curve fit is the lowest for the empty chevron displacement model. The semivariogram fit used to map the displacement data of the rotor is the Gaussian curve fit.

#### 4.4.4 Filled Chevrons, No Separation Model

Adding material in the chevrons that is light, but strong can impact how the material displaces at the airgap from the stator to the rotor. For this reason a no separation model that includes slipping effects, but does not allow the material to separate in the FEA software, is

explored. The rotor/stator airgap must remain small so the efficiency of the machine stays high. If the gap becomes too large, the machine must work harder to push the magnetic flux through the larger airgap. This is because the reluctance of the airgap is the highest in system. Reluctance is the property of a magnetic circuit that opposes the passage of magnetic flux. The larger the airgap, the higher the reluctance in the system. A two-material model is created to explore the maximum stress, given a set of two materials, and the displacement at the inner surface of the rotor. 45 separate geometries and 4 rotational speeds that adhere to Table 9 are used in this analysis.

Materials listed in Table 10 are used to create the different sets configurations. The total possible sets of combinations for the given 9 materials is 72. To reduce this number of possibilities, but still explore the entire design space, Latin hypercube sampling is used (See chapter 3). The combinations of materials are shown in Table 13.

**Table 13: Filled chevron material iterations**

Chevron Material	Rotor Material
Iron Composite 30%	Silica Steel
Iron Composite 50%	Iron Composite 70%
Iron Composite 70%	Steel
Aluminum Alloy	Iron Composite 50%
Iron	Iron Composite 30%
Steel	Titanium Alloy
Titanium Alloy	Magnesium Alloy
Silica Steel	Iron
Magnesium Alloy	Aluminum Alloy

Semivariograms are created with the collected data points. The semivariograms map the maximum stress and displacement on the inner edge of the salient pole in the two material no separation model.

From Figure 53 the semivariogram for the stress that fits the no-separation filled chevrons model the best is the Gaussian form. The Gaussian residual error is also the lowest for the given data from Table 14.

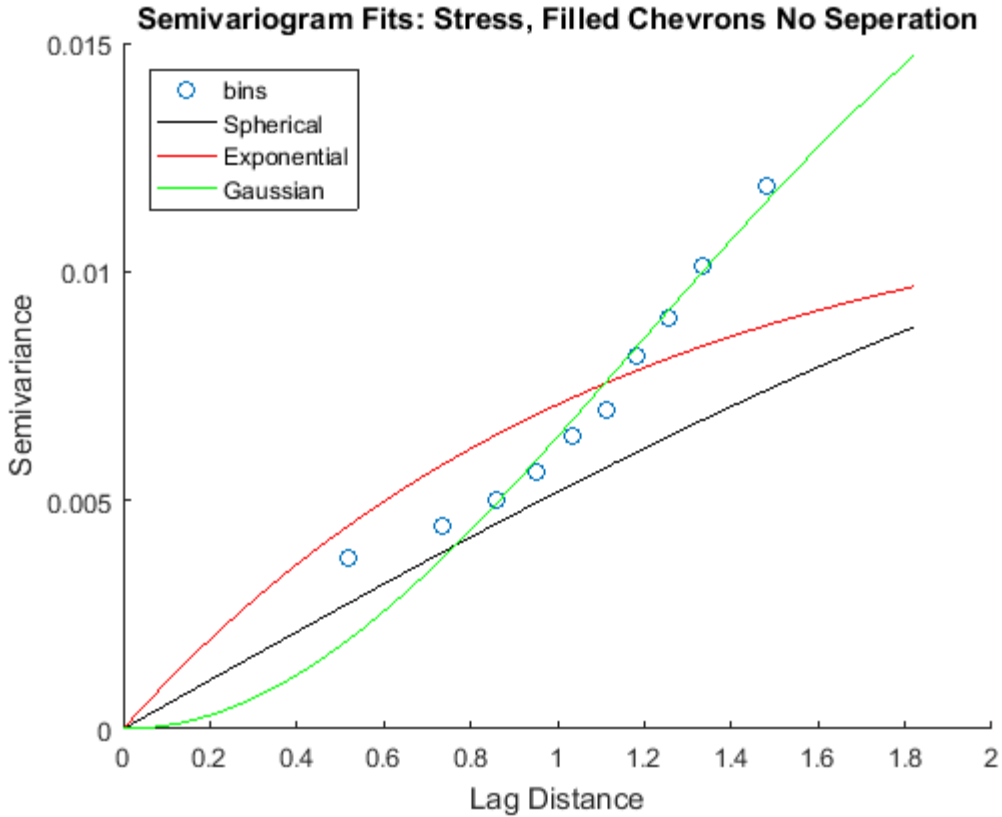


**Figure 53:** Semivariogram of stress fits: filled chevrons no separation model

**Table 14:** Semivariogram of stress characteristics: filled chevrons no separation model

Fit	Sill (c)	Range (a)	Residual Error
Spherical	0.0181	3.8	8.36E-06
Exponential	0.0121	3.4	2.02E-05
Gaussian	0.0211	2.88	3.44E-06
<b>Number of Bins</b>		10	

From Figure 54, the semivariogram for the displacement that fits the no-separation filled chevrons model the best is the exponential form. The exponential residual error is also the lowest for the given data from Table 15.

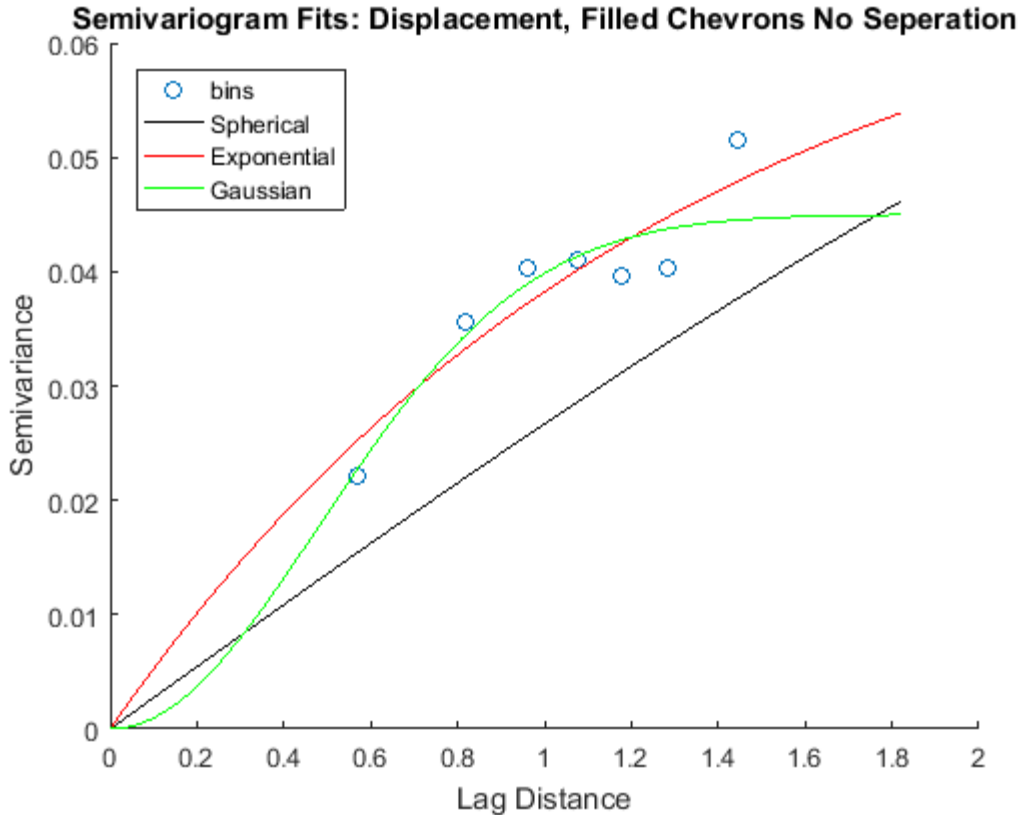


Figure 54: Semivariogram of displacement fits: filled chevrons no separation model

Table 15: Semivariogram of displacement characteristics: filled chevrons no separation model

Fit	Sill (c)	Range (a)	Residual Error
Spherical	0.051	1.79	7.21E-05
Exponential	0.072	3.96	6.85E-05
Gaussian	0.045	1.18	7.53E-05
<b>Number of Bins</b>		7	

#### 4.4.5 Filled Chevrons, Bonded Model

A high strength to weight ratio is more advantageous to increase the kinetic energy storage, equation 1.1. The higher the strength to weigh ratio in a rotating object, the lower the stresses are at a given angular velocity, equations 4.1 and 4.2. The displacement is also lower with a high strength to weight ratio, equation 4.3. A composite material has the ability to have a high strength to weight ratio. It also has the ability to be manufactured in ways that a metal cannot. New technology enables the use of pressure molding [37] and 3D printing of composite

materials [36]. The composite also has the ability to be impregnated with magnetically permeable particles, like iron, to give it the characteristics desired in electromagnetic applications. The two materials are bonded together in this process. For these reasons, composites possess desirable characteristics for a HSFESS.

Filling the chevron areas with a material has an effect on the displacement and stress seen in the rotor. In this model, the two materials are bonded together through innovative manufacturing techniques that are only available to composites. Bonding the materials together effects the stress and displacement of in the rotor. The composite material in the chevrons can also be tailored to match the material characteristics of the rotor material. This would essentially make the boundary between the rotor and chevrons mechanically invisible, while still providing the electromechanical differences needed between the two materials.

The materials tested for this model are shown in Table 16. Titanium and aluminum were chosen for analysis because of their strength to weight ratios. These two materials do not have the ability to be manufactured this way, but composites are available that are closely mimic their material characteristics. The density of aluminum and titanium also expands the model to design space that could be advantageous to explore. A material that is only a carbon fiber composite is introduced because of its high strength to weigh ratio. The rotor is only filled with magnetically permeable composite material, while the chevron is filled with magnetically inert material.

**Table 16: Filled chevron (bonded) material iterations**

Chevron Material	Rotor Material
Carbon Fiber Composite	Iron Composite 50%
Aluminum Alloy	Iron Composite 50%
Titanium Alloy	Iron Composite 50%
Aluminum Alloy	Iron Composite 70%
Carbon Fiber Composite	Iron Composite 70%

From Figure 55 the semivariogram for the stress that fits the bonded filled chevrons model the best is the Gaussian form. The Gaussian residual error is also the lowest for the given data from Table 17.

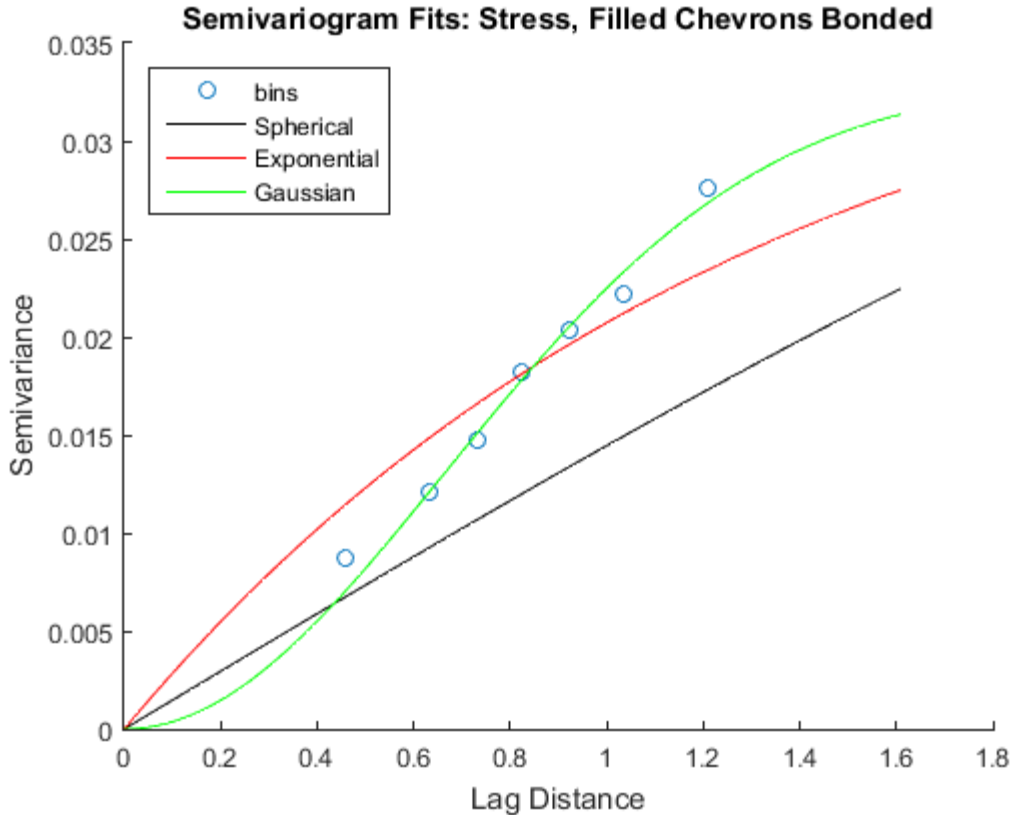


Figure 55: Semivariogram of stress fits: filled chevrons bonded model

Table 17: Semivariogram of stress characteristics: filled chevrons bonded model

Fit	Sill (c)	Range (a)	Residual Error
Spherical	0.039	2.6	1.32E-05
Exponential	0.039	3.97	3.75E-05
Gaussian	0.033	1.61	5.05E-06
<b>Number of Bins</b>		7	

From Figure 56 the semivariogram for the stress that fits the bonded filled chevrons model the best is the Gaussian form. The Gaussian residual error is also the lowest for the given data from Table 18.

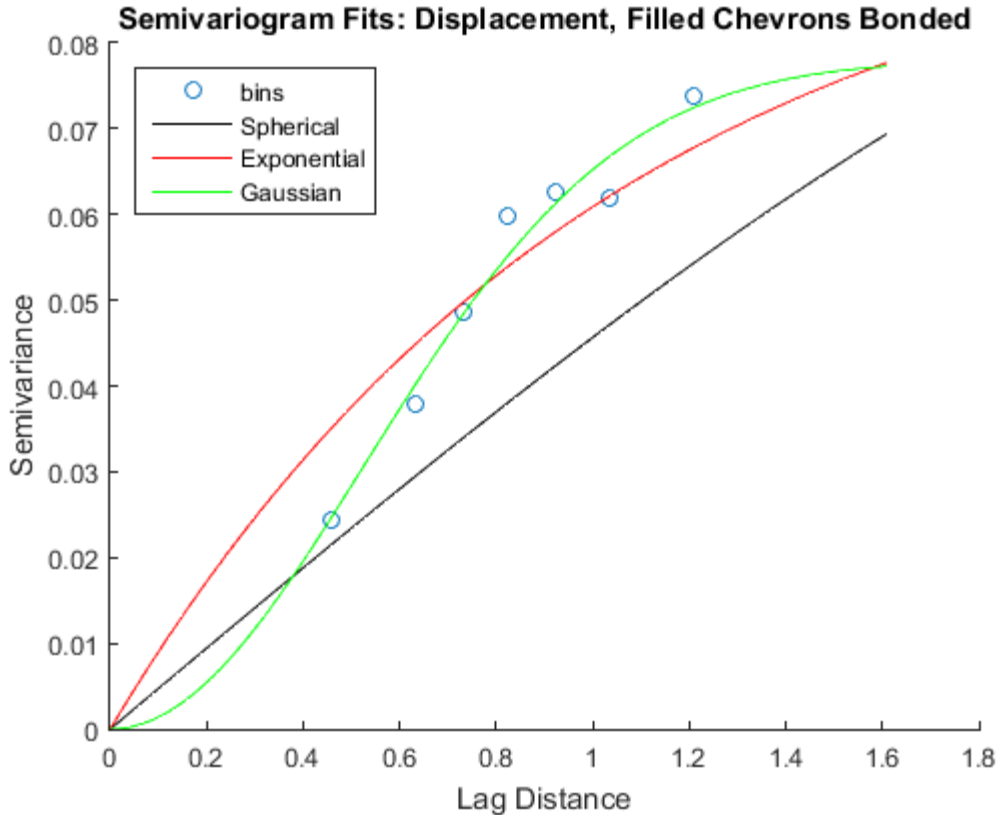


Figure 56: Semivariogram of displacement fits: filled chevrons bonded model

Table 18: Semivariogram of displacement characteristics: filled chevrons bonded model

Fit	Sill (c)	Range (a)	Residual Error
Spherical	0.099	2.19	1.23E-04
Exponential	0.099	3.14	2.60E-04
Gaussian	0.078	1.29	5.62E-05
<b>Number of Bins</b>		7	

#### 4.5 Localized Stress Model Conclusion

The configuration of the HSFESS has been discussed and the original model created by Kaschmitter was analyzed. Kaschmitter's model [12] maximizes the kinetic energy storage of the HSFESS's rotor while meeting constraints of geometry and stress in the rotor. The model has been expanded to include localized stress in regions of interest. Using the optimized dimensions from Kaschmitter's model, ranges of variables were determined to create rotor configurations. The rotor's geometry and material characteristics were adjusted in these

ranges to map the design space inside the given bounds. The design space was mapped by use of a semivariogram that relates special correlation of inputs and outputs. A stochastic prediction of maximum stress and displacement at the inner edge of the rotor are found with the use of ordinary Kriging utilizing the semivariogram fit with the lowest residual error. The dips in the displacement semivariograms are counter-intuitive. As the lag distance increases the semivariance becomes less as illustrated in Figure 52, Figure 54, and Figure 56. These dips are due to the multivariable problem and that the variables are a different scale. The different scales propagate the slight drop in semivariance with an increasing lag distance. Normalization of the variables helps reduce the instances, but there are no perfect normalization schemes for Kriging.

Three separate models were mapped in this chapter:

1. An empty chevron model that mimics the LSFESS
2. A model that has material in the chevrons and includes slipping effects. This model is created to map stress and displacement at the inner edge of the rotor with two separate materials
3. A model that has material in the chevrons that is bonded to the rotor material. This model is used to explore a carbon fiber composite as a more desirable material because of its high strength to weight ratio and ability to reduce the slipping created along material boundaries by bonding the materials together.

Each of the models has a map to make a stochastic prediction of the displacement at the inner edge of the salient pole, and the maximum stress seen in this section of the rotor. The predictions link geometry, material, and operating conditions to the outputs. The displacement is important to know to predict the airgap change between the stator and rotor. When the angular speed of the rotor increases, the airgap increases. It is vital from an electromagnetic perspective to know what the airgap is at a given speed. The FRRM makes corrections to the rotor based on its position. When a changing airgap is introduced, it is important to distinguish between changes in airgap and changes in position. It is important to quantify the stress concentrations in the rotor to predict failure based on geometry, material, and operating speeds.

The formulation of the three stochastic models started with a model 1. When this model was compared to model 2, under the same rotor configuration, the following trends were seen:

- The displacement along the inner edge of the salient pole is reduced in model 2 when the chevron material is relatively lighter than the rotor material
- A stronger chevron material further decreased radial displacement in model 2 along the inner edge of the salient pole
- A wider azimuthal chevron width further decreased radial displacement of model 2 along the inner edge of the salient pole
- A larger outer notch radius decreased the radial displacement in model 2 along the inner edge of the salient pole
- A larger stress in the rotor appeared in model 2 because of the reduction in the radial displacement of the inner edge of the salient pole.

The reduction in displacement and the increase in stress was expected. This is due to the geometry of the salient pole region. When a material is introduced into the chevron, it replaces the air. The air essentially has no elastic modulus, so the added material can reduce the displacement of the salient pole. The geometry and material of the chevron changes the effect this has. The higher the strength to weight ratio of the material, the greater effect on the salient pole's radial displacement. The larger the ratio of the chevron to rotor area had the most effect on displacement as well. Reducing the displacement does come at cost, as it increases the stress. With the semivariogram and the Kriging process, geometry, and materials can be explored in this configuration.

Quantifying the reduction in stress while maintaining reduction of the displacement is the purpose of model 3. When comparing model 2 to model 3, under the same configurations, the following trends were seen:

- The displacement along the inner edge of the salient pole is reduced in model 3 when the chevron is bonded to the rotor
- The maximum stress in the rotor is reduced in model 3 because of the bonding of the two materials.

The models in this chapter have found that filling the chevrons with a relatively lighter material than the rotor material decreases the displacement along the inner radius of the rotor. The stress is also decreased when the chevron and rotor are bonded together. This reduces slipping effects, such as shear between the two materials. Discontinuous randomly oriented composite materials are able to be bonded together, relatively light, and can be impregnated with iron.

## 5 Electromagnetic Rotor Model

Using the surrogate modeling techniques described in chapter 4, a model is created in the same manner to map electromagnetic characteristics of the Field Regulated Reluctance Machine (FRRM). The FRRM operates with the use of salient poles, Figure 41, and the effect of the saliency ratio can give the machine access to more torque in a given configuration. A larger amount of torque can rotate the same size rotor at a higher acceleration, or can rotate a larger rotor. This directly relates to the amount of energy that can be stored in the machine over a given amount of time.

In this chapter, the physical makeup of the HSFESS is electromagnetically examined. This chapter uses the electromagnetic model developed at the University of Idaho by Bridget T. Wimer [5]. Wimer's model was created for the LSFESS. The model uses fundamental elements of electromagnetic mathematics and validates the solutions with FEA software. A further extension of this model is created to map the design space using multiple geometries and materials. Experiments of estimating an unknown material's permeability is discussed to extend FEA modeling to a composite material. FEA software is used to construct a semivariogram to process desired outputs of torque and saturation for the HSFESS. The semivariogram will provide a stochastic prediction using a Kriging/Gaussian process.

### 5.1 FRRM Composition

The FRRM only contains electrical windings on the stator. The rotor does not contain any windings. In order for the stator to interact with the rotor, the rotor must be a magnetically permeable material [8]. Permeability is the ability of a material to support the formation of a magnetic field within itself. In a given medium, the magnetic flux density,  $\mathbf{B}$ , can be related to the magnetic field intensity,  $\mathbf{H}$ , with the permeability,  $\mu$  by [47]:

$$\mathbf{B} = \mu \mathbf{H} \quad 5.1$$

A higher permeability increases the flux density. However, higher permeable engineering materials, like iron, have a high density. From equations 4.1, 4.2, and 4.3, a higher density increases the stress and displacement for a rotating geometry. Being able to map the characteristics of a given rotor geometry and electrical material properties is advantageous to the electromagnetic dynamics of the FRRM.

The rotor is essentially a large electromagnet that is composed of magnetic poles. For the FRRM, the rotors poles are salient, meaning they protrude outward from the cylindrical surface of the rotor. The rotor's salient poles alter the distribution of flux around the machine. Saliency results in a different inductance for the pole and chevron regions [47]. The variables selected for the mechanical rotor design influence the saliency ratio of the machine.

The saliency ratio is the ratio of inductance of the direct axis and quadrature axis. The direct axis is in line with the center of a salient pole, and the quadrature axis is in line with the center of a chevron as shown in Figure 57. As the geometry and material of the rotor changes, the saliency ratio changes, influencing the torque of the machine. If the inductances of the direct axis and quadrature axis are the same, no torque is produced on the rotor.

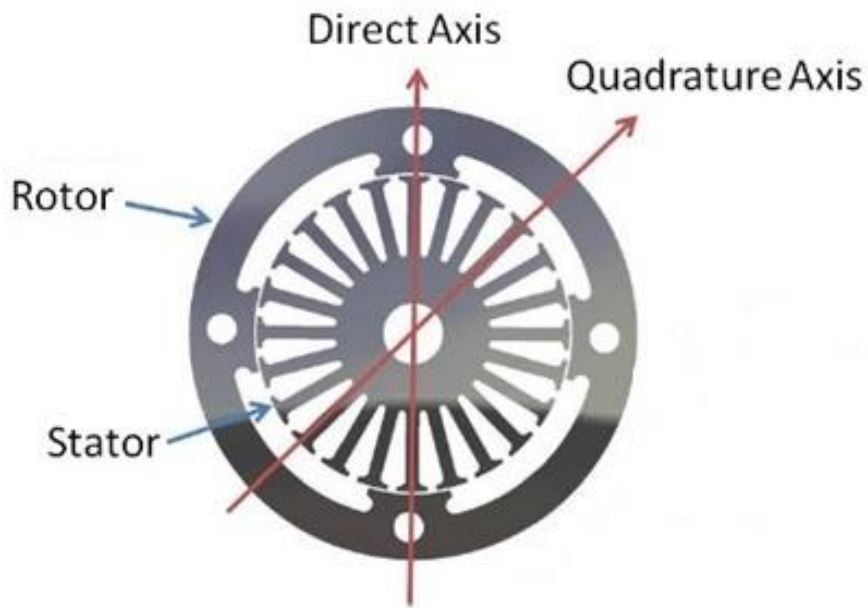


Figure 57: FRRM topology [5]

## 5.2 LSFESS Electromagnetic Model

To validate the magnetic circuit model (MCM) and modified winding approach (MWA) calculations of the FRRM, Wimer used a FEA program known as Finite Element Method Magnetics [48]. Wimer developed the MCM and MWA approaches at the University of Idaho in her M.S.E.E. thesis [5]. The two methods, MCM and MWA, result in a small error of 2% from each other when comparing the static forces of the LSFESS in Tesla. The MCM and MWA methods both assumed that the iron has infinite permeability and that there is no

magnetomotive force drop across the stator or rotor. The magnetomotive force is also known as the magnetic potential. Magnetomotive force is analogous to electromotive force, voltage, for electricity [47]. The FEA program is limited to calculating static forces for the FRRM.

An FEA software, FEMM, is used to calculate the resulting magnetic forces when the direct axis current is adjusted. The program is used to verify the flux density and forces of the stator. Wimer reported an FEMM force of approximately 20% lower than the MWA approach. This is due to the stator being saturated at this current level. Saturation is reached when an increase in applied external magnetic field,  $H$ , cannot increase the flux density,  $B$ , any further. The relationships of permeability, current, and geometry are of interest in development of the HSFESS electromagnetic model.

### **5.3 Magnetic Permeability Experiment**

The material characteristic needed for the FEA program is magnetic permeability. Permeability is the material property that is related to the magnetic flux density, equation 5.1. The iron-particle composite materials do not have the same permeability as iron itself because of the added volume fraction of matrix/carbon fiber. To experimentally measure the permeability, specimens need to be constructed out of different iron volume fractions. The only ferromagnetic material in the composite material discussed in chapter 3 is iron. Carbon fiber/matrix composites have a permeability close to air [49]. Only changing the amount of iron will affect the permeability of the composite.

Increasing the amount of iron in the electromagnetic composite specimens does not have a peak like the mechanics properties in Figure 25, but constantly increases. The shape of the graph is unknown, but the highest permeability is possible when there is 100% iron in the mixture. The only limiting factor to permeability is manufacturability. Specimens are constructed to the same volume fraction limit as the mechanics discussed in chapter 3, but the results are extrapolated with a curve fit discussed later in the chapter.

Specimens are constructed in an endless loop, known as a toroid core, shown in Figure 58.

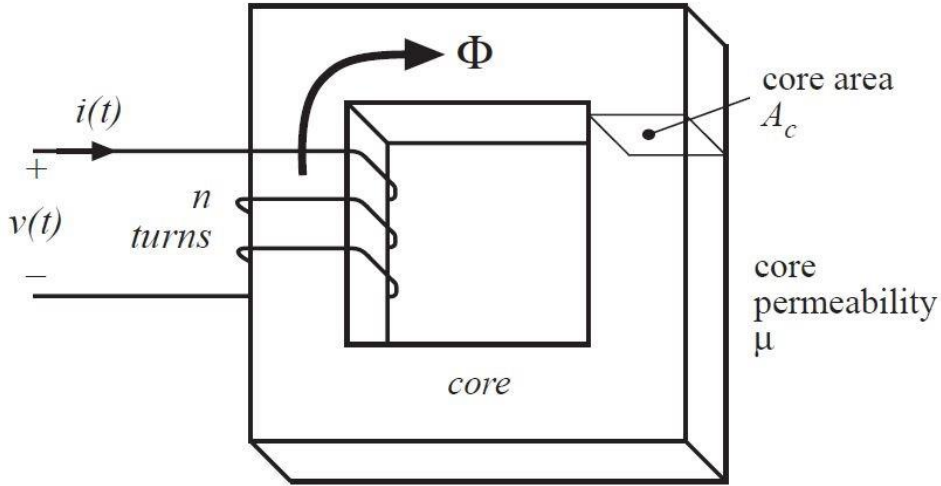


Figure 58: Toroid specimen [31]

Faraday's law of inductance is used with specimen geometry and set number of turns to find magnetic permeability of the unknown material [47]:

$$v = L \frac{di}{dt} \quad 5.2$$

$$L = \frac{\mu N^2 A_c}{2\pi r} \quad 5.3$$

where  $v$  is the applied voltage,  $I$  is the current,  $L$  is the inductance,  $\mu$  is the permeability of the material,  $N$  is the number of turns of the wire,  $A_c$  is the cross sectional area of the toroid, and  $r$  is the average radius of the toroid.

The simplest geometry to test, that has a constant averaged radius, is a short cylinder [49]. A female mold of this geometry is created to test different volume fractions of iron, carbon fiber, and matrix material. A toroid with a known permeability is first tested as a control to verify the experiment. Then four different configurations of composite volume fractions are constructed. The relative permeability of each material is tested and then a line is fit to the data to map untested volume fractions. The results of the experiment are shown in Table 19. A picture of the experimental set up is shown in Figure 59. A procedure of the toroid permeability test and specimen geometry are available in Appendix C: Toroid Permeability Test. A linear fit extrapolation of the permeability is shown in Figure 60. An equation to

relate the permeability to the percentage of iron in a given material is found with the data. The r-squared error is relatively small, as shown in Figure 60, and the results can be used in correlation with the FEA model.

**Table 19: Permeability experimental results**

Specimen	Carbon Fiber (%)	Matrix (%)	Iron (%)	Permeability (H/m)
1	20	75	5	1.20E-05
2	10	78	12	1.50E-05
3	25	60	15	1.65E-05
4	0	70	30	2.22E-05

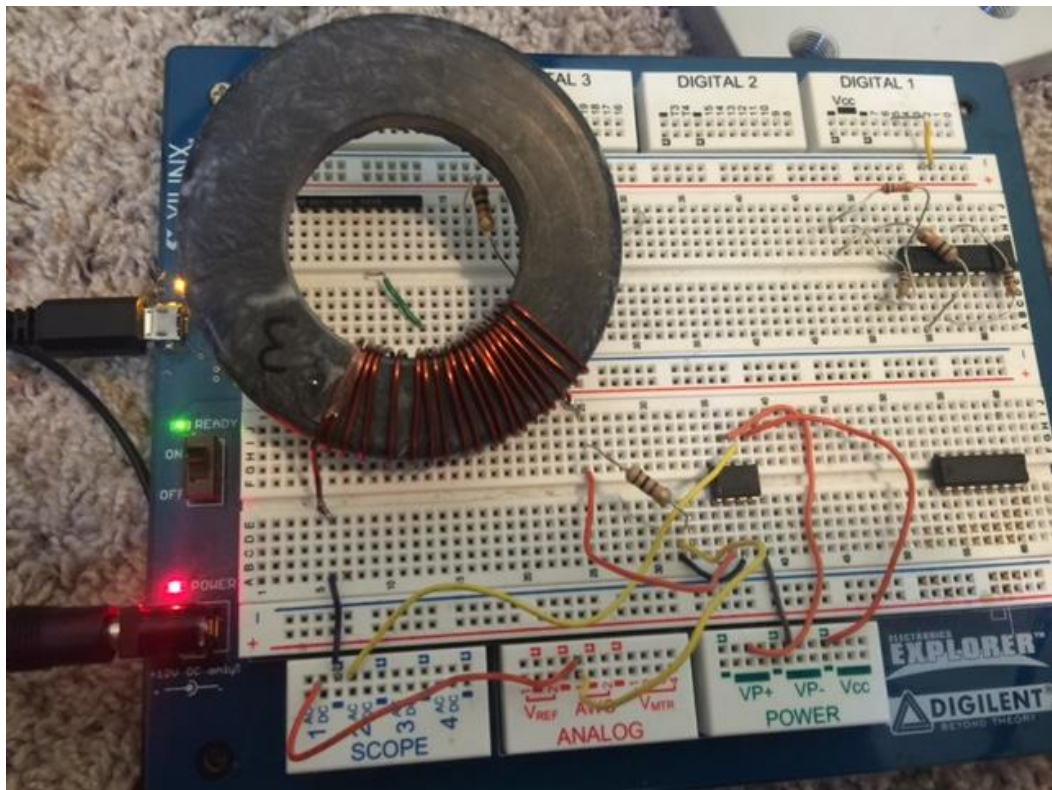


**Figure 59: Toroid test setup**

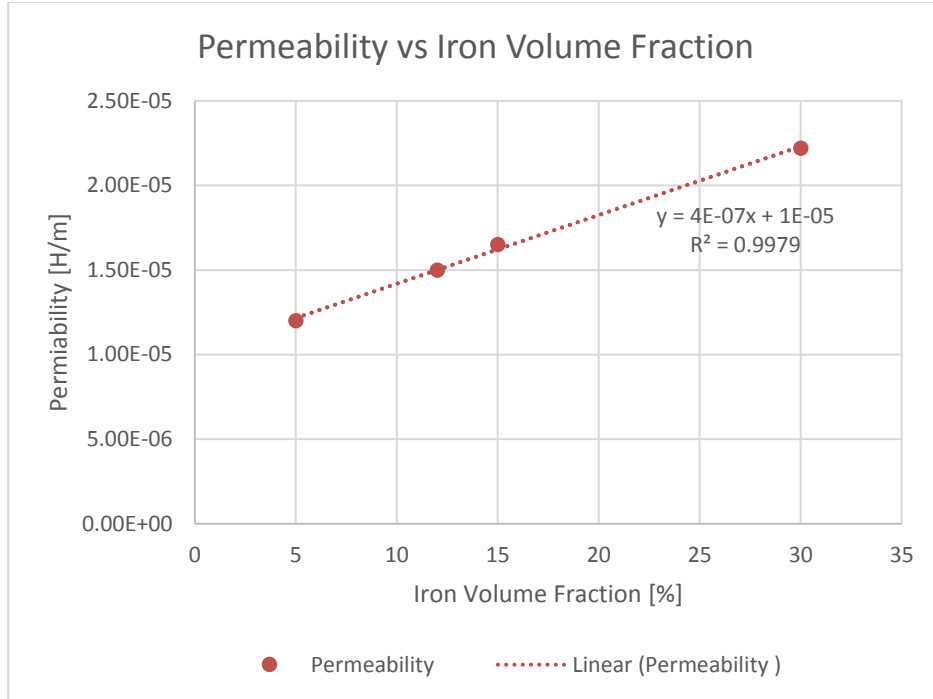


**Figure 60: Linear extrapolation of permeability data**

## 5.4 FEA Model Creation

Wimer's FEA simulation is recreated to indicate parameters and structure for the FEMM program [48]. Once the program operation is understood, geometry and material bounds are set to create model situations.

The design variables chosen to incorporate into the model are:

- $N_o$  is an outside notch radius. The notch radius is chosen as a variable because it forces the flux to be pushed into the salient pole area.
- $C_w$  is the width of the salient pole. A wider salient pole increases the cross sectional area.
- $R_i$  is the inside radius of the chevron. A larger inside radius increases the saliency ratio, which allows the stator to increase the torque on the rotor.
- $R_o$  is the outside radius of the rotor. This variable changes the area that the flux can pass through relative to the chevron radius.
- $i$  is the current that is passed through the windings in the stator. The current changes the flux created by the stator. The winding placement is shown in Figure 61.

- $\mu_r$  is the relative magnetic permeability of the rotor. The permeability has a direct relationship with the magnetic flux density.

The geometry constraints and input variable ranges are shown in Table 20. The ranges are chosen because they represent the physical operating constraints of the HSFESS.

**Table 20: FEMM constrains and input variable ranges**

$0 < R_o - R_i - 2N_o - N_i$	in
$0 < R_s \tan(C_w) - N_o$	in
$0.125 < N_o < 0.425$	in
$5 < C_w < 20$	deg
$3 < R_i < 4$	in
$3.6 < R_o < 4.6$	in
$1 < i < 5$	Amp
$30 < \mu_r < 2500$	dim

The output being collected is  $|\mathbf{B}|$  in Tesla. This output is the magnitude of the magnetic flux density. The magnitude of the flux density relates how much force the stator can apply to the rotor. To map how the chevron, rotor/stator airgap, rotor and stator magnitudes of magnetic flux density,  $|\mathbf{B}|$ , change as the input variables change, 10 geometries that operate at 2 different currents are chosen. Each one of these situations tests 3 separate materials. This creates 60 data points that are all physical and in the ranges described by Table 20. The materials being tested are shown in Table 21 along with their corresponding relative magnetic permeability. The output points are chosen because of their relationship with the saliency ratio, saturation, and inductance of the electromagnetic mechanics.

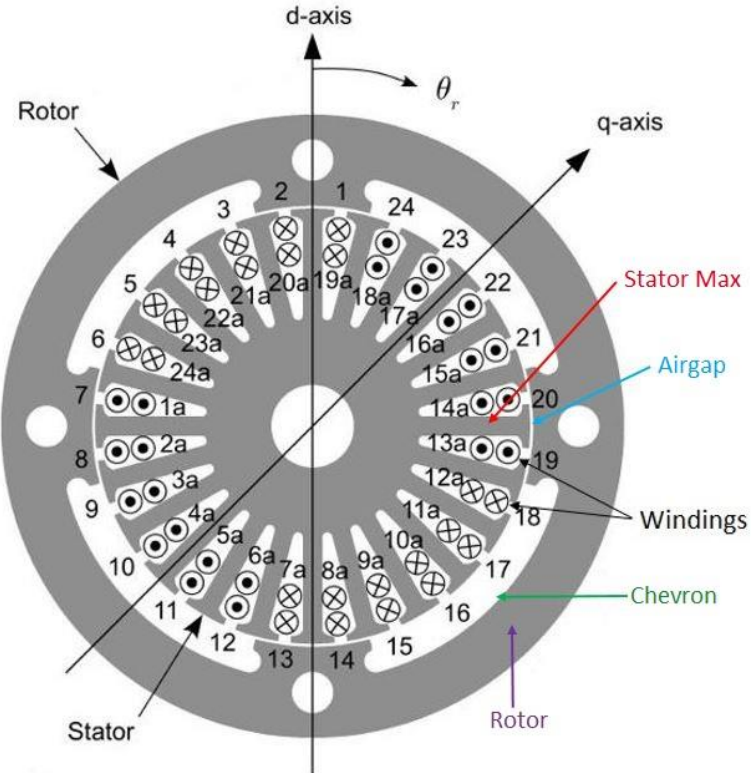


Figure 61: Stator winding topology [7]

Table 21: FEMM materials list

Material	Relative Permeability, $\mu_r$ [-]
Iron (98% pure)	2500
Martensitic SS, Annealed	800
Iron Composite 70%	30

## 5.5 Electromagnetic Stochastic Model

The Kriging/Gaussian process explained in chapter 4 is used to map electromagnetic design space. The data collect by the FEMM program is used to construct semivariogram to map chevron, rotor/stator airgap, rotor and stator magnitudes of magnetic flux density,  $|\mathbf{B}|$ , as the inputs in Table 20 and Table 21 change.

The chevron is the interpole region of the stator that is desired to have a very low permeability. The low permeable area forces the flux to go from a positively charge salient

pole, to a negatively charged salient pole [47]. The region is required to have a low flux density so the stator can spin the rotor efficiently. If a high flux density is in this region, unwanted flux is moving through this area and is not being concentrated at the salient pole regions to help spin the rotor. Chevron region magnitudes of magnetic flux density,  $|\mathbf{B}|$ , are used to create a semivariogram based on the inputs of chapter 5.4. The semivariogram is shown in Figure 62. The residual error is shown with each fit in Table 22, which imposes the use of a Gaussian fit for the  $|\mathbf{B}|$  in the chevron.

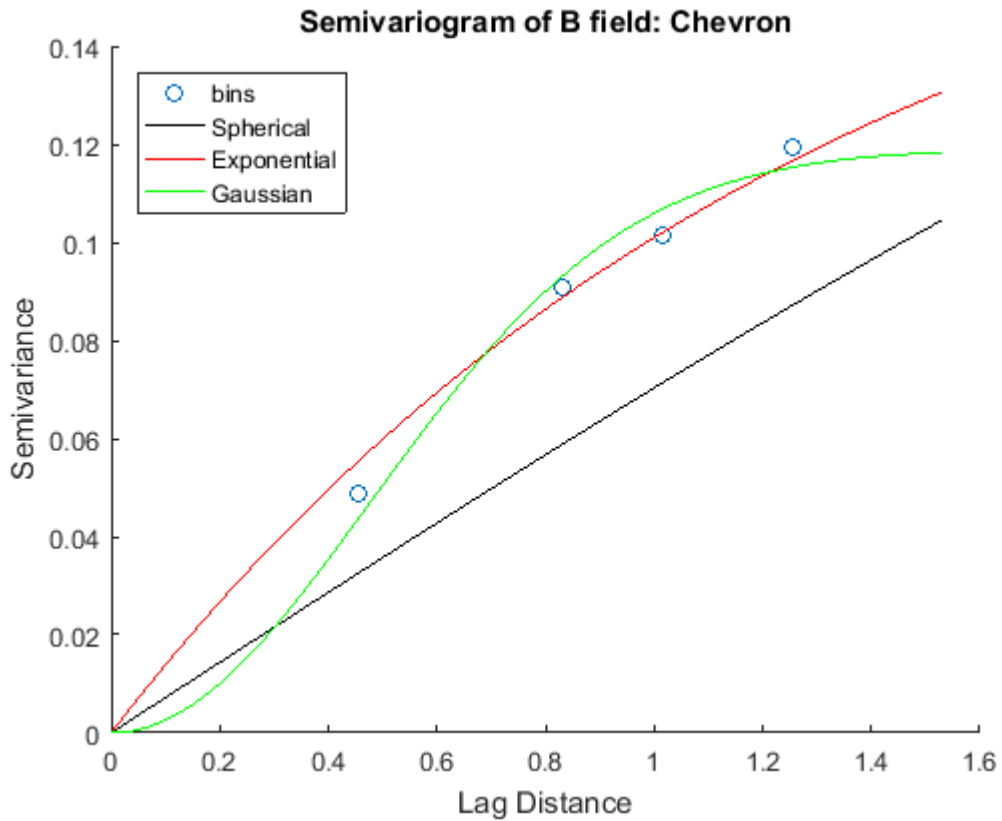


Figure 62: Semivariogram of chevron  $B$  field

Table 22: Semivariogram characteristics of chevron  $B$  field

Fit	Sill (c)	Range (a)	Residual Error
Spherical	0.134	1.76	7.71E-05
Exponential	0.191	3.99	5.55E-05
Gaussian	0.119	1.17	1.58E-05
Number of Bins		4	

The rotor/stator airgap has the highest reluctance of the magnetic flux path in the FRRM. The airgap is where the magnitude of the magnetic flux density,  $|B|$ , is converted into a torque that spins the rotor around the stator. Airgap region magnitudes of magnetic flux density,  $|B|$ , are used to create a semivariogram based on the inputs of chapter 5.4. The semivariogram is shown in Figure 63. The residual error is shown with each fit in Table 23, which imposes the use of a Gaussian fit for the  $|B|$  in the rotor/stator airgap.

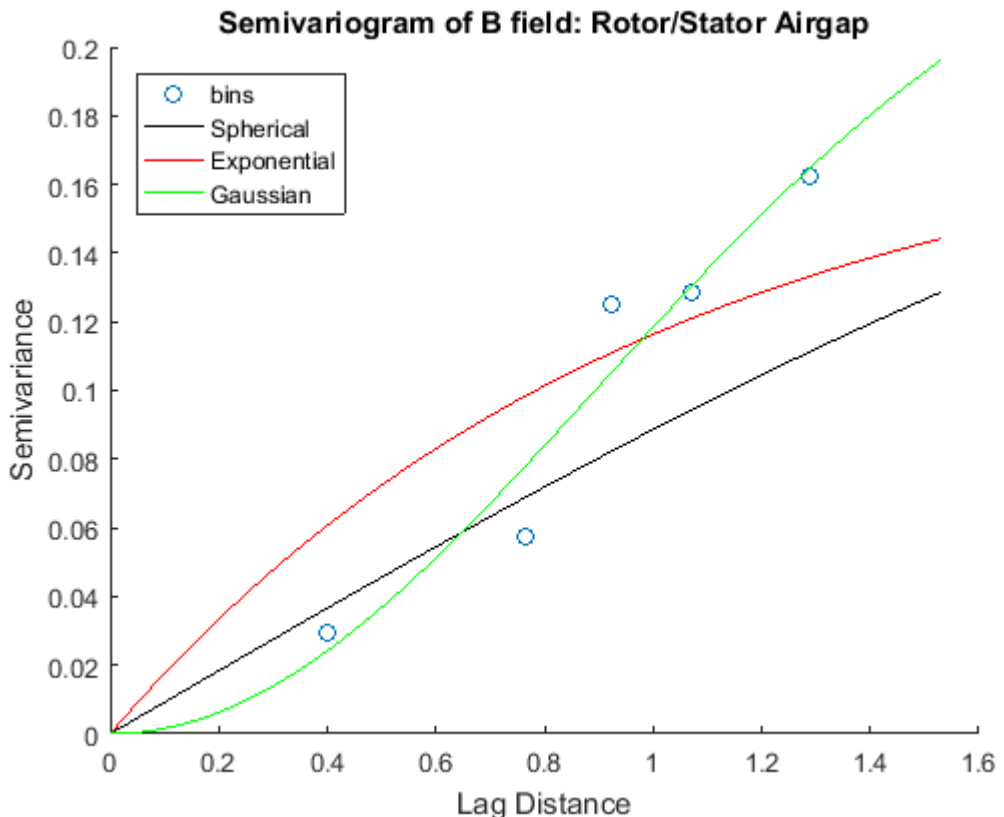


Figure 63: Semivariogram of rotor/stator airgap  $B$  field

Table 23: Semivariogram characteristics of rotor/stator airgap  $B$  field

Fit	Sill (c)	Range (a)	Residual Error
Spherical	0.244	2.99	2.00E-03
Exponential	0.184	2.99	3.80E-03
Gaussian	0.256	2.2	8.47E-04
<b>Number of Bins</b>		5	

If the rotor is carrying a higher flux density, compared to the airgap, then there is more torque applied to the rotor by the stator. Collecting the magnitude of magnetic flux density,  $|\mathbf{B}|$ , in this region will also provide information about rotor saturation. Rotor region magnitudes of magnetic flux density,  $|\mathbf{B}|$ , are used to create a semivariogram based on the inputs of chapter 5.4. The semivariogram is shown in Figure 64. The residual error is shown with each fit in Table 24, which imposes the use of a Gaussian fit for the  $|\mathbf{B}|$  in the rotor.

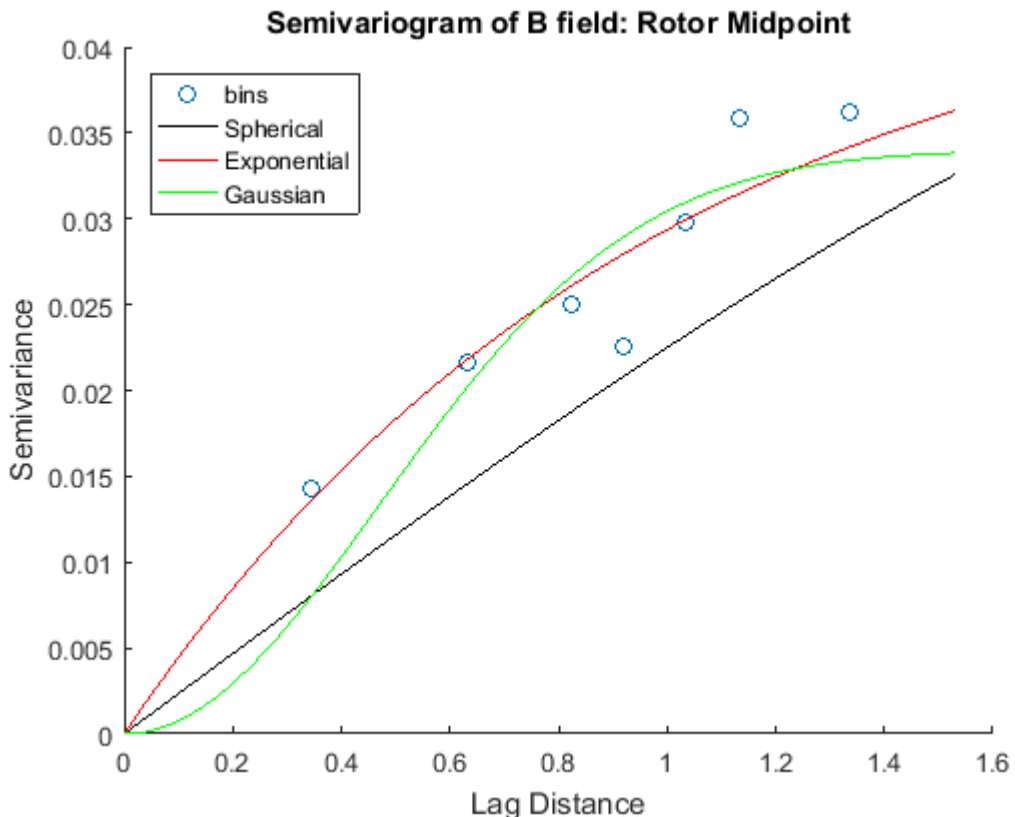


Figure 64: Semivariogram of rotor midpoint  $B$  field

Table 24: Semivariogram characteristics of rotor midpoint  $B$  field

Fit	Sill (c)	Range (a)	Residual Error
Spherical	0.04	1.82	5.07E-05
Exponential	0.046	2.95	5.45E-05
Gaussian	0.034	1.15	3.10E-05
<b>Number of Bins</b>		7	

The electrical current is generated in the stator. In a given configuration, the stator will saturate first, as there is nothing between it and the windings. Therefore, the magnitude of magnetic flux density,  $|B|$ , is collected in this region so saturation can be determined in a given material. The flux density magnitudes in this region are used to create a semivariogram based on the inputs of chapter 5.4. The semivariogram is shown in Figure 65. The residual error is shown with each fit in Table 25, which imposes the use of a Gaussian fit for the  $|B|$  in the stator.

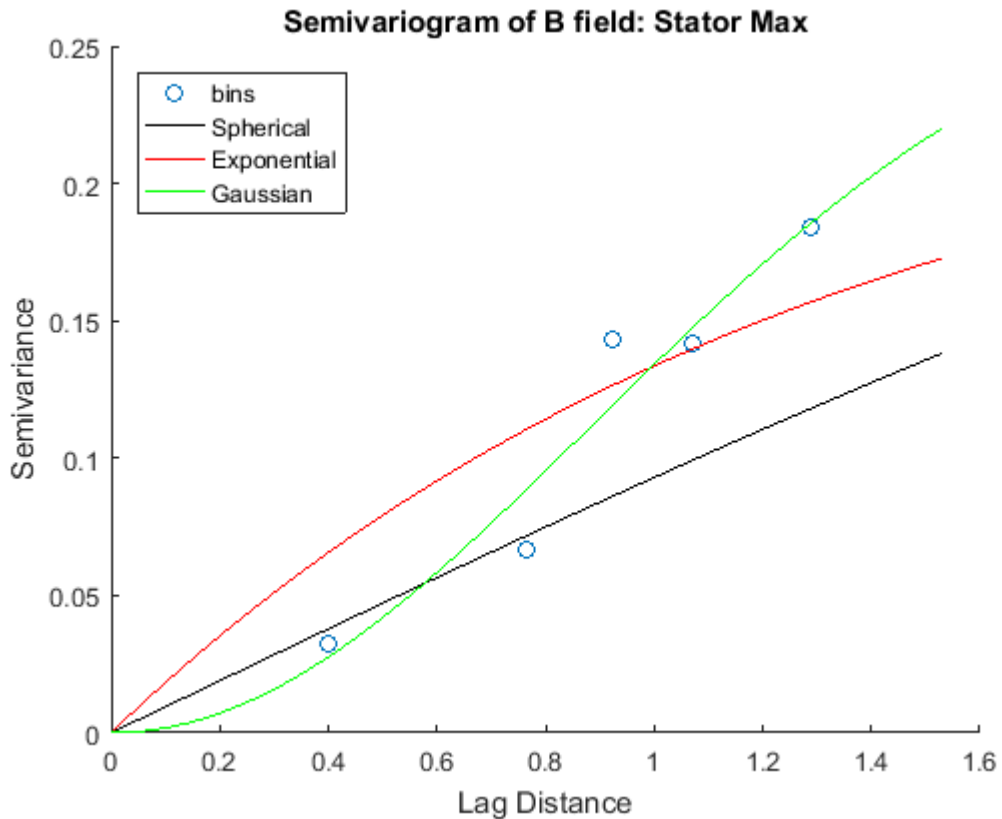


Figure 65: Semivariogram of stator maximum  $B$  field

Table 25: Semivariogram characteristics of stator maximum  $B$  field

Fit	Sill (c)	Range (a)	Residual Error
Spherical	0.298	3.26	2.50E-03
Exponential	0.253	3.99	4.00E-03
Gaussian	0.283	2.16	1.10E-03
Number of Bins		5	

## 5.6 Electromagnetic Rotor Model Conclusion

This chapter used the electromagnetic model for the LSFESS developed by Bridget T. Wimer to extend the model to different parameters of interest for the HSFESS. The use of FEA software, FEMM [48], was used to explore electromagnetic static inputs. Using the optimized dimensions from Kaschmitter's model, geometric ranges of variables were determined to create rotor configurations. Using the parameters from Wimer's model, electromagnetic inputs and properties were varied to explore design regions of interest. The design space was mapped by use of a semivariogram that relates spatial correlation of inputs and outputs. A prediction of chevron, rotor/stator airgap, rotor and stator magnitudes of magnetic flux density,  $|\mathbf{B}|$ , were found with the use of ordinary Kriging utilizing the semivariogram fit with the lowest residual error. The semivariogram provides a stochastic prediction using a Kriging/Gaussian process. This model was used to explore the effects of magnetic flux density in an inside-out flywheel configuration with different geometries and material characteristics.

As material of this section of the flywheel changes, the mechanics of the electromagnetics alter. The variation was dependent on the mechanical permeability of the material, the geometry of the rotor, and operating amperage of the FRRM. Categorizing the effects and predicting untested design space is now possible with the use of the Kriging process. There are a smaller number of bins used to create the semivariogram for the electromagnetic model when comparing to the mechanical model. There were more data points collected for the mechanical model so the semivariogram has a larger number of bins to accommodate the larger number of data points. The model allows testing of different geometries, material characteristics, and operating amperage to quantify the magnetic flux density effects in different regions of the FESS. Quantifying the effects allows a stochastic prediction of the torque, produced by the stator, to spin the flywheel. The kriging process also predicts a saturation level of the stator and rotor so that operation can stay in an efficient region. The magnetic losses, due to different configurations, were quantified by studying the  $|\mathbf{B}|$  field in the chevron airgap.

The following trends were seen when analyzing input to configurations for the electromagnetic model:

- As the area between the outside radius and chevron radius decreased the rotor  $|\mathbf{B}|$  field increased
- As the area between the outside radius and chevron radius decreased the rotor/stator airgap  $|\mathbf{B}|$  field decreased

The amperage and permeability show the greatest effect on the  $|\mathbf{B}|$  field in the rotor. Other parameters do affect the  $|\mathbf{B}|$  field, such as saturation of the material or permeable material area that the  $|\mathbf{B}|$  field travels through. The design space is non-linear, but the Kriging model does provide an estimation of  $|\mathbf{B}|$  field in each region based on specified inputs.

## 6 Summary and Future Work

### 6.1 Summary

A team of electrical computer engineers, mechanical engineers and physicists work together to accomplish NASA's goal of developing an energy dense, reliable, and efficient energy storage system. Designing an integrated, hubless high-speed flywheel energy storage system (HSFESS) is the goal of the University of Idaho's NASA flywheel team.

Mechanical energy stored in a flywheel energy storage system (FESS) increases exponentially with the speed, and only linearly with the moment of inertia, equation 1.1, making it more advantageous to increase the speed of the flywheel. A flywheel in an inside-out configuration, essentially a cylinder. Stresses in a rotating cylinder exponentially increase with the rotational speed of the spinning object and linearly with the density of the material, equations 4.1 and 4.2. The displacement follows the same trend, but is inversely proportional to the elastic modulus of the material. These reasons make a high strength to weight material beneficial for maximizing energy storage of a FESS. Composites are high strength to weight ratio materials.

In a FESS operated by a field regulated reluctance machine (FRRM) requires the use of a magnetically permeable rotor. Composites can be tailored to enable magnetic permeability. A permeable material can be impregnated into a composite material. The composite type is assessed as an isotropic material because of the discontinuous randomly oriented mechanics discussed in chapter 2. The mechanics of the isotropic composite material can be estimated with the use of equations to predict the elastic modulus, Poisson's ratio and strength with the use of equations 2.6, 2.7, 2.28, and 2.29. Different compositions of permeable particulates, chopped fibers, and matrix materials predict different mechanics. The mechanics are heavily dependent on material characteristics of the matrix, as it enables the load to be transferred to each of the different reinforcements inside of the composite. With the understanding of more precise manufacturing equipment, results from chapter 3 signify that the composite mechanic predictions are acceptable to perform design.

Geometry of the rotor allows the stator to increase torque production of the FRRM. The geometry introduces stress concentration due to the need to increase the saliency ratio of the

rotor. The entire rotor does not need to be a permeable material, which points to encompassing the permeable material in a higher strength carbon fiber filament composite. The wrapping provides a much higher strength than the discontinuous chopped composite because of the orientation of the fibers. When fibers are oriented in one direction, the strength is greatly increased. This type of composite is only used to support the permeable material, as it cannot be formed into the complex shape required to interact with the FRRM. The chopped fiber composite does not have the strength of the aligned carbon fiber, so stress analysis is only performed on the discontinuous composite structure. Displacement at the inside edge of the rotor is an important aspect, because a larger airgap from stresses imposed on the flywheel increases the distance to flux must travel from the stator to the rotor.

Geometry of the permeable section of the rotor was explored to quantify the maximum stress in this section of the rotor. The jagged geometry of the rotor induces stress concentrations, which increases the localized stress field. The complex shape of the rotor also increases the displacement of the inner edge of the rotor, resulting in an exponential change in the electromagnetic dynamics. Material also contributes to the stress field and displacement of the material. Because of its high strength to weight ratio, a composite material is more advantageous from a mechanical standpoint, but a more permeable material, such as iron, is more advantageous from an electromagnetic standpoint.

A design that maximizes kinetic energy stored by the flywheel is the overall goal of the NASA project. The effects of different materials, designs, and operating conditions need to be explored to locate the design variables that are important to complete the overall design. The forces induced on the rotor during high speed operation are a significant limiting factor of the HSFESS design. Since the design space encompassing all the parameters that control geometry, material, and operating conditions is so non-linear, an analytical solution is problematic. A similar problem arises with the magnemotive force needed to rotate the rotor.

Numerical simulation was used to merit this problems with the use of FEA. FEA simulates set inputs to quantify specified outputs of maximum stress, displacement along the inner edge of the salient pole, and magnetic flux density at various points in the FESS. The quantified outputs are produced at many different operating inputs. The spaces in between the design points are categorized with the use of a semivariogram that relates special correlations of

design inputs to outputs. A Kriging/Gaussian process is used to estimate unknown territory of the design space to provide a prediction and uncertainty associated with that prediction.

## 6.2 Future Work

The maps created for the mechanical and electromagnetic models are a guide to help future processes. The models are only estimated predictions, but the interaction between the mechanical and electromagnetic needs of the HSFESS are the primary focus for the stochastic models. Future findings will require the need of one of the mechanical models. An M.S.E.E University of Idaho student, David Arnett, is researching the electromagnetic effects of the changing rotor/stator airgap. Arnett's findings will further refine the design space mapped in this thesis. One of the mechanical designs will be chosen, that surrogate model can estimate the stress and deformation of the rotor in different configurations. A permeability and airgap relationship will also be found with Arnett's model. An electromagnetic efficiency will prescribe an amperage/permeability interaction. This enables the electromagnetic surrogate model, created in this thesis, to estimate static torque production of the flywheel in different configurations.

The mechanical model selected also predicts change in the radial deformation vs speed of the flywheel. The prediction can be estimated for different configurations of rotor designs. The estimations allow the control system of the flywheel to distinguish between radial displacements and off axis movements. This allows examination of different flywheel control schemes as the airgap changes.

Once future models are created for needed design spaces, constraints can be set in place for operational bounds. After needed constraints of the system are found, the models created here will help accelerate optimization the HSFESS geometry. The models will assist in locating geometries that work better than others, both mechanically and electromagnetically. In these areas, a more refined model can be created once permeable material and airgap dynamics are electromagnetically analyzed.

Any material under the stress imposed by a high speed rotating object is going to experience displacement. The displacement of materials is highly dependent on shape and mechanical characteristics. To advantageously optimize material and actual geometry of the flywheel,

within bounds and the goal to maximize kinetic energy storage, the electromagnetic importance of the displacement must be quantified. Displacement limits will allow bounds to be set to optimize geometry and material to be determined.

A future goal of the HSFESS is to create a mechanical and electromagnetic dynamic model. As the airgap changes, the moment of inertia will also change. A modeling process, similar to the process presented in this thesis, can be used to examine the change. Once a geometry and material selection is more refined, FEA data points can be taken for the moment of inertia at a few different operating speeds. A Kriging/Gaussian process can be used to interpolate in between the selected data points. The changing moment of inertia data can be used in the mechanical dynamic model. The same FEA tests can also map more precise displacements of the rotor to be incorporated into the electromagnetic dynamic model.

An overall FEA simulation will need to be used in the future to analyze Poisson's ratio effects in the z direction. Poisson's ratio can be a significant contributor to the overall displacement of the flywheel. The structure holding the magnets in place will also have to be incorporated into the FEA analysis. The magnets are a strong, brittle material that are placed radially on the bottom of the flywheel. The radial placement of the magnets can be changed to help reduce the stress enforced on them and their encompassing material, but the placement influences the dynamics of the system. The magnets will also be radially displacing, so larger superconductors might be necessary to comply with the displacement. A composite material may also be used to encase the magnets to replace the current stainless steel caps used on the LSFESS.

## References

- [1] D. D. R. Williams, "Moon Fact Sheet," NASA, 25 February 2016 . [Online]. Available: <http://nssdc.gsfc.nasa.gov/planetary/factsheet/moonfact.html>. [Accessed 20 March 2017].
- [2] H. Chen, "Progress in electrical energy storage systems: a critical review," *Progress in Natural Science*, vol. 3, no. 19, pp. 291-312, 2009.
- [3] H. B. B. Bolund, "Flywheel Energy and power storage systems," *Renew. Sustain. Energy Rev.*, no. 2, pp. 235-258, 2007.
- [4] G. Roe, "Boeing flywheel energy storage technology," 2012.
- [5] B. Wimer, "Dynamic Modeling and Design of an Intergrated Flywheel Energy Storage System," University of Idaho, 2014.
- [6] J. G. Bitterly, "Flywheel technology past, present and 21st century projections," in *Energy Conversion Engineering Conference*, 1997.
- [7] B. Kisling, "Active Magnetic Bearing Control for an Experimental Flywheel Energy Storage System," University of Idaho, 2014.
- [8] J. Law, "Modeling of Field Regulated Reluctance Machines," University of Wisconsin-Madison, 1991.
- [9] G. Sotelo, A. Ferreira and R. d. Andrade, "Halbach array superconducting magnetic bearing for a flywheel energy storage system," *IEE transactions on applied superconductivity*, vol. 15, no. 2, pp. 2253-2256, 2005.
- [10] S. S. Tinchev, *Enhanced superconductivity of YBCO interfaces: origin of high critical temperature in layered superconductors*, pp. 1-13: Nature, 2009.

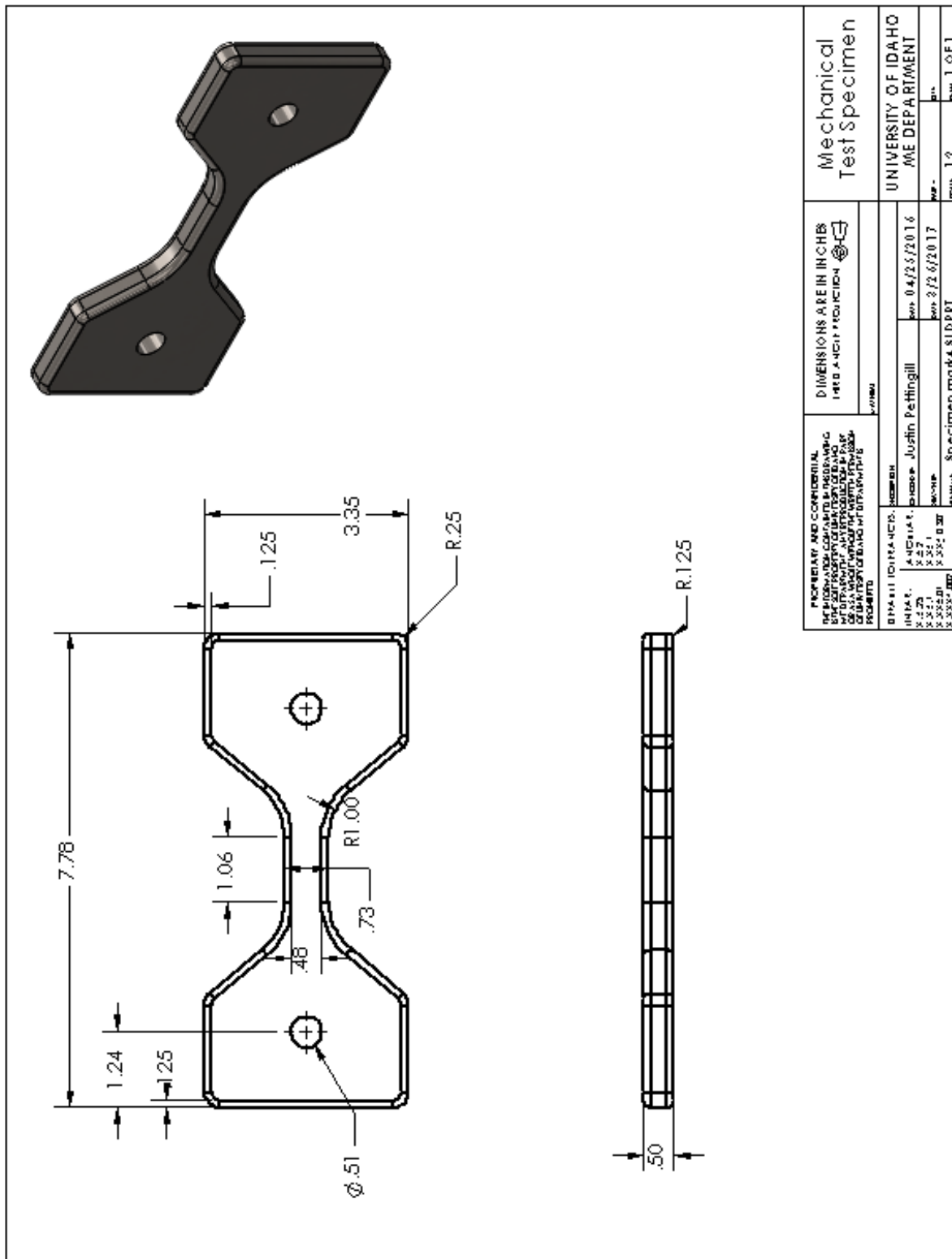
- [11] N. Igarashi and e. al, "Pure Iron based soft magnetic composite core that enables downsizing automotive reactors," *SEI Technical Review*, no. 80, pp. 98-103, 2015.
- [12] B. F. Kaschmitter, "Modeling, Design, and Optimization of a High-Speed Flywheel for an Energy Storage System," University of Idaho, 2016.
- [13] K. Ramus, "Power Electronic Components and Hardware for an Experimental Flywheel Energy Storage System," University of Idaho, 2014.
- [14] R. F. Gibson, Principles of Composite Material Mechanics, Third Edition, Boca Raton: CRC Press, 2012.
- [15] J. Vargas, J. Bariola, M. Blondet and P. K. Mehta, "Seismic strength of adobe masonry," *Materials and Structures*, vol. 19, no. 4, pp. 253-258, 1986.
- [16] A. Dollinger, "House and Garden," Ancient Egyptian Accomidations, March 2014.  
[Online]. Available: <http://www.reshafim.org.il/ad/egypt/timelines/topics/housing.htm>.  
[Accessed January 2017].
- [17] A. A. Griffith, "The Phenomena of Rupture and Flow in Solids," *Philosophical Transactions of the Royal Society*, vol. 221, no. A, pp. 163-198, 1920.
- [18] N. Pan, "The Elastic Constants of Randomly Oriented Fiber Composites: A New Approach to Prediction," *Science and Engineering of Composite Materials*, vol. 5, no. 2, pp. 63-72, 1992.
- [19] C. Gelinas and F. C. a. S. Pelletier, "Development of an Iron-Resin Composite Material for Soft Magnetic Applicaitons," Industrial Material Institute and Quebec Metal Powders Limited, Boucherville, 2000.
- [20] L. E. Nielsen and P. Chen, "Young's modulus of composites filled with randomly oriented fibers," *Journal of Materials*, vol. 3, no. 2, pp. 352-358, 1968.

- [21] Y. Lu, "Mechanical Properties of Random Discontinuous Fiber Composites Manufactured from a Wetlay Process," Virginia Polytechnic Institute and State University, 2002.
- [22] D. G. Lee and N. P. Suh, Axiomatic Design and Fabrication of Composite Structures, New York: Oxford University Press, 2006.
- [23] S. Banerjee and V. Sankar, "Mechanical Properties of Hybrid Composites using Finite Element Method Based Micromechanics," University of Florida, 2010.
- [24] S. W. Tsai and N. J. Pagano, "Invariant properties of composite materials," Technomic Publishing Co., Lancaster, 1968.
- [25] M. Manera, "Elastic properties of randomly oriented short fiber-glass composites," *Journal of Composite Materials*, vol. 11, pp. 235-247, 1977.
- [26] J. K. Lees, "A Study of Tensile Strength of Short Fiber Reinforced Plastics," *Polymer Engineering and Science*, vol. 8, no. 3, pp. 195-201, 1968.
- [27] P. E. Chen, "Strength Properties of Discontinuous Fiber Composites: I. Fiber Reinforced Composites," *Polymer Engineering and Science*, vol. 18, no. 6, pp. 496-504, 1971.
- [28] J. R. Davis, Tensile Testing, Materials Park: ASM International, 2004.
- [29] M. Biron, Thermosets and Composites, Second Edition, Elsevier Ltd, 2014.
- [30] B. Gomero, "Latin Hypercube Sampling and Partial Rank Correlation Coefficient Analysis Applied to an Optimal Control Problem," University of Tennessee, Knoxville, 2012.
- [31] A. P. Boresi and R. J. Schmidt, Advanced Mechanics of Materials, Sixth Edition, Hoboken: John Wiley & Sons, Inc, 2003.
- [32] J. E. Shigley and C. R. Mischke, Mechanical Engineering Design, McGraw-Hill, 1989.

- [33] Micro-Measurements, *MR-Series Bridge Completion Modules*, Vishay Precison Group, Inc., 2014.
- [34] D. M. Stefanescu, Handbook of Force Transduces, Berlin: Springer, 2011.
- [35] C. C. Chamis and R. F. Lark, "Hybrid composites - State-of-the-art review: Analysis design, application and fabrication.," in *Conference on Structures, Structural Dynamics and Materials*, San Diego, 1977.
- [36] R. Matsuzaki and e. al, "Three dimentional printing of continuous-fiber composites by in-nozzle impregnation," *Sci. Rep.*, vol. 6, no. 23058, p. 10.1038/srep23058, 2016.
- [37] S. Pelletier, C. Gelimas and F. Chagnon, "Effect of Compaction Temperature on magnetic properties of iron-resin composites," Industiral Materials Institute/National Research Counsil Canada, Boucherville, Quebec.
- [38] H.-I. S. K. Ha, Yang and D.-J. Kim, "Optimal design of a hybrid composite flywheel with a permenent magnet rotor," *Journal of Composite Materials*, vol. 33, no. 16, pp. 1544-1575, 1999.
- [39] E. J. Hearn, Mechanicsl of Materials 2: The Mechanics of Elastic and Plastic Deformation of Solids and Structural Materials, 3rd Edition, Butterworth-Heinemann, 1997.
- [40] J. D. Law, A. Chertok and T. A. Lipo, "Design and performance of a field regulated reluctance machine," *IEEE Transactions on Industry Applications*, vol. 30, no. 5, pp. 1185-1192, 1994.
- [41] S. J. Chapman, Electric Machinery Fundamentals, 4th edition, New York: McGraw-Hill, 2005.
- [42] O. C. Zienkiewicz, R. L. Taylor and D. Fox, The Finite Element Method for Solid and Structural Mechanics, 7th edition, Waltham: Butterworth-Heinemann, 2014.

- [43] W. A. Pruett and R. L. Hester, "The creation of surrogate models for fast estimation of complex model outcomes," *PLoS ONE*, vol. 11, no. 6, 2016.
- [44] H. Wackernagel, Multivariate Geostatistics, Berlin: Springer Berlin Heidelberg, 1998.
- [45] J.-P. Chiles and P. Delfiner, Geostatistics: Modeling Spacial Uncertainty, 2nd edition, John Wiley & Sons, Inc., 2012.
- [46] X. Jian, R. A. Olea and Y.-S. Yu, "Semivariogram modeling by weighted least squares," *Computers & Geosciences*, vol. 32, no. 3, pp. 387- 397, 2006.
- [47] M. N. O. Sadiku, Elements of Electromagnetics, New York: Oxford University Press, 2015.
- [48] D. Meeker, *Finite Element Method Magnetics*, 2011.
- [49] V. Antonucci, M. Esposito, M. R. Ricciardi, M. Z. M. Raffone and M. Giordano, "Permeability characterization of stiched carbon fiber preforms by optic sensors," *eXPRESS Polymer Letters*, vol. 5, no. 12, pp. 1075-1084, 2011.

## **Appendix A: Mechanical Testing Information**





## 1/4" Chopped Graphite Fibers

Part # - 571

These precision chopped graphite fibers offer an economical alternative for localized reinforcement of high performance parts requiring optimal electrical conductivity, high strength and modulus. Excellent for reducing voids in difficult vacuum bagging applications. Spread the filler in deep cavities or sharp edges of parts and be assured the pressure will squeeze out air.

### Features & Benefits:

- Good process ability
- Compatible with our System 2000 Epoxy Resin
- Good translation of mechanical and electrical properties
- Easily mixed into a uniform pre-blend prior to compounding

### Mixing Directions:

To mix, use 1 part #571 to 15 parts epoxy resin. This ratio may be adjusted as needed

### Storage:

Storage in a dry warehouse is recommended. Open packages should be resealed to prevent contamination of the product or discarded.

### Safety & Handling:

#571 1/4" Chopped Graphite Fibers contain ingredients which could be harmful if mishandled. Contact with skin and eyes should be avoided and necessary protective equipment and clothing should be worn. Individuals should wash with soap and water before eating, drinking, or using toilet facilities. Individuals should observe conditions of good industrial hygiene and safe working practice. For more detailed instructions on handling please see the MSDS sheet.

Pre-Chop Properties	
Property	Unit
Tensile Strength	660 ksi
Tensile Modulus <sup>(1)</sup>	34.1 Msi
Elongation <sup>(1)</sup>	1.90%
Size Level	1.00%
Yield (w/size)	317 yd/lb
Density	0.066 lb/in <sup>3</sup>
Filament Diameter	0.28 x 10 <sup>-3</sup> in

Notes: (1) Modulus / Elongation based on JIS R7601 (strain range of 0.4-0.6%) unless otherwise noted.

Information present herein has been compiled from sources considered to be dependable and is accurate and reliable to the best of our knowledge and belief but is not guaranteed to be so. Nothing herein is to be construed as recommending any practice or any product violation of any patent or in violation of any law or regulation. It is the user's responsibility to determine for himself the suitability of any material for a specific purpose and to adopt such safety precautions as may be necessary. We make no warranty as to the results to be obtained in using any material and, since conditions of use are not under our control, we must necessarily disclaim all liability with respect to the use of any material supplied by us.

©Copyright 2010 Fibre Glast Development Corporation

Fibre Glast Developments Corporation  
385 Carr Drive  
Brookville, Ohio 45309  
Phone – 800.214.8579  
Fax – 937.833.6555  
www.fibreglast.com



PDCT-PDS-00123-B-09/10-CG

Page 1 of 1

**SIGMA-ALDRICH**[sigma-aldrich.com](http://sigma-aldrich.com)**SAFETY DATA SHEET**

Version 3.8

Revision Date 05/24/2016

Print Date 05/28/2016

**1. PRODUCT AND COMPANY IDENTIFICATION****1.1 Product identifiers**

Product name : Iron

Product Number : 209309

Brand : Aldrich

CAS-No. : 7439-89-6

**1.2 Relevant identified uses of the substance or mixture and uses advised against**

Identified uses : Laboratory chemicals, Synthesis of substances

**1.3 Details of the supplier of the safety data sheet**Company : Sigma-Aldrich  
3050 Spruce Street  
SAINT LOUIS MO 63103  
USATelephone : +1 800-325-5832  
Fax : +1 800-325-5052**1.4 Emergency telephone number**

Emergency Phone # : (314) 776-6555

**2. HAZARDS IDENTIFICATION****2.1 Classification of the substance or mixture**GHS Classification in accordance with 29 CFR 1910 (OSHA HCS)  
Flammable solids (Category 1), H228

For the full text of the H-Statements mentioned in this Section, see Section 16.

**2.2 GHS Label elements, including precautionary statements**

Pictogram



Signal word : Danger

Hazard statement(s)  
H228 : Flammable solid.

Precautionary statement(s)

P210 : Keep away from heat/sparks/open flames/hot surfaces. No smoking.  
P240 : Ground/bond container and receiving equipment.  
P241 : Use explosion-proof electrical/ ventilating/ lighting/ equipment.  
P280 : Wear protective gloves/ eye protection/ face protection.  
P370 + P378 : In case of fire: Use dry sand, dry chemical or alcohol-resistant foam for extinction.**2.3 Hazards not otherwise classified (HNOC) or not covered by GHS - none**

# TASK® 2 & TASK® 3

**Very Low Viscosity, High Performance Liquid Plastics**



[www.smooth-on.com](http://www.smooth-on.com)

## PRODUCT OVERVIEW

TASK® 2 & TASK® 3 low viscosity, high performance casting resins offer superior physical and performance properties compared to our popular Smooth-Cast® Series of general purpose casting resins. Vacuum degassing is not necessary and they offer the convenience of a 1A:1B by volume (115A:100B by weight) mix ratio. The difference between TASK® 2 & TASK® 3 is the pot life and demold time.

TASK® 2 & TASK® 3 are white. They have high tensile and flexural strength, as well as high flexural modulus. These plastics were formulated for a variety of industrial applications including pattern making and making prototype models. These resins are designed for casting in thicknesses up to ½" (1.27 cm). **TASK® Plastics** are moderately priced and are available in trial kits, one-gallon, five-gallon, 55-gallon drum and totes.

## TECHNICAL OVERVIEW

	Pot Life** @ 73°F/23°C (ASTM D-2471)	Cure Time** @ 73°F/23°C	Tensile Strength (ASTM D-638)	Tensile Modulus (ASTM D-638)	Elongation at Break (ASTM D-638)	Flexural Strength (ASTM D-790)	Flexural Modulus (ASTM D-790)	Compressive Strength (ASTM D-695)	Compressive Modulus (ASTM D-695)	Shrinkage in./in. (ASTM D-2566)
TASK® 2	7 min.	60 min.	6,650 psi	290,000 psi	6 %	9,500 psi	288,000 psi	8,300 psi	78,000 psi	0.005
TASK® 3	20 min.	90 min.	6,650 psi	290,000 psi	6 %	9,500 psi	288,000 psi	8,300 psi	78,000 psi	0.0025

\*\* Depending On Mass

Mix Ratio; 1A:1B by volume or 115A:100B by weight

Color; White

Mixed Viscosity, cps; 150 (ASTM D-2393)

Shore D Hardness; 80 (ASTM D-2240)

Specific Gravity, g/cc; 1.12 (ASTM D-1475)

Heat Deflection Temp; 134°F / 57°C (ASTM D-648)

Specific Volume, cu. in./lb; 24.7 (ASTM D-1475)

\*All values measured after 7 days at 73°F/23°C

## PROCESSING RECOMMENDATIONS

**PREPARATION...** Materials should be stored and used in a warm environment (73°F/23°C). These products have a limited shelf life and should be used as soon as possible. All liquid urethanes are moisture sensitive and will absorb atmospheric moisture. Mixing tools and containers should be clean and made of metal, glass or plastic. Mixing should be done in a well-ventilated area. Wear safety glasses, long sleeves and rubber gloves to minimize contamination risk.

Because no two applications are quite the same, a small test application to determine suitability is recommended if performance of this material is in question.

**Applying A Release Agent** - If you are unsure about surface compatibility, a trial casting on a surface finish similar to the final mold or model should be made to avoid damage to the working surface. Polyurethane, latex or metal molds should be dry and require a coat of suitable release agent. Universal Mold Release (available from Smooth-On) is ideal for this purpose. A liberal coat of release agent should be applied onto all surfaces that will contact the plastic. To ensure thorough coverage, lightly brush the release agent with a soft brush over all surfaces. Follow with a light mist coating and let the release agent dry for 30 minutes.

## Appendix B: Specimen Data Collection Procedure

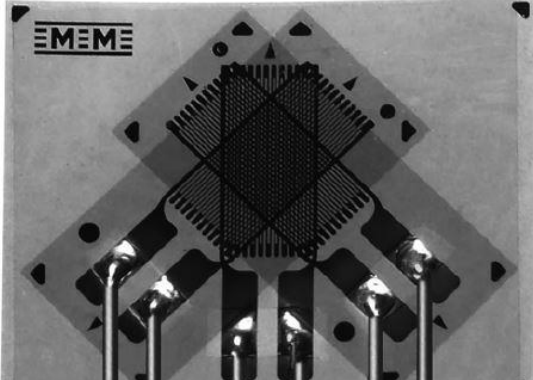
### Strain Gage Installation Procedure

1. De-grease the location where the strain gauge is to be applied using isopropyl alcohol.
2. Sand the mounting surface with 320 grit sandpaper until the surface is free of edges, divots and defects. The mounting location should be of uniform color
3. Wet the sanded surface with M-Prep A (Acid) and rub with a cotton swab. Then sponge it off using unidirectional motion with a sponge.
4. Apply more M-Prep A and begin sanding the surface with 600 grit sandpaper. When finished sanding, rinse with M-Prep A and sponge it off using unidirectional motion.
5. Apply M-Prep 5A (Base) to the mounting surface, rub with a cotton swab, then dry with a sponge using unidirectional motion.
6. Prep the glass strain gauge applicator with acetone for cleaning.
7. Lay strain gauge on glass applicator, the fasten it using 3 strips of Kapton tape.
  - a. \*Note: only fasten one end of the Kapton tape down as it will need to be lifted to transport the strain gauge later.
8. Peel Kapton tape off the glass applicator, making sure the strain gauge stays with the tape. Transfer the gauge (with the tape) over to the test specimen.
  - a. Apply the strain gauge to the specimen and align the vertical layer of the rosette as vertical as possible with visual inspection.
9. Once aligned, push one side of the Kapton tape down to secure it to the specimen. On the other side, peel the gauge up at a 45° angle.
  - a. Now apply the catalyst (blue bottle) to the underside of the strain gauge using the brush applicator. Also apply to the specimen.
10. Allow catalyst to “dry” for about one minute. Then apply 3-4 drops of the fastener (glue) to the specimen. As fast as possible, pull the tape down to stick the gauge to the specimen and use the sponge to flatten it down/remove excess glue.
  - a. Immediately after pressing with the sponge, apply pressure with your thumb to the gauge for 1-2 minutes. (The heat from your thumb helps the fastener solidify) Then wait approximately another 1-2 minutes after removing your thumb before continuing to the next step.
11. Carefully route strain gauge wires down the side of the specimen and fasten them down with Kapton tape. \*This is to ensure no wires are separated during transport/testing prep.
12. Gently peel tape off of the strain gauge

125WW

**MEME** Micro-Measurements

## General Purpose Strain Gages - Stacked Rosette

GAGE PATTERN DATA												
 <b>C2A</b> version shown			GAGE DESIGNATION	RESISTANCE (OHMS)	OPTIONS AVAILABLE							
			See Note 1									
<table border="1" style="width: 100%; border-collapse: collapse;"> <tr> <td style="padding: 2px;">L2A-XX-125WW-120</td> <td style="padding: 2px;">120 ± 0.6%</td> </tr> <tr> <td style="padding: 2px;">L2A-XX-125WW-350</td> <td style="padding: 2px;">350 ± 0.6%</td> </tr> <tr> <td style="padding: 2px;">C2A-XX-125WW-120</td> <td style="padding: 2px;">120 ± 0.6%</td> </tr> <tr> <td style="padding: 2px;">C2A-XX-125WW-350</td> <td style="padding: 2px;">350 ± 0.6%</td> </tr> </table>					L2A-XX-125WW-120	120 ± 0.6%	L2A-XX-125WW-350	350 ± 0.6%	C2A-XX-125WW-120	120 ± 0.6%	C2A-XX-125WW-350	350 ± 0.6%
L2A-XX-125WW-120	120 ± 0.6%											
L2A-XX-125WW-350	350 ± 0.6%											
C2A-XX-125WW-120	120 ± 0.6%											
C2A-XX-125WW-350	350 ± 0.6%											
DESCRIPTION			 <b>Pb-free</b> <b>RoHS</b> COMPLIANT									
<b>GAGE DIMENSIONS</b>			Legend: ES = Each Section S = Section (S1 = Sec 1) CP = Complete Pattern M = Matrix	inch millimeter								
Gage Length	Overall Length	Grid Width	Overall Width	Matrix Length	Matrix Width							
0.125 ES	0.241 CP	0.070 ES	0.280 CP	0.309	0.375							
3.18 ES	6.12 CP	1.78 ES	7.11 CP	7.85	9.53							

GAGE SERIES DATA					
See Gage Series data sheet for complete specifications.					
Series	Description	Strain Range	Temperature Range (See Note 2)		
L2A	Encapsulated constantan gages with preattached ribbon leads.	±3%	−100° to +150°F [−75° to +65°C]		
C2A	Encapsulated constantan gages with preattached ready-to-use cables.	±3%	−60° to +150°F [−50° to +65°C]		
					
Example of an L2A Construction			Example of a C2A Construction		

Note 1: Insert desired S-T-C number in spaces marked XX.

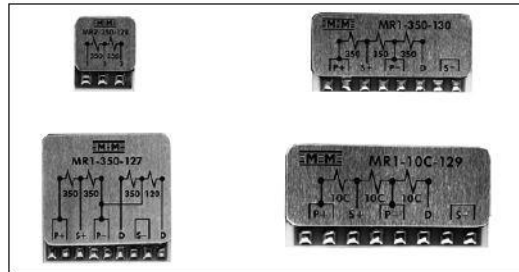
Note 2: Upper use range is reduced to these values for stacked patterns.

## MR-Series Bridge Completion Modules

**MEME** Micro-Measurements



### Information and Selection Chart



Strain gage instrumentation is readily available with built-in bridge completion resistors and "dummy" gages to accept quarter- and half-bridge strain gage input circuits. However, if the instrumentation at hand is not provided with these components, or if the measurement application does not permit their use, external bridge completion must be provided, and MR-Series Bridge Completion Modules can be an excellent choice in these applications.

MR-Series Bridge Completion Modules employ metal-foil resistance elements, bonded to a dense ceramic substrate. The resistance elements are specially processed to "match" the thermal expansion coefficient of the ceramic, resulting in a very low resistance temperature coefficient equivalent to  $\pm 0.15\mu\text{e}^{\circ}\text{F}$  [ $\pm 0.27\mu\text{e}^{\circ}\text{C}$ ] for the half-bridge circuits, and  $\pm 0.35\mu\text{e}^{\circ}\text{F}$  [ $\pm 0.63\mu\text{e}^{\circ}\text{C}$ ] for the dummy gages, over a

temperature range from 0° to +200°F [-18° to +95°C]. Maximum operating temperature range is -50° to +250°F [-45° to +120°C].

Each module is covered with a special environmental protection system to ensure long-term stability. A rugged aluminum overlay, embossed with a wiring diagram for easy terminal identification, affords additional protection, and in many applications no supplementary environmental protection is required. Each module is provided with foam tape for easy attachment to the test-part surface or at the instrumentation site, and tinned, heavy copper terminals facilitate attachment of up to 22-gage [0.64mm dia.] leadwires.

Completing the bridge circuit at the strain gage site provides for a symmetrical, balanced leadwire system between the strain gage circuit and the instrumentation. This can reduce effects of noise pickup in the leadwire system in some environments. Where switch contacts, slip rings, or other mechanical connections are employed between the strain gages and measuring instrumentation, or when leadwires will be periodically disconnected from the measuring instrument, accuracy can be improved by completing the bridge at the measurement site. Bridge completion modules can be designed to meet special circuit requirements. Contact our Applications Engineering Department for a detailed discussion of your special needs.

#### CHARACTERISTICS

Module Type & Features	Bridge Excitation (Volts)	
	Recommended	Maximum
MR1-350-127: Provides a precision 350Ω half bridge as well as 120Ω and 350Ω dummy gages. Recommended for use with half-bridge strain gage circuits of any resistance value, or with 120Ω or 350Ω three-wire quarter-bridge circuits. Size (including foam tape): 1 x 1 x 0.2in [25 x 25 x 5mm]. Weight: 6g.	0.5 – 15V 0.5 – 25V	20V (D120) 35V (D350)
MR1-10C-129: Provides a precision 1000Ω half bridge and a 1000Ω dummy gage. Recommended for use with half-bridge strain gage circuits of any resistance value, or with 1000Ω quarter-bridge circuits. High resistance extends battery life in battery-powered instrumentation, reduces strain gage self-heating, and permits higher bridge excitation voltage to improve signal-to-noise ratio. Size (including foam tape): 1.2 x 0.6 x 0.2in [30 x 15 x 5mm]. Weight: 4g.	0.5 – 30V	40V
MR1-350-130: Provides a precision 350Ω half bridge and a 350Ω dummy gage. Recommended for use with half-bridge strain gage circuits of any resistance value, or with 350Ω three-wire quarter-bridge circuits. Size (including foam tape): 1.2 x 0.6 x 0.2in [30 x 15 x 5mm]. Weight: 4g.	0.5 – 18V	25V
MR2-350-128: Provides a precision 350Ω half bridge in a compact size for use with half-bridge strain gage circuits. Small size makes it ideal for attachment at the strain gage site on the test part in many applications. Size (including foam tape): 0.5 x 0.7 x 0.2in [13 x 18 x 5mm]. Weight: 2g.	0.4 – 18V	25V

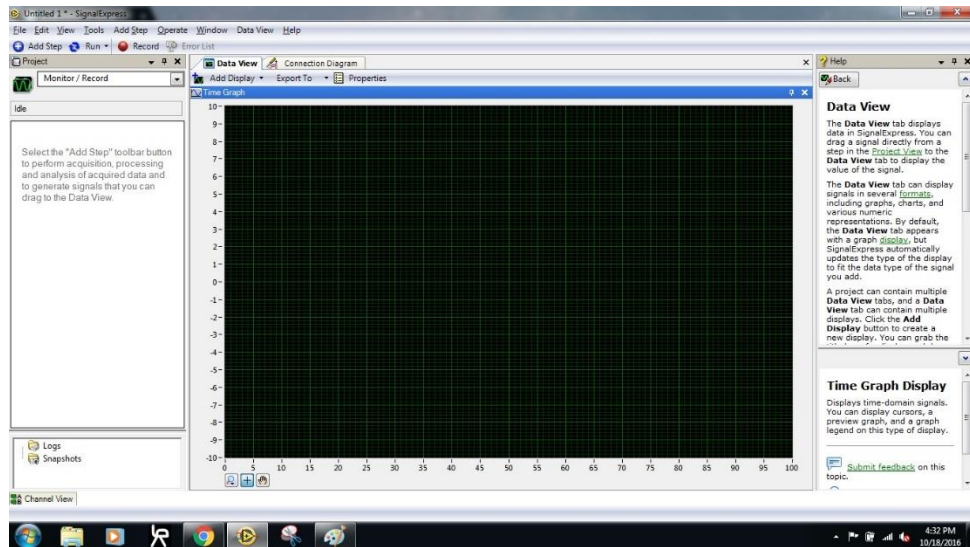
Half-bridge circuits in each module type are balanced to within  $\pm 0.005\%$ . Resistance tolerance on each dummy gage is  $\pm 0.02\%$ .

## NI Signal Express 2015 setup to collect data

1. Open NI Signal Express 2015

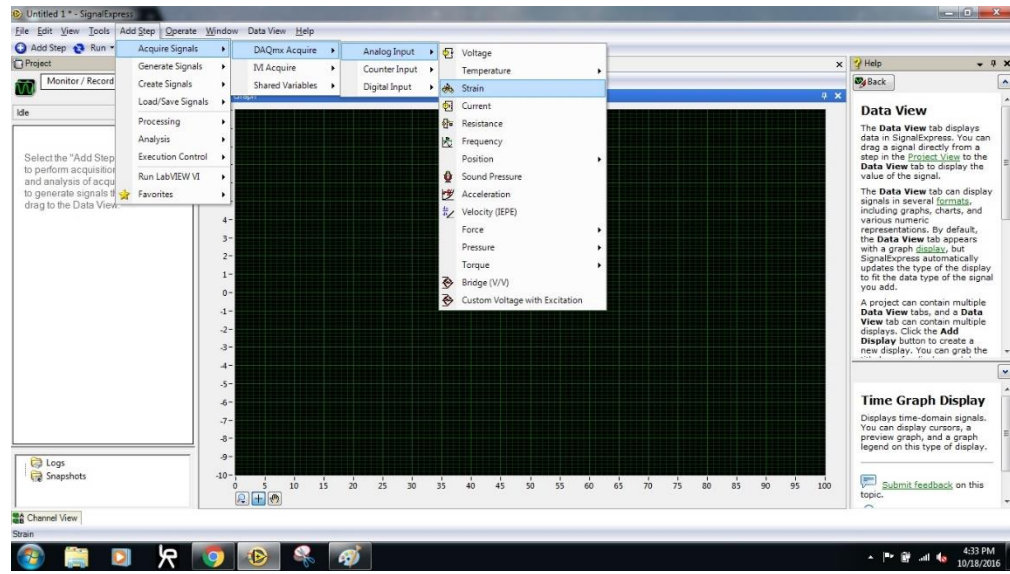


2. Select "empty signal Express project"

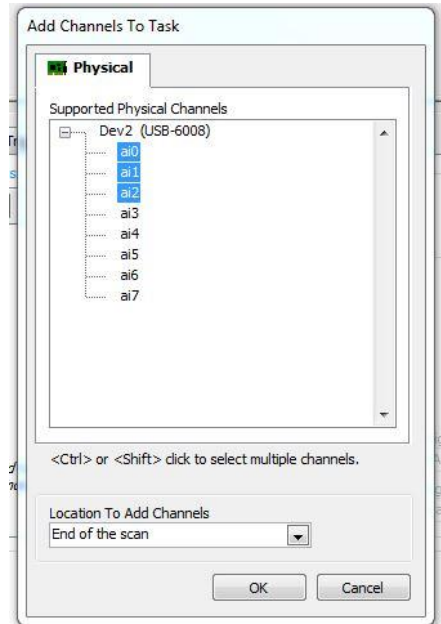


3. Ensure the NI USB 6008 data acquisition module (DAQ) is plugged into the computer.  
Note: another data acquisition module can be used, the Texas Instruments DAQ was used for this project because it was easily accessible
4. Select "add setup"
  - Acquire signals
  - DAQmx Acquire
  - Analog Input

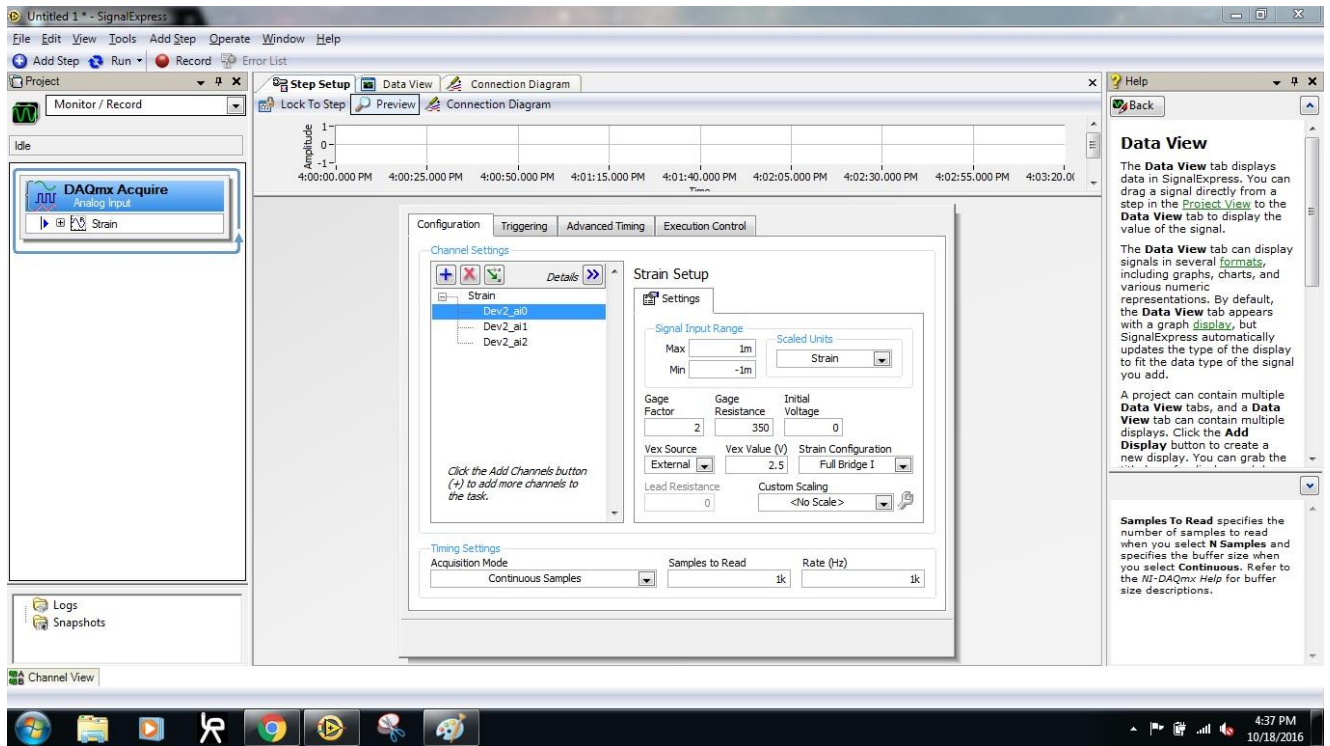
- Strain



- Select the ports that will be used on the DAQ that will be used to collect the signals from the strain gauges

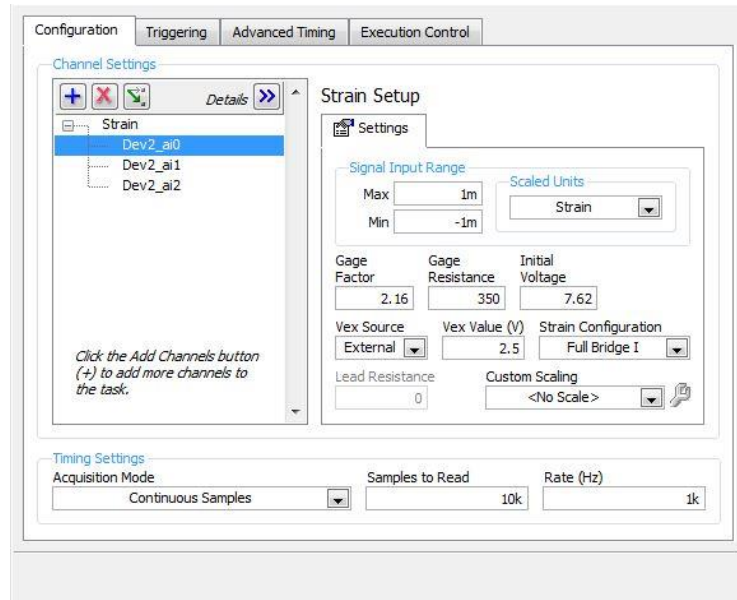


- Click "OK" and the image in the figure below will be produced

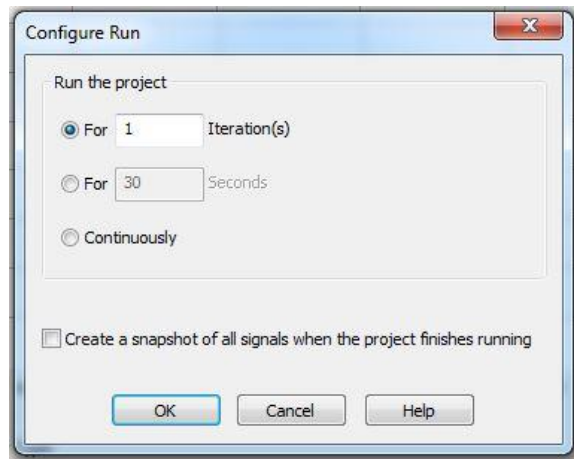


7. For each strain gauge go through and change the following values

- Gauge factor – This is supplied by the manufacturer of the strain gauges. For this experiment, the gauge factor was 2.16
- Gauge resistance – This experiment used a bridge completion module with a resistance of  $350\ \Omega$ .
- Initial Voltage – This is from the power supply being used to power the strain gauges. This iteration of the experiment used a 7.62 Volt, DC battery. Please note the voltage should be read between each test, because the voltage will decrease over time. An AC to DC power supply converter was not chosen, because it creates noise, so to minimize this, the researcher chose to use a DC battery.



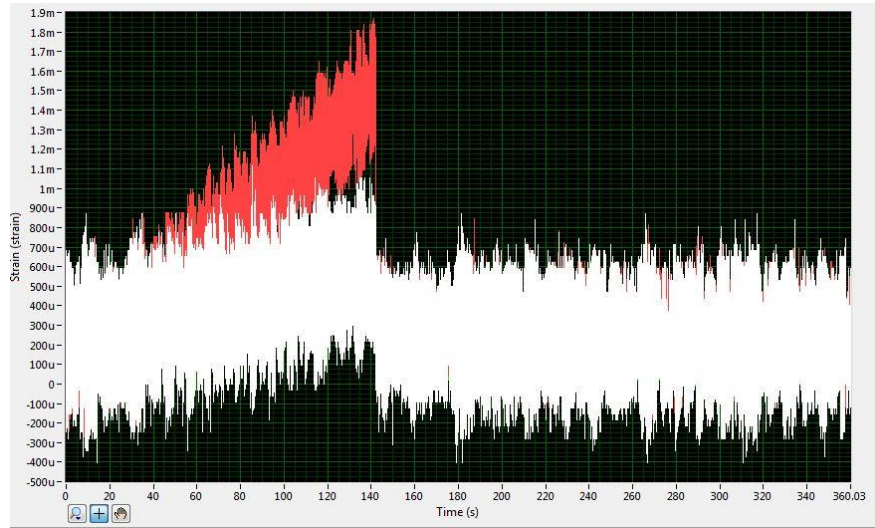
8. Change the samples to read and rate (Hz)
  - if the researcher wants to run for 10 seconds at 1 KHz sampling rate, then set the samples to read at 10K
9. In the upper left tool bar select the run drop down tab
  - Configure Run
  - Select for 1 iteration. This ensures the test runs for 1 iteration of the 10 seconds you set previously, instead of continuously



10. Verify the software and circuit have been setup properly by running a short test around 10 seconds in length. Do this by flexing the specimen gently by hand. Note the direction

of strain being applied visually and compare to that being displayed by the Signal Express software. The strain should be in the same direction. i.e. if you pull the specimen apart, then a positive strain should be shown. Also, note that for this experiment, the researcher chose to use a rosette strain gauge containing three separate strain gauges. The middle gauge was placed along the axis which should show the most strain, so for the short test to verify the equipment, the middle gauge on the Signal Express software, should show a larger strain value than the other two gauges.

11. After running a full test, a plot like the figure below should be produced.



## Appendix C: Toroid Permeability Test

### Objectives:

Use the current through a coil of wire to determine the permeability of the core material.

### Apparatus:

Small signal current clamp  
 Current clamp signal amplifier  
 BNC cable  
 Oscilloscope capable of outputting graph data in .csv file format  
 Caliper  
 Solid core copper wire  
 Carbon fiber/ iron composite toroids

### Procedure:

1. Using the caliper measure the inner and outer radius of each toroid, take average
2. Wrap coil around toroid to match desired number of turns
3. Connect the current clamp to the amplifier and attach around one side of the wire
4. Connect the amplifier to the oscilloscope using the BNC cable
5. Turn on all equipment
6. Apply a 5V 1kHz signal to a coil
7. Measure the slope of the resulting current
8. Using the equations below, calculate the permeability for each toroid
9. Repeat with 5, 10, & 20 turns of coil

### Analysis:

Using Matlab, create a program that will read a .csv file and perform the necessary computations. The program should be manually given the number of turns, toroid dimensions and should calculate the rest from the .csv file.

$$v = L \frac{di}{dt}$$

$$L = \frac{\mu N^2 A_c}{2\pi r}$$

